Dipl.-Ing. Michael RACHINGER, B.Sc.

Simulation and validation of a segmented single SOFC operating on methane

THESIS

submitted in fulfilment of the requirements for the degree of

Diplom-Ingenieur

Master's programme Mechanical Engineering

Graz University of Technology

Adviser: Dipl.-Ing. Dr.techn. Martin Hauth
AVL LIST GmbH

Adviser: Univ.-Prof. Dipl.-Ing. Dr.techn. Christoph Hochenauer
Institute of Thermal Engineering

Supervisor: Univ.-Prof. Dipl.-Ing. Dr.techn. Christoph Hochenauer
Institute of Thermal Engineering

Graz, April 9, 2017

EIDESSTATTLICHE ERKLÄRUNG

AFFIDAVIT

Ich erkläre an Eides statt, dass ich die vorliegende Arbeit selbstständig verfasst, andere als die angegebenen Quellen/Hilfsmittel nicht benutzt, und die den benutzten Quellen wörtlich und inhaltlich entnommenen Stellen als solche kenntlich gemacht habe. Das in TUGRAZonline hochgeladene Textdokument ist mit der vorliegenden Masterarbeit identisch.

I declare that I have authored this thesis independently, that I have not used other than the declared sources/resources, and that I have explicitly indicated all material which has been quoted either literally or by content from the sources used. The text document uploaded to TUGRAZonline is identical to the present master‘s thesis.

Datum / Date

Unterschrift / Signature

Thanks

This thesis was written on behalf of the AVL List GmbH between July 2016 and January 2017. Therefore, my first and foremost gratitude belongs to DI Dr.techn. Martin Hauth. Not only did he provide me with the opportunity to write this thesis at the AVL headquarters in Graz, Austria. He also supervised this thesis in his professional, patient and ever-friendly way. A special thanks also belongs to Univ.-Prof. DI Dr.techn. Christoph Hochenauer for supervising this thesis on behalf of the Technical University Graz.

A large variety of people from AVL List GmbH contributed to this thesis. Most prominently DI Dr.techn. Clemens Fink, who helped me with problems concerning the CFD-Software used, AVL FIRE®. Without his patienence and professional input, this thesis would not have been possible. I thank Nikolaus Soukup B.Sc. for his professional support in technical matters and his help in conducting experiments in the laboratory, Christopher Sallai for his help with PTC Creo and for his company in a lot of coffee-breaks as well as DI Michael Seidl B.Sc. for his general support, open ear for my problems and professional remarks. Further I want to express my gratitude to Roman Lucrezi B.Sc. for his professional remarks regarding AVL Fire, Marlies Hofer B.Sc. for many shared late-night- and weekend-work sessions, Rene Vötter B.Sc. for his support in LaTeX, DI Jörg Mathe for his remarks regarding the conducted laboratory-experiments, Marika Gasteiger B.Sc. for her inputs regarding Faraday's law, Nejc Kosir for his training in AVL FIRE®, Ing. Stefan Weissensteiner M.Sc. B.Sc. for his help in Matlab-Simulink, Clement Dufour M.Sc. B.Sc. for providing experimental data as well as Mag. Doris Schönwetter and Vanessa Timischl for their help in all adminstrative matters. Additionally, I would like to mention Dominic Leipold B.Sc., Johannes Funk B.Sc., DI Michael Derntl, Horst Kiegerl, Alexandre Gitz M.Sc. B.Sc., DI Peter Cartellieri, Patrick Swaschnig, Markus Goll B.Sc. and DI Dr.rer.nat. Stefan Pofahl as well as the whole AVL Fuel-Cell team.

In particular, I have to thank DI Daniel Schaffer B.Sc. for his previous work on the CFD-model, patient consultations and correcting remarks on the thesis. Further I would like to mention DI Stefan Leithner B.Sc for putting me on the right track sometimes, DI Andreas Sattlecker B.Sc. for bringing order to chaos, DI Johannes Riedler B.Sc. for his long-standing support and Michael Eibl B.Sc. for past projects, that put me in the position to write this thesis.

Last but not least I thank my parents, as well as my whole family, for their untiring emotional and financial support. Without them, this thesis would not have been possible.

Thank you all!

Michael Rachinger
January 2017

Abstract

	Titel:	Simulation und Validierung einer mit Methan betriebenen segmentierten Festoxid-Brennstoff-Einzelzelle
	Autor:	Michael Rachinger
1.	Stichwort:	Festoxidbrennstoffzelle
2.	Stichwort:	Dampfreformierung
3.	Stichwort:	Elektrochemie

Brennstoffzellentechnologie stellt sich als vielversprechende Alternative zu konventionellen Energiewandlungstechnologien dar. In dieser Hinsicht zeigt die Technologie der Festoxid-Brennstoffzelle (engl.: solid oxide fuel cell) eine Reihe vorteilhafter Eigenschaften. Diese sind beispielsweise ihr hoher Wirkungsgrad und die Möglichkeit, die durch Zellbetrieb entstehende Abwärme zu nutzen. Zusätzlich sind Festoxid-Brennstoffzellen aufgrund ihrer Eignung zur internen Reformierung in der Lage, direkt mit Kohlenwasserstoff-Brennstoffen betrieben zu werden. Ziel dieser Arbeit ist in diesem Zusammenhang die CFD-Simulation eines Prüfstandes zur Untersuchung einer segmentierten Festoxid-Einzelzelle unter Nutzung von Methan als Brennstoff.

Die Ergebnisse der durchgeführten Simulationen werden unter Zuhilfenahme von Messdaten der AVL List GmbH validiert. Um einen Vergleich zwischen Messdaten und Simulationsergebnissen zu ermöglichen, werden die bereitgestellten Messdaten analysiert. Der Fokus liegt dabei auf der Untersuchung des Verhaltens des Prüfstandes hinsichtlich Reformierung und der gemessenen Temperaturen. Aufbauend auf diese Überprüfungen werden die bereitgestellten Daten verwendet, um eine bereits bestehende Simulation eines Prüfstandes für eine segmentierte Festoxid-Einzelzelle weiter zu entwickeln. Sowohl Abbildung der Reaktionskinetik als auch der Elektrochemie in der CFD-Simulation werden basierend auf den Messdaten eingestellt, um größtmögliche Übereinstimmung zwischen Messdaten und Simulation zu erreichen. Dies erfolgt durch Ermittlung der Parameter zur Modellierung der Methan-Dampfreformierung und der Spannung-Strom-Kurven. Die Validität der Simulation wird in Folge durch einen Vergleich der simulierten und gemessenen Temperaturprofile kontrolliert. Durchgeführte Vergleiche zeigen eine gute Übereinstimmung zwischen Simulation und Messdaten.

Die validierte Simulation wird anschließend dazu verwendet, das Verhalten der segmentierten Festoxid-Einzelzelle bei verschiedenen Betriebszuständen zu untersuchen. Zu diesem Zweck werden die Umgebungstemperatur der Zelle sowie die Stromdichte an den Kathoden variiert. Dabei werden physikalische Parameter, welche nur mittels CFD-Simulation quantifiziert werden können, einer genauen Betrachtung unterzogen. Beispielsweise werden der Einfluss der inhomogenen Brennstoffverteilung an der Anode auf das elektrische Potenzial an den Kathoden und der durch die endotherme Methan-Reformierung verursachte lokale Kühleffekt an der Anode untersucht.

Der nächste Schritt in der Verbesserung des vorliegenden CFD-Modells ist die Simulation von Methan als Brennstoff unter realen Temperaturbedingungen, wie diese in einem Brennstoffzellen-Stapel vorkommen. Des Weiteren bieten die erhaltenen CFD-Ergebnisse eine Basis für Finite Elemente Analysen des Prüfstandes.

Abstract

Title: Simulation and validation of a segmented single SOFC operating on methane

Author: Michael Rachinger

1 st Keyword: Solid Oxide Fuel Cell
2 nd Keyword: Steam Reforming
3 rd Keyword: Electrochemistry

Fuel cell technology shows promise to be a viable alternative to conventional energy conversion technologies. The solid oxide fuel cell (SOFC), for example, shows a number of positive characteristics. These characteristics are, amongst others, its high efficiency and the possibility to use waste heat caused by its high operating temperatures. In addition, SOFCs are able to directly utilize hydrocarbon fuels due to their capability for internal reforming. Therefore, the aim of this thesis is a CFD simulation of a segmented single SOFC testbed in AVL FIRE® using methane as fuel.

The results obtained from these simulations are validated with measurement data provided by AVL List GmbH. In order to be able to compare simulation results to measurements, the provided measurement data is examined. The focus thereby lies on the investigation of the provided data with regard to the fuel reforming behaviour in the test setup and the measured temperature profiles. Following these investigations, the provided data is used to improve an existing simulation of a single SOFC testbed. The reaction kinetics as well as the electrochemistry of the CFD simulation are adjusted to achieve the best possible agreement with the provided measurement data. For this purpose, parameters controlling the simulated methane steam reforming behaviour as well as the simulated current-voltage-curve are determined. Using the parameters found, the validity of the simulation is investigated by comparing measured and simulated temperature profiles. These comparisons indicate good agreement between simulations and measurements.

The validated simulation is further used to investigate the behaviour of the segmented single SOFC under different operating conditions. For this purpose, the ambient temperature as well as the cathode current density are varied. Subsequently, physical properties only quantifiable using CFD analysis are scrutinized. Most prominent properties in this context are the influence of the fuel distribution at the cell's anode on the electric potential on the cathodes and the local cooling effect on the anode due to endothermic fuel reforming reactions. The next step in improving the CFD model is the simulation using methane as fuel under stack-like temperature conditions. Further, the CFD results are ready to form the basis for a finite element analysis of the testbed.

Contents

Figures

Tables

Abbreviations

BC	Boundary Condition
CTE	Coefficient of Thermal Expansion
CAD	Computer Aided Design
CFD	Computational Fluid Dynamics
CGO	Gallium-Doped Ceria
DME	Dimethyl Ether
ECD	Exchange Current Density
LSM	$La_{0.8}Sr_{0.2}MnO_3$
MIEC	Mixed Ionic-Electronic Conduction
SOFC	Solide Oxide Fuel Cell
S/C	Steam-to-Carbon-Ratio
TC	Transfer Coefficient
TPB	Three-Phase-Boundary
OCV	Open Circuit Voltage
PEM	Proton Exchange Membrane
PEN	Positive-Electrolyte-Negative
YSZ	Yttria-Stabilized Zirconia
MFC	Massflow Controller

NI	National Instruments
PC	Personal Computer

Latin Symbols

Symbol	Description	Unit/Value
A	Pre-exponential factor	depends on order
A'	Pre-exponential factor (adapted)	depends on order
b_{H_2}	Hydrogen exponent	[-]
b_{O_2}	Oxygen exponent	[-]
b_{H_2O}	Water exponent	[-]
C_j	Heat capacity of the component j	$[\frac{J}{K}]$
$c_{c_nH_mO_p}$	Concentration of a general hydrocarbon	$[\frac{mol}{dm^3}]$, $[\frac{mol}{m^3}]$
c_{H_2O}	Concentration of a steam	$[\frac{mol}{dm^3}]$, $[\frac{mol}{m^3}]$
c_{H_2}	Concentration of a hydrogen	$[\frac{mol}{dm^3}]$, $[\frac{mol}{m^3}]$
c_{CO}	Concentration of a carbon monoxide	$[\frac{mol}{dm^3}]$, $[\frac{mol}{m^3}]$
c_{CO_2}	Concentration of a carbon dioxide	$[\frac{mol}{dm^3}]$, $[\frac{mol}{m^3}]$
c_{CH_4}	Concentration of a methane	$[\frac{mol}{dm^3}]$, $[\frac{mol}{m^3}]$
$D_{H_2-H_2O}$	Fundamental binary diffusivity	$[\frac{m^2}{s}]$
E_0	Standard open circuit potential	[V]
F	Faraday constant	$[\frac{C}{mol}]$
h	Specific enthalpy	$[\frac{J}{kg}]$, $[\frac{J}{mol}]$
h_j	Enthalpy of formation for j at local temperature	$[\frac{J}{mol}]$, $[\frac{kJ}{mol}]$
$h_{j,ref}$	Enthalpy of formation for j at reference temperature	$[\frac{J}{mol}]$, $[\frac{kJ}{mol}]$
I	Electric current	[A]
I_{max}	Theoretical maximum current	[A]
l_e	Thickness electrolyte	$[\mu m]$, $[m]$
l_c	Thickness electrolyte	$[\mu m]$, $[m]$
l_a	Thickness anode	$[\mu m]$, $[m]$
i	Current density	$[\frac{A}{m^2}]$, $[\frac{mA}{cm^2}]$
i_0	Exchange current density	$[\frac{A}{m^2}]$, $[\frac{mA}{cm^2}]$

K	Equilibrium constant	[-]
K_{eq}	Equilibrium constant for a reaction	[-]
k	Reaction rate constant	depends on order
k_f	Rate constant forward reaction	depends on order
k_b	Rate constant backward reaction	depends on order
k_a	Anodic transfer coefficient	[-]
k_c	Cathodic transfer coefficient	[-]
M_{H_2}	Molar mass hydrogen	$[\frac{g}{mol}]$, $[\frac{kg}{mol}]$
M_{H_2O}	Molar mass steam	$[\frac{g}{mol}]$, $[\frac{kg}{mol}]$
M_{CO}	Molar mass carbon monoxide	$[\frac{g}{mol}]$, $[\frac{kg}{mol}]$
M_{CO_2}	Molar mass carbon Dioxide	$[\frac{g}{mol}]$, $[\frac{kg}{mol}]$
$M_{C_nH_mO_p}$	Molar mass for general hydrocarbons	$[\frac{g}{mol}]$, $[\frac{kg}{mol}]$
M_{O_2}	Molar mass of oxygen	$[\frac{g}{mol}]$, $[\frac{kg}{mol}]$
M_j	Molar mass of a species j	$[\frac{g}{mol}]$, $[\frac{kg}{mol}]$
m	Mass	$[kg]$
$\dot{m}_{O_2}$	Oxygen mass flow	$[\frac{kg}{s}]$
n_s	Number of species	[-]
n_{cat}	Number of cathodes	[-]
n_e	Charge transfer number	[-]
$\dot{n}_{el}$	Molar flow of electrons	$[\frac{mol}{s}]$
$\dot{n}_{el,Cell}$	Molar flow of electrons at the cell	$[\frac{mol}{s}]$
$\dot{n}_{H_2}$	Molar flow hydrogen	$[\frac{mol}{s}]$
$\dot{n}_{CO}$	Molar flow carbon monoxide	$[\frac{mol}{s}]$
$\dot{n}_{CH_4}$	Molar flow methane	$[\frac{mol}{s}]$
n^{el,H_2}	Electron ratio hydrogen	[1]
$n^{el,CO}$	Electron ratio carbon monoxide	[1]
n^{el,CH_4}	Electron ratio methane	[1]
$p^a_{H_2}$	Typical partial pressure of hydrogen in fuel	[V]
$p^a_{O_2}$	Typical partial pressure of oxigen in fuel	[V]
p	Pressure	[Pa],[bar]
p_0	Standard pressure	1 [bar]=10^5 [Pa]
p_j	Pressure of the component j	[Pa], [bar]

$p_{H_2O,neg}$	Partial pressure of water on negative electrode	[Pa], [bar]
$p_{O_2,pos}$	Partial pressure of oxygen on positive electrode	[Pa], [bar]
p_{CH_4}	Partiap pressure of methane	[Pa], [bar]
p_{H_2O}	Partiap pressure of Steam	[Pa], [bar]
p_{H_2}	Partiap pressure of hydrogen	[Pa], [bar]
$p_{Species}$	Partial pressure of a species	[Pa], [bar]
$p_{Ambient}$	Ambient pressure	[Pa], [bar]
p_N	Standard pressure	[Pa], [bar]
Q	Heat	[J]
$Q_{FC_{rev}}$	Fuel cell - total reversible heat	[J]
$\dot{Q}_{react}$	Heat source through chemical reaction	[W]
$q_{FC_{rev}}$	Fuel cell - specific reversible heat	$[\frac{J}{kg}]$, $[\frac{J}{mol}]$
$R_{contact}$	Contact resistance	[Ω]
R_m	Universal gas constant	$R_m = 8.314[\frac{J}{mol \cdot K}]$
R_{ct}^c	Charge transfer resistance	$[\Omega \cdot cm^2]$
r	General reaction rate	$[\frac{mol}{m^3 \cdot s}]$
r_P	Reaction rate of a component P	$[\frac{mol}{m^3 \cdot s}]$
r_{CH_4}	Reaction rate for methane	$[\frac{mol}{m^3 \cdot s}]$
r_{H_2}	Reaction rate hydrogen	$[\frac{mol}{m^3 \cdot s}]$
r_{H_2O}	Reaction rate steam	$[\frac{mol}{m^3 \cdot s}]$
r_{CO}	Reaction rate carbon monoxide	$[\frac{mol}{m^3 \cdot s}]$
r_{CO_2}	Reaction rate carbon dioxide	$[\frac{mol}{m^3 \cdot s}]$
$r_{C_nH_mO_p}$	Reaction rate for general hydrocarbons	$[\frac{mol}{m^3 \cdot s}]$
r_{reform}	Reaction rate reforming reactions	$[\frac{mol}{m^3 \cdot s}]$
r_{shift}	Reaction rate water-gas-shift reaction	$[\frac{mol}{m^3 \cdot s}]$
r_j	Reaction rate of a species j	$[\frac{mol}{m^3 \cdot s}]$
T_N	Standard temperature	[K]
T	Temperature	[K]
T_0	Reference temperature	[K]
T_{FC}	Fuel cell temperature	[K]
T_{pos}	Temperature positive electrode	[K]
T_{neg}	Temperature negative electrode	[K]

U_f	Fuel utilisation	[-], [%]
$V_{FC,rev}$	Reversible voltage	[V]
$V_{oc,r}$	OCV in the TPB	[V]
$\dot{V}_{O_2}$	Oxygen volume flow	$[\frac{m^3}{s}]$
W	Work	[J]
$W_{tFC_{rev}}$	Fuel cell total reversible work	[J]
$w_{tFC_{rev}}$	Fuel cell specific reversible work	$[\frac{J}{kg}]$, $[\frac{J}{mol}]$
z_{O_2}	Charge number of oxygen	[-]

Greek Symbols

Symbol	Description	Unit/Value
β	Transfer coefficient	[-]
$\Delta^r G$	Gibbs enthalpy	$[\frac{J}{mol}]$
$\Delta^r H$	Reaction enthalpy	$[\frac{J}{mol}]$
$\Delta^r S$	Reaction entropy	$[\frac{J}{mol}]$
$\Delta_R H(T^0)$	Standard enthalpy of reaction	$[\frac{J}{mol}]$
Δt_{FF}	Time for fluid to pass through flow field	[s]
η_t	Thermodynamic efficiency	[-], [%]
η_{ohm}	Voltage loss through ohmic resistance	[V]
η^a_{conc}	Concentration polarisation	[V]
η^c_{act}	Cathodic activation polarisation	[V]
η_{act}	Activation overpotential	[V]
$\nu_{Species}$	Molar fraction of a species	[-]
ν_{stP}	Stoichiometric coefficient of a component P	[-] ?
ν_j	Fuel related quantity of the component j	[-]
ρ_e	Resistivity electrolyte	$[\frac{\Omega \cdot mm^2}{m}]$
ρ_c	Resistivity cathode	$[\frac{\Omega \cdot mm^2}{m}]$
ρ_a	Resistivity anode	$[\frac{\Omega \cdot mm^2}{m}]$
ρ_{O_2}	Density of oxygen	$[\frac{kg}{m^3}]$
Φ	Slope of Arrhenius line	[°]
Φ_{ele}	Electronic potential at TPB	[V]
Φ_{ion}	Ionic potential at TPB	[V]
Φ_{oc}	Open circuit potential	[V]
$\Phi_{oc,pos}$	Electric potential positive electrode	[V]
$\Phi_{oc,neg}$	Electric potential negative electrode	[V]

Chemical Species

Symbol	Description
C	Elemental Carbon
CH_4	Methane
C_8H_{18}	Gasoline (simplified Model)
CH_3OH	Methanol
CO	Carbon Monoxide
CO_2	Carbon Dioxide
Cr	Elemental Chrome
$C_xH_yO_z$	General Carbohydrate
H_2	Hydrogen
H_2O	Water
Mg_2NiH_x	Metal Hydrate
Mn	Elemental Manganese
N	Elemental Nitrogen
N_2	Nitrogen
NH_3	Ammonia
Ni	Elemental Nickel
O_2	Oxygen
P	Elemental Phosphorus
S	Elemental Sulfur
Si	Elemental Silicium

1 Introduction

High temperature solid oxide fuel cells (SOFCs) represent the most efficient devices for the electrochemical conversion of chemical energy of hydrocarbon fuels into electricity. Therefore, they have been gaining increasing attention for cleanly and efficiently distributed power generation [56]. A major aspect of SOFCs is that they offer direct conversion from electrochemical to electrical energy without additional conversion steps and that they represent a stable energy supply with high efficiency and low pollution [57]. Additionally, due to their high efficiency, SOFCs require less fuel to achieve a target power. Therefore, less CO_2 is emitted into the atmosphere [58].

AVL List GmbH participates in the EU-Project PROSOFC, which has the aim to improve reliability of SOFCs [59]. A series of theses is conducted in order to drive the project to its goal. The aim of the thesis at hand is to adapt the existing model developed by Fabian Rasinger [51] and Daniel Schaffer [53] to simulate the behaviour of an existing testbed running on methaneous fuel in AVL FIRE®.

Although first attempts to achieve this goal have already been made (see [18]), the obtained results still show room for improvement. One of the drawbacks up to this point is that no simulation results have been validated using measurements with methane as fuel. Therefore, this thesis builds heavily on the work of Clement Dufour [15], who performed extensive measurements on the physical test rig using methaneous fuels. Unfortunately, the gathered data was only partly evaluated. Therefore, this thesis also has a strong focus on the analysis and interpretation of the provided measurement data.

Aspects alredy covered in previous theses will not be investigated in greater detail. These are especially the fluid mechanics investigated by Fabian Rasinger [51] and the material properties gathered by Daniel Schaffer [53].

Using the interpreted data, the computational fluid dynamics (CFD) simulation is adapted to imitate measuring conditions. Subsequently, the chemical kinetics as well as the IV-curves are fitted to measurement data. Further, the simulated temperature profiles are compared to measured data as an additional criterion to ensure the validity of the simulation results. The goal for further thesis is to use validated CFD data as input for FE analysis of thermal stresses.

2 Theoretical Basis

The aim of the following chapter is to give a short summary of the topics relevant for this thesis. First the function, designs and elements of SOFCs will be reviewed. Then, chemical and thermodynamical aspects will be taken into consideration.

2.1 Function, Designs and Elements of SOFCs

2.1.1 Principal Function

Figure 1 shows the scheme of an SOFC. An SOFC consists of five components: electrolyte, anode, cathode and two interconnects. The electrolyte acts as a conductor of oxide ions at temperatures from 600 °C to 1000 °C. The ceramic material allows oxygen atoms to be reduced by electrons on its own porous cathode surface. Thereby, these atoms are converted to oxide ions which are then transported through the ceramic electrolyte to a fuel-rich porous anode zone. At this anode zone, the oxide ions can react with a fuel (for example hydrogen) and dispense electrons to an external circuit [56]. Electronic conductivity is necessary to convey the electrons resulting from the electrode reaction out into the external circuit. The electrochemical reaction takes place in the region where oxygen ions provided by the electrolyte can discharge electrons to the conducting anode, as illustrated in figure 2 [38].

This requires gas phase for fuel access, electrolyte phase for oxide ion entry and metal phase for electron output. Therefore, the region where these phase conditions are met is called „three-phase-boundary“ (TPB). In order to ensure an efficient operation, the TPB should not be a simple linear structure or two-dimensional interface of the solid materials. Instead it should be distributed to provide an active „volumetric“ reaction region. The fabrication of the anode is critical to ensure that the finely dispersed TPB has a large reactive surface [38].

Oxygen ions migrate through the electrolyte toward the anode-electrolyte-fuel TPB via vacancy hopping mechanisms. There they can participate in the electrochemical oxidation of fuels. As long as there is an electrical load connected between the anode and the cathode, electrons from the anode will flow through the load back to the cathode. Therefore, electric

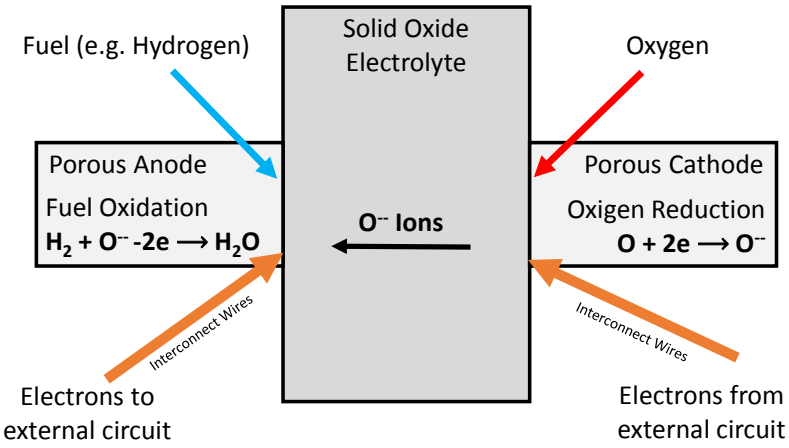

Figure 1: Function of an SOFC [56]

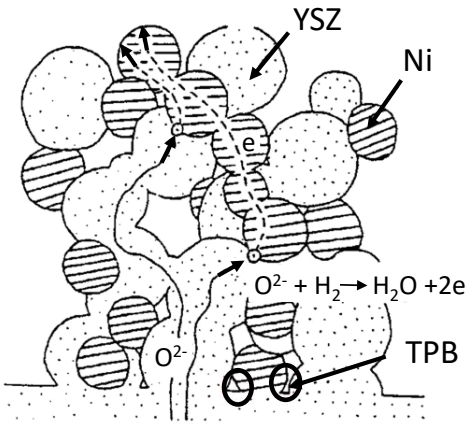

Figure 2: Schematic of anode cermet structure. Interpenetrating networks of pores and conductors can be seen. Conductors are nickel for electrons and YSZ for oxide ions. The reactive sites are the contact zones of two conducting phases which are accessible to fuel through porosity [38].

current will flow through the circuit [28].

2.1.2 Typical Designs

Under typical operating conditions a single cell produces less than 1 V. In order to get a higher voltage and therefore power output, it is necesseary to combine several cells into a cell stack. This can be done in a number of ways using various interconnect materials which are often fabricated into complex shapes to provide a number of additional functions besides

electronic conduction. These functions include air and fuel channelling as well as sealing [29]. A major issue is designing cells that can be stacked to produce a significant power output. This output is directly proportional to the cell area. In order to increase the power output, the maximum area of Yttria-stabilized zirconia (YSZ) membrane must be packed into a SOFC stack. The two common principal solutions are a stack of flat plates and an array of parallel tubes [56].

a) Tubular Cell Designs

As described in [14], tubular cells are commonly arranged as parallel pipes. The functional elements of each cell thereby form concentric circles.

In a tubular stack packed in a square array, the power density depends on the diameter D of the cells and the gap g between them. Therefore, having small diameters and less gaps is necessary in order to provide high power densities [56].

Since this thesis has its focus on investigations of a testbed for a planar SOFC, tubular cells will not be discussed in further detail.

b) Planar Cell Designs

Planar SOFCs provide very high areal ($\frac{W}{cm^2}$) and volumetric ($\frac{W}{cm^3}$) power densities. Furthermore, they can be manufactured by low-cost conventional ceramic processing techniques. Issues that need to be resolved are sealing of the cell edges and the control of temperature gradients which can cause cell cracking [29]. As illustrated in figure 3, the components of typical planar cells are configured as flat layers that are connected in electrical series [29, 40, 41]. Like any other cell configuration, planar SOFCs must be designed to have the desired electrical and electrochemical performance. Further, they require appropriate thermal management as well as mechanical and structural integrity to meet operating requirements of specific power generation applications. Key requirements are [29, 41, 47]:

- Electrical performance: The design must minimise ohmic losses in the stack.
- Electrochemical performance: The design has to provide the highest possible open circuit voltage. Further, polarisation losses should be minimized.
- Thermal management: The design must provide means for stack cooling and a more uniform temperature distribution during operation.
- Mechanical and structural integrity: The SOFC stack should be designed to exhibit a good mechanical strength. This is important when assembling and handling the SOFC stack.

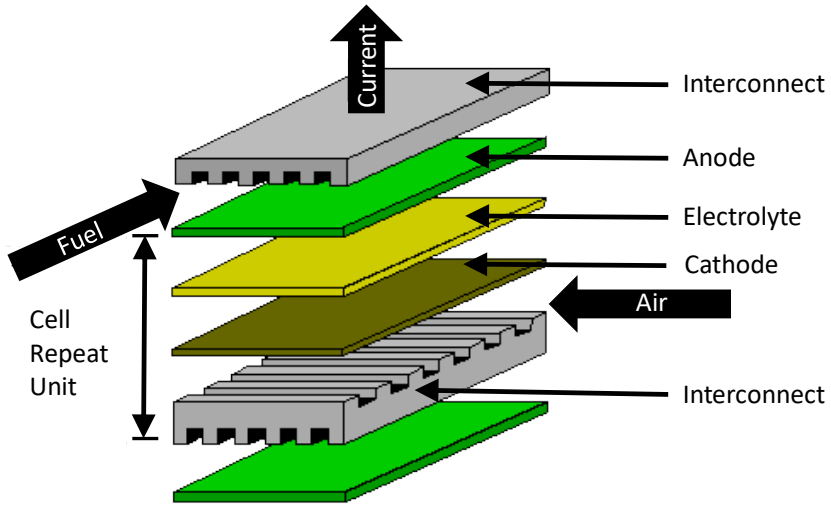

Figure 3: Typical design of a planar SOFC [17, 29]

Planar SOFCs can be classified into self-supported and externally supported configurations. In a self-supporting cell arrangement, one of the components of the cell has the role of providing structural support for the whole cell. In most cases this is the thickest layer. Thus, single cells can be designed as either electrolyte supported, anode supported or cathode supported. In the externally supported configuration, the single cell consists of thin layers that are applied on an interconnect or a porous substrate. Figure 3 illustrates a possible cell configuration for planar SOFCs [29]. Planar cells have various advantages [56]:

- They can be produced by screen printing,
- stacked together with narrow channels to achieve high power densities
- and can provide short current pathways through the interconnect.

Nonetheless, there are major disadvantages of large planar cells [56]:

- Large areas of sheets are difficult to fabricate and handle. Sheet sizes which can be practically fabricated and handled are much smaller than those of, for example polymer membranes, which are used in PEM fuel cells.
- Sealing off the gas around the edges of cells can be difficult.

2.1.3 Components

a) Electrodes

The application of electrode layers can be performed in numerous ways. These range from vapor deposition and solution coating to plasma spraying and collodial ink methods such as screen printing and paint spraying. Out of these methodes, paint spraying represents the most economic approach, since it is widely used in the traditional ceramic industry to lay down glaze layers from particulate inks to give electrode thicknesses of 50-100 µm [56].

Anodes

The task of the anode in an SOFC is to provide the necessary sites for the fuel to react with the oxide ions delivered by the electrolyte within a structure. Anodes have to combine catalytic activity for fuel oxidation with electrical conductivity. The anode's catalytic properties are neccessary for the kinetics of the fuel oxidation with the oxide ions travelling through the solid electrolyte. Ionic conductivity allows the anode to spread the oxide ions across a broader region of the anode/electrolyte interface. This property minimises resistive and overpotential losses (see chapter 2.2.2) [38].

This structure also needs to facilitate the necessary charge neutralisation by its electronic conductivity. These functional considerations and the operation environment of the anode play a major role in the selection of anode materials. The material has to be refractory to sustained periods of cell operation temperature and thermal cycling to ambient temperature. Due to the variations in oxygen partial pressures, certain metallic components of the anode could suffer by fuel oxidation products. Furthermore, electrical properties and lattice geometry of oxide components of the anode could change by variations of stoichiometry. Therefore, chemical and physical stability of the anode material are essential [38].

In addition to these requirements, compatibility with the other materials the anode comes in contact with is necessary. Specifically, these materials are the electrolyte, the interconnect and any other relevant structural components. Physical compatibility thereby requires matching thermomechanical properties and the absence of phase-change effects which could generate stresses during temperature variations. In order to ensure chemical compatibility, solid state contact reactions and interdiffusion of constituent elements should be avoided, despite extreme temperature conditions. The stated requirements also apply to anode-interconnect interfaces in assembled stacks. Furthermore, compatibility also has to cover ambient gases. This includes corrosion or poisoning by trace impurities such as sulphur [38].

Nickel is the most widely used material for the electronic-conducting phase of SOFC anodes.

This is largely due to its known performance and economics. Unfortunately, nickel does not adhere strongly to YSZ and therefore flakes off. The driver for this flaking is the large difference in the coefficient for thermal expansion (CTE) between metal and ceramic. The mismatch between the different CTEs can be reduced by the use of a heat-treated mixture of nickel oxide with YSZ. The application of this "nickel cermet" as anode material allows for a better adhesion between anode and electrolyte [56]. A further disadvantage of nickel-based anodes is their propensity to become coated with a carbon layer when reacting with hydrocarbon fuel (see chapter 2.3). The most common material for anodes in SOFCs is nickel-zirconia-cermet [38].

Cathodes

A cathode's performance ultimately depends on its surface area, porosity and microstructure. The most important properties for cathodes are their catalytic activity for oxygen reduction and their compatibility with the electrolyte. The latter includes a matching CTE and chemical non-reactivity. Further, they have to withstand a highly oxidising environment. Therefore, cathodes represent a major issue in the design and operation of SOFCs. Due to their application in an oxidising environment, the use of base metals is not possible. In addition, the use of noble metals is economically limited by their higher costs. Furthermore, cathodes have to fulfill requirements like a high electrical conductivity, high catalytic activity for oxygen reduction and compatibility with other cell components. An additional important point is the interaction with the interconnect. Thereby the possibility of poisoning the cathode has to be taken into consideration. This can, for example occur due to Cr contamination [65].

As a consequence, semiconducting oxides like doped lanthanum cobaltites or lanthanum manganites have been commonly used in the past [56]. A large variety of perovskites has been considered and investigated concerning their catalytic activity. The most common perovskites used with YSZ electrolyte up to 1000 °C are lanthanum manganite-based materials. This is common practice although these materials show only a low oxide ion diffusivity and therefore a limited electrochemical activity. The reason for their popularity is their superior chemical stability [65]. $La_{0.8}Sr_{0.2}MnO_3$ (LSM) provides a good combination of electronic conductivity and expansion coefficient matching. Higher conductivity can be obtained at higher dopant levels with the downside of a too high expansion coefficient [56]. For cell operation at lower temperatures down to 700 °C composite cathodes made from LSM/YSZ are used. Less severe conditions for the chemical reactions at temperatures below 800 °C make it attractive to use more catalytically active perovskites as cathodes [65].

b) Electrolytes

The electrolyte for SOFCs has to be stable in both reducing and oxidising environments. It should show a high ionic conductivity while having a low electronic conductivity at the operating temperature of a cell. Furthermore, it is neccessary that the material can be formed into a thin, strong and gastight film [24]. Additional requirements an electrolyte has to meet the following [56]:

- Denseness and leak-tightness
- Correct composition for good ionic conduction at operating temperatures
- Low thickness to reduce ionic resistance
- Large area to maximise the current capacity
- Resistance to thermal shock
- Economical processability

The most favoured electrolyte material used in SOFCs at present is Yttria-stabilised zirconia (YSZ). While there is a large variety of oxide ion-conduction materials, YSZ has a number of significant attributes that make it ideal for this application. These attributes include abundance, chemical stability, non-toxicity and economics. However, the material has also drawbacks, including its high CTE and problems concerning joining and of sealing the material [56]. Other fluorite structured oxide ion conductors, for example ceria, have been proposed as electrolyte materials for SOFCs as well, especially for the operation under reduced temperatures of around 600-800 °C. Materials that have been found to possess good ionic conductivity are, amongst others, pervoskites, brownmillerites and hexagonally structured oxides [24].

Zirconia-based compositions are still the best electrolytes at present. The reason for this is their good stability under reducing atmospheres, low electric conductivity and acceptable ion conductivity above 800 °C. However, YSZ is by no means the best oxide ion conductor. Its popularity is also based on several negative aspects other oxides display. Such disadvantages are, for example, electronic conductivity, high costs or difficulties in processing [24].

For YSZ electrolytes, the lowest operation temperature of the cell is estimated to be about 700 °C considering YSZ conductivity and mechanical property data. Since a trend of SOFC development is operation at lower temperatures, this represents a limitation. A possible alternative to avoiding this limitation are ceria-based electrolytes which can be operated at 550 °C or less. For the operation at higher temperatures a dual layer electrolyte with a thin YSZ layer on gallium-doped ceria (CGO) has been proposed. Another possibility is the use of pervoskite compositions [24]. Electrodes are applied to the electolyte's surfaces in contact with fuel (anode) and the oxidant (cathode). Usually, particulate materials are partially sintered to form the porous conducting layers which make up the electrodes. In

many cases, several layers are laid down. This allows for a gradient of properties ranging from nearly pure YSZ at the electrolyte surface to almost pure electrode composition at the interconnect contact [56].

c) Interconnects

The two major roles of the interconnect in SOFCs are to establish the electrical connection between cells and to seperate the gases within the cell stack. The interconnection requires two interconnection wires which are often combined into a single material. The interconnects connect the anode on one side and the cathode on the other. Because of the oxidising potential on the air electrode and the reducing condition at the fuel side, an inert and impervious material is needed [56]. Similar to the other components of an SOFC, the interconnect has to withstand both oxidising and reducing gases. Therefore also the interconnect must fulfill stringent material requirements. Typical requirements for interconnect materials are [6, 47]:

- High electronic and low ionic conductivity
- Chemical stability regarding both anode and cathode gases
- A CTE similar to the other cell components
- High mechanical and structural integrity
- High thermal conductivity
- Chemical stability in regard to other cell components

Costs and ease of fabrication further limit the possible choices [6]. Common materials for this application are on one hand perovskite-type oxide ceramics based. These are based on rare earth chromites and are suited for operation temperatures in the range of 900-1000 °C. On the other hand, for lower temperature cell operation metallic alloys can be used [6]. Usually lanthanum chromite is being used for systems operating near 1000°C. This is because lanthanum chromite can be doped using strontium to achieve the same CTE as YSZ. Typically, 20 mol% strontium dopant in lanthanum chromite result in a CTE of about $11 \times 10^{-6}/K$. Unfortunately, lanthanum chromite is not inert and thus expands in hydrogen [56]. For operation at lower temperatures (700-850°C) the use of metallic alloys like ferritic steel or chromium-based alloys is feasible [56].

d) Sealings

The seal is required to prevent gas leakage, seperate the fuel and oxidant within the fuel cell and hold the fuel cell components together. The sealants must be chemically and mechanically compatible with the different oxide and metallic cell components. Moreover,

they have to be electrically insulating [50]. According to [50], currently three types of seals are utilised:

- Compressively bonded sealants require an externally applied load.
- Compliant sealants are susceptible to chemical reactions and are electrically conductive.
- Rigid sealants (regarded as glass and glass-ceramics) are rigidly bonded to the cell components. Thus, they can prevent leakage and mixing of gasses. Further, they are electrically insulating, flexible in design, easy to manufacture and cost-competitive.

The seal should be strong and stiff in order for stacks to be stable and able to withstand varying pressure differences during operation. In addition, the seal should be soft enough to reduce mechanical stresses during fabrication and operation [30]. Glass ceramic materials can be applied to the sealing surfaces as a powder dispersed in a paste, as tape cast sheets or by screen printing [37].

2.2 Thermodynamics and Chemistry of SOFCs

In principle, SOFCs convert a fuel's chemical energy directly into electricity using an oxidant gas (air). Thermodynamically this can be treated in terms of the free enthalpy of the reaction of the fuel with oxidant [63]. In order to be able to discuss various aspects of an SOFC, as for example its thermodynamics, relevant chemical reactions have to be stated. Therefore, in the following section the reaction of hydrogen and hydrocarbons will be taken into consideration. For a discussion of the impact of fuels for SOFC operation see chapter 2.3. Based on the stated fuel reactions, an overview over the thermodynamics of SOFCs will be given. Table 1 states relevant fuel reactions. The prominent reactions of hydrogen and methane are subsequently looked at in greater detail.

Table 1: Possible reactions in SOFCs [34]

Fuel		Reaction
Hydrogen	Anode	$H_2 + O^{2-} \rightleftharpoons H_2O + 2e^-$
	Cathode	$\frac{1}{2}O_2 + 2\,e^{2-} \rightleftharpoons O^{2-}$
	Overall	$H_2 + \frac{1}{2}O_2 \rightleftharpoons H_2O$
Methane	Anode	$CH_4 + 4O^{2-} \rightleftharpoons CO_2 + 2H_2O + 8\,e^-$
	Cathode	$2O_2 + 8\,e^- \rightleftharpoons 4O^-$
	Overall	$CH_4 + 2O_2 \rightleftharpoons CO_2 + 2H_2O$
Carbonmonoxide	Anode	$CO + O^{2-} \rightleftharpoons CO_2 + 2e^-$
	Cathode	$\frac{1}{2}O_2 + 2\,e^{2-} \rightleftharpoons O^{2-}$
	Overall	$CO + \frac{1}{2}O_2 \rightleftharpoons CO_2$

a) Fuel-Cell Reaction of Hydrogen

Equation 2.1 states the chemical reaction of the combustion of hydrogen with air. Air is thereby assumed to consist of 79% nitrogen (N_2) and 21% oxygen (O_2). Furthermore, equation 2.1 assumes a hot combustion of hydrogen with air, an air-fuel ratio $\lambda > 1$ and a complete reaction. This implies that all educts react completely to products [31].

$$H_2 + \frac{1}{2}\lambda O_2 + \frac{1}{2}\lambda \frac{0,79}{0,21} N_2 \longrightarrow H_2O + \frac{1}{2}(\lambda\text{-}1) O_2 + \frac{1}{2}\lambda \frac{0.79}{0.21} N_2 \tag{2.1}$$

Chemical reactions in general have many intermediate steps and form various intermediate products. As a simplification, only the reaction educts and products are taken into consideration. The reaction equation for the stoichiometric oxidation of hydrogen with air is therefore [31]:

$$H_2 + \frac{1}{2} O_2 \longrightarrow H_2O \tag{2.2}$$

The same result as in equation 2.2 can be achieved by assuming $\lambda = 1$ and ignoring the nitrogen in equation 2.1. This can be done since nitrogen is an inert gas and has therefore no effect on the reaction.

Figure 4 illustrates the transport processes within an SOFC connecting the thermodynamic and electrical effects using the example of hydrogen oxidation [63]. Equation 2.2 is independent

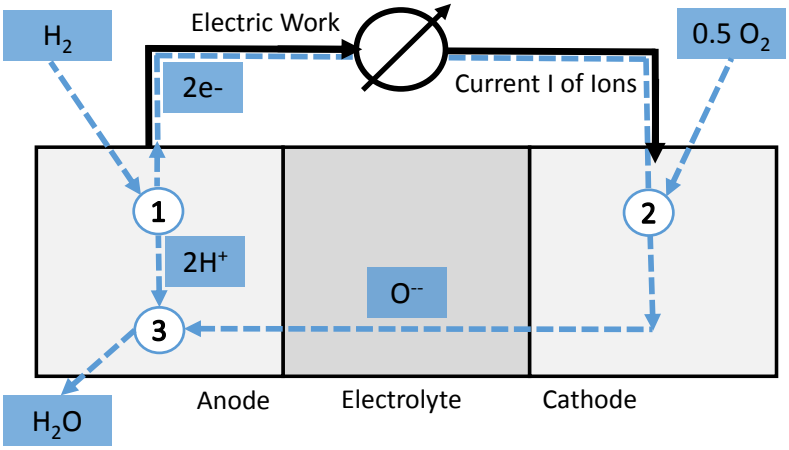

Figure 4: Transport processes within an SOFC [63]

of the process itself. The reaction path in an SOFC depends on the anode and the cathode reactions. Hydrogen is adsorbed at the anode, ionised and the electrons are removed by the connection to the electrical load where the electrical work is used. Oxygen is adsorbed at the cathode connected with the load and ionised by the arriving electrons. The oxide ion is

conducted to the anode by the electrolyte. The hydrogen ions (protons) and the oxide ion form a water molecule. Equation 2.3 gives reaction (1) on the anode [63].

$$H_2 \longrightarrow 2H^+ + 2e^- \tag{2.3}$$

Reaction (2) on the cathode is [63]:

$$\frac{1}{2}O_2 + 2e^- \longrightarrow O^{2-} \tag{2.4}$$

The oxide ion O^{2-} is conducted through the electrolyte and arrives at the anode. At the anode reaction (3) forms water according to equation 2.5 [63]:

$$2H^+ + O^{2-} \longrightarrow H_2O \tag{2.5}$$

b) Fuel-Cell Reactions of Hydrocarbon

The general reaction equation of an ideal combustion of hydrocarbons is [31]:

$$\begin{aligned} C_nH_mO_p + \lambda(n + \frac{m}{4} - \frac{p}{2})O_2 + \frac{0.79}{0.21}\lambda(n^+\frac{m}{4} - \frac{p}{2})N_2 \longrightarrow \ldots \\ \ldots \longrightarrow nCO_2 + \frac{m}{2}H_2O^+(\lambda - 1)(n + \frac{m}{2} - \frac{p}{2})O_2{}^+\frac{0.79}{0.21}\lambda(n + \frac{m}{2} - \frac{p}{2})N_2 \end{aligned} \tag{2.6}$$

In the course of this thesis, the reaction of methane is of special interest. By using equation 2.6, setting the variables $n = 1$, $m = 4$ and $p = 0$, assuming $\lambda = 1$ and ignoring the inert gas nitrogen, equation 2.7 can be obtained. This is the overall reaction equation for methane (CH_4) [27].

$$CH_4 + 2O_2 \longrightarrow CO_2 + 2H_2O \tag{2.7}$$

The reaction on the anode is given in equation 2.8, whereas the reaction on the cathode is given in equation 2.9 [27].

$$CH_4 + 4O^{2-} \longrightarrow CO_2 + 2H_2O \tag{2.8}$$

$$2O_2 + 8e^- \longrightarrow 4O^{2-} \tag{2.9}$$

In practice, instead of the methane-combustion reaction, the direct electrochemical methane reforming reaction (see equation 2.10) is used [27].

$$CH_4 + H_2O \longrightarrow 3H_2 + CO \tag{2.10}$$

2.2.1 The Ideal Reversible SOFC

The use of the first and second law of thermodynamics allows for a simple description of a reversible fuel cell. Therefore a reversible operating fuel cell where fuel and air enter and exit the fuel cell as non-mixed flows is assumed. The non mixed reactants deliver the total enthalpy $\sum n_i H_i$ to the fuel cell. Furthermore, the non mixed products leave the cell with the enthalpy $\sum n_j H_j$. In addition, the heat Q_{FCrev} has to be extracted from the fuel cell and transported to the environment in a reversible way. This can be done, for example, if the fuel cell and its environment have the the same thermodynamic state. Q_{FCrev} is defined positive if it is transported to the fuel cell. The reversible work W_{tFCrev} is produced by the fuel cell. Figure 5 illustrates the described model [63].

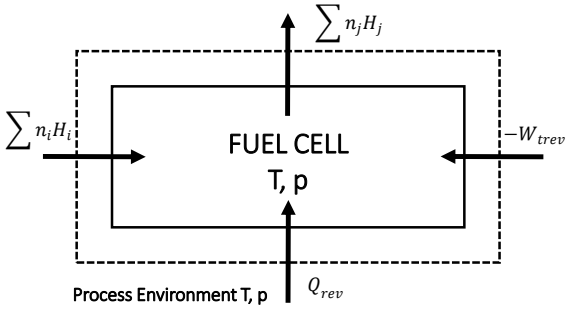

Figure 5: The reversible fuel cell: system boundary and energy balance [63]

a) Reaction Enthalpy and Reaction Entropy

Usually, specific mass or mol related figures are used, whereas the fuel quantity is the reference. Using the first law of thermodynamics on figure 5 gives [63]:

$$\Delta^r H = q_{FCrev} + w_{tFCrev} \tag{2.11}$$

The reaction enthalpy $\Delta^r H$ of the oxidation covers the production of the reversible work and heat. The second law of thermodynamics gives [63]:

$$\oint dS = 0 \tag{2.12}$$

The reaction entropy $\Delta^r S$ is a result of the reaction itself and must be compensated by the transport of the reversible heat q_{FCrev} to the environment, as formulated in equation 2.12

[63]:

$$\Delta^r S - \frac{q_{FCrev}}{T_{FC}} = 0 \tag{2.13}$$

Using $dS = \frac{dH - v\,dp}{T}$, the entropy S_j of any component j can be written as [63]:

$$S_j(T,p) = S_j^0 + \int_{T0}^{T} \frac{C_{Pj}(t)}{t} dt - R_m \cdot \ln\left(\frac{p_j}{p_0}\right) \tag{2.14}$$

In equation 2.14 C_{Pj} is the temperature dependent heat capacity of the component j. Equation 2.14 can be used to find an expression for the reaction entropy $\Delta^r S(T,p)$ [63]:

$$\Delta^r S(T,p) = \Delta^r S(T) - R_m \cdot \ln K \tag{2.15}$$

K in equation 2.15 represents the equilibrium constant [63]:

$$K = \prod \left(\frac{p_j}{p_0}\right)^{\nu_j} \tag{2.16}$$

The parameter ν_j in equation 2.16 is the fuel-related quantity of the component j in the equation of the oxidation reaction, where p_0 is the standard pressure of 1 bar [63].

b) Gibbs Enthalpy

Equations 2.11 and 2.13 can be used to find an expression for the reversible work w_{tFCrev}, stated in equation 2.17 [63].

$$w_{tFCrev} = \Delta^r H - T_{FC} \cdot \Delta^r S \tag{2.17}$$

The reversible work w_{tFCrev} of the reaction given in equation 2.18 is equal to the free enthalpy or Gibbs enthalpy $\Delta^r G$ of the fuel-reactions [63] (see chapter 2.3).

$$\Delta^r G = w_{tFCrev} = \Delta^r H - T_{FC} \cdot \Delta^r S \tag{2.18}$$

As stated above, the mixing effects during fuel utilisation within an SOFC do not allow for a reversible SOFC operation. These effects and the voltage reduction can be calculated by considering the fuel utilisation connected with a change of the partial pressures of the components within the system [62, 63]. Equation 2.17 can be written more precisely as equation 2.19 [63].

$$\Delta^r G(T,p) = \Delta^r H(T,p) - T \cdot \Delta^r S(T,p) \tag{2.19}$$

In the given case, the pressure dependence of $\Delta^r H(T,p)$ can be neglected, as stated in equation 2.20 [63].

$$\Delta^r G(T,p) = \Delta^r H(T) - T \cdot \Delta^r S(T,p) \tag{2.20}$$

Further, the following expression can be found [63]:

$$\Delta^r G(T,p) = \Delta^r G(T) + T \cdot R_m \cdot \ln(K) \tag{2.21}$$

c) Thermodynamic Efficiency

The thermodynamic efficiency of a process is conventionally defined as given in equation 2.22. [28]

$$\eta_t = \frac{\dot{W}}{\dot{W} + \dot{Q}} = \frac{\dot{W}}{\dot{m}|\Delta h|} \tag{2.22}$$

It has to be noted that η_t measures only how efficiently chemical energy extracted from the fuel stream is converted to useful power, rather than heat. To find a formulation for the overall efficiency, the fuel utilisation also has to be taken into consideration [28]. The reversible efficiency η_{FCrev} of the fuel cell is the ratio of the Gibbs enthalpy $\Delta^r G$ to the reaction enthalpy $\Delta^r H$ at the thermodynamic state of the fuel cell. Using Equation 2.17 gives [63]:

$$\eta_{FCrev} = \frac{\Delta^r G}{\Delta^r H} = \frac{\Delta^r H - T_{FC} \cdot \Delta^r S}{\Delta^r H} \tag{2.23}$$

Further, η_{FCrev} can be written as stated in equation 2.24 [28].

$$\eta_{FCrev} = \frac{\Delta G^0}{\Delta H^0} + \frac{RT}{\Delta H^0} ln \prod_k p_k^{\nu_k} \tag{2.24}$$

Since the process environment of an SOFC can not exist near the ambient state, it is only an artificial model. Further, an SOFC can also be described as an electrical device where the electrical effects are explained by thermodynamics [63].

d) Electric Current and Fuel Utilisation

The electric current I is a linear function of the molar flow of the electrons $\dot{n_{el}}$ respectively the molar flow of the spent fuel [63]. Therefore, according to [21], the fuel utilisation can be

expressed as the ratio of the actual current to the (theoretical) maximum current:

$$U_f = \frac{I}{I_{max}} \tag{2.25}$$

$$I_{max} = \dot{n}_{el,Cell} \cdot F \tag{2.26}$$

With $\dot{n}_{el,Cell}$ being the flow of molar stream of electrons along the cell and F representing the Faraday-Constant. The approach offers several advantages. For example, it can be used to express the fuel utilisation operating on a mixture of different fuels. This can be done by accounting for the molar streams $\dot{n}$ and the respective electron ratios n^{el} of fuel-species in the fuel mixture [21]:

$$\dot{n}_{el,Cell} = n^{el,H_2} \cdot \dot{n}_{H_2} + n^{el,CO} \cdot \dot{n}_{CO} + n^{el,CH_4} \cdot \dot{n}_{CH_4} \tag{2.27}$$

$$\dot{n}_{el,Cell} = 2 \cdot \dot{n}_{H_2} + 2 \cdot \dot{n}_{CO} + 2 \cdot \dot{n}_{CH_4} \tag{2.28}$$

e) Reversible Voltage and Nernst Voltage

The reversible voltage V_{FCrev} of the oxidation of any fuel gas can be written as follows [63]:

$$V_{FCrev} = \frac{-\Delta^r G}{n^{el} \cdot F} \tag{2.29}$$

Subsequently, the use of the assumption of an ideal gas allows for an expression of the Nernst voltage or Nernst potential V_N. Therefore, equation 2.30 can be formulated [63]:

$$V_N = \frac{-\Delta^r G(T)}{n^{el} \cdot F} - \frac{R_m \cdot T \cdot \ln K}{n^{el} \cdot F} \tag{2.30}$$

The oxidation reactions of fuel species (e.g. H_2 and CH_4) determine the reaction enthalpy, the reaction entropy and thus the free enthalpy and voltage of the reversible oxidation as formulated in equations 2.18 and 2.29. To calculate these variables, the thermodynamic data of the reactions at the standard conditions (25 °C, 1 bar), as available in various literature sources, is needed [63].

2.2.2 Losses in Fuel Cells

If no current flows, the cell voltage is called the open-circuit-voltage (OCV). In many cases the OCV is equal to the potential developed by a reversible cell i.e. the already discussed Nernst potential. As current flow increases, internal losses grow. Because the cell potential

has to overcome these losses (also called overpotentials, see Figure 6), the cell potential drops. Mentioned losses include [30]:

- Ohmic overpotential: associated with the ion transport through the electrolyte
- Activation overpotential: associated with energy barriers to the charge transfer reactions
- Concentration overpotential: associated with gas-phase species diffusion resistance through the electrodes

At the continuum level, the simulation of electrode and cell performance requires only a parameterised electrochemical model. Such a chemical model is usually described as a current-voltage relation (I-V-curve). The I-V relation describes the voltage (potential) loss at a specific current with respect to the ideal thermodynamic performance. This ideal performance is called overpotential or polarisation. The I-V curve is specific for the materials, structural characteristics and operational parameters (gas composition, pressure, temperature) of a given positive-electrolyte-negative (PEN) element [30]. Polarisation is a common parameter in the analysis of fuel cell performance [44].

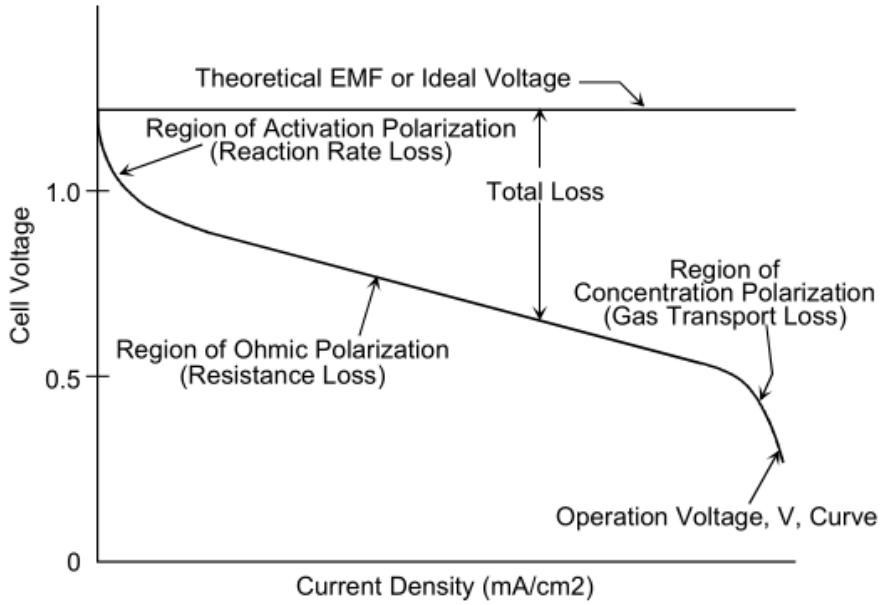

Figure 6: Schematic plot of voltage versus current density [14]

a) Ohmic Polarisation

All matters, with the exception of superconductors, offer a resistance to the motion of electric charge. In the simplest case, this behaviour can be described by Ohm's law. The

assumed linear behaviour between voltage drop and the current density can be described by the resistivity of the materials used. Doing so, the resistivities ρ_e, ρ_c and ρ_a as well as the thicknesses l_e, l_c and l_a for the electrolyte, cathode and anode and a possible contact resistance $R_{contact}$ have to be taken into account. For these ohmic resistances at a given current density, the voltage loss η_{ohm} is given by equation 2.31 [25].

$$\eta_{ohm} = (\rho_e l_e + \rho_c l_c + \rho_a l_a + R_{contact}) \tag{2.31}$$

b) Concentration Polarisation

The concentration polarisation is caused by the resistance that gas molecules experience when being transported through porous electrodes. Transport of gaseous species usually occurs by binary diffusion. The effective binary diffusivity is a function of the fundamental binary diffusivity $D_{H_2-H_2O}$ and microstructural parameters of the anode [12, 20, 25]. In electrode microstructures with very small pore sizes, the possible effects of Knudsen diffusion, adsorption/desorption and surface diffusion may also be present. The physical resistance to the transport of gaseous species through the anode at a given current density is reflected as an electrical voltage loss. This polarisation loss is known as concentration polarisation η^a_{conc}. It is a function of:

- $D_{H_2-H_2O}$
- Microstructure
- Partial pressures
- Current densitiy

In order to get physically measurable parameters, analytical expressions for anodic concentration polarisation have been derived. These allow for an explicit determination as a function of a number of parameters. One important parameter is the anode-limiting current density. This is the current density, at which the partial pressure of the fuel at the interface between anode and electrolyte is near zero. Therefore the cell is starved of fuel and the voltage drops to zero [25]. Looking at comparable cathode and anode thicknesses and microstructures, the anodic concentration polarisation is usually much lower than the cathodic concentration polarisation. On the one hand this is the case because the binary diffusitivity of the fuel is usually higher than that of oxygen. (e.g.: The binary diffusivity of $H_2 - H_2O$ is four to five times greater than the binary diffusivity of $O_2 - N_2$. This is due to the low molecular weight of H_2 compared to the other species.) On the other hand the typical partial pressure of hydrogen in the fuel $p^a_{H_2}$ is much larger than the typical partial pressure of oxygen in the oxidant $p^c_{O_2}$. Thus in a practical non-electrolyte-supported cell design one electrode is thicker than the other [25].

c) Activation Polarisation

A fundamental step in electrode reactions is the transfer of charges. Thereby, a neutral species is converted into an ion or an ion is converted into a neutral species. Thus both reactions involve electron transfer. Electrodes in solid state electrochemical devices may be either purely electronic conductors or display both ionic and electronic conductivity, also called mixed ionic-electronic-conduction (MIEC). Further, the electrodes may be single phase,

two phase or composites [25].

The oxygen reduction, being a multi-step process, usually follows several parallel reaction pathways. Despite the difficulty of isolating a single rate-determining step out of a series of steps, it is usually possible to describe the overall process in a phenomenological framework. See [25] for an example of possible reaction steps. The rate of cathodic reaction is directly proportional to the net current density. A loss of voltage (overpotential) is associated with the reaction rate or the passage of current. Usually the reaction is thermally activated. The relation between the cathodic activation polarisation η^c_{act} is nonlinear, except at very low current densities. The activation-polarisation η^c_{act} depends on following parameters [25]:

- Material properties
- Microstructure
- Temperature
- Atmosphere
- Current densitiy

A phenomenological approach to describe the quantitative relation between current density and η^c_{act} is given by the Butler-Volmer equation 2.32 [25].

$$i = i^c_0 \left(exp\left(\frac{\beta z F \eta^c_{act}}{RT}\right) - exp\left(\frac{(1-\beta) z F \eta^c_{act}}{RT}\right)\right) \tag{2.32}$$

The variable β in equation 2.32 is the transfer coefficient, a dimensionless, positive number, while i^c_0 is the exchange current density. The given relationship between η^c_{act} and i is nonlinear and implicit. Thus η^c_{act} can not be determined as a function of the current density. Instead it gives the net current density for a given η^c_{act}. Only limiting the forms of the Butler-Volmer equation allows for expressing η^c_{act} as a function of current density i. In the low current density limit the simplifications 2.33 and 2.34 can be applied [25].

$$i^c_0 \left| \frac{\beta z F \eta^c_{act}}{RT} \right| << 1 \tag{2.33}$$

$$i^c_0 \left| \frac{(1-\beta) z F \eta^c_{act}}{RT} \right| << 1 \tag{2.34}$$

This leads to the simplified expression in equation 2.35 which can be rearranged to equation 2.36 [25].

$$i \approx i^c_0 \left| \frac{\beta z F \eta^c_{act}}{RT} \right| \tag{2.35}$$

$$|\eta^c_{act}| \approx \frac{RT}{z F i^c_0} \tag{2.36}$$

The term $\frac{RT}{zFi^c_0}$ in equation 2.36 has the unit $\left[\Omega cm^2\right]$. Since this is the unit of an area specific

resistance, it is referred to as the charge transfer resistance R^c_{ct}. It has to be noted, however, that the linear relation between η^c_{act} and the current density i in the low limit of the current density does not imply ohmic relationship. This is because the response time for the process is too long and it is determined by its underlying physical process [25].

In the high current density regime the approximation shown in 2.37 can be applied [25].

$$\left|\frac{\beta z F \eta^c_{act}}{RT}\right| >> 1 \tag{2.37}$$

Doing so, the Butler-Volmer equation can be written as given in equation 2.38 [25].

$$\eta^c_{act} \approx \frac{RT}{\beta z F} ln(i^c_0) - \frac{RT}{\beta z F} ln(i) \approx a + b ln(i) \tag{2.38}$$

The expression in 2.38 is also referred to as the Tafel equation [20]. As described in [25], cathodic and anodic activation polarisations can be considered in greater detail.

2.3 Fuels for SOFCs

2.3.1 Possible Fuels

SOFCs combine the benefits of high energy efficiency with fuel flexibility [36]. The fastest reaction on the nickel anode is that of hydrogen. Nonetheless, other fuels can react directly on the anode, depending on the composition of the catalyst. Two prominent examples are the reaction of carbon monoxide on Ni/YSZ and the reaction of methane on the anode. The reaction of methane on the anode requires a catalyst (e.g. ceria) to provide suitable sites for direct oxidation [56].

The choice the operating temperature, and therefore also the choice of fuel, are largely dependent on the intended application [46]. An eligible fuel for SOFCs is supposed to be cheap, safe, pollution free, causes no electrode contamination and is easy to transport and store. Table 2 illustrates the relative values for gravimetric and volumetric densities of fuels potentially relevant for SOFCs. Comparing equal masses of a certain fuel, hydrogen is the best choice. However it has several downsides like a low volumetric density. The requirement of storage for liquid hydrogen is too severe and the gravimetric density of metal hydride is too small [36]. Therefore it has to be stored at high pressures, resulting in high costs for storage and transportation.

Natural gas represents the most widely used fuel. Reasons for this are its low costs and existing supply infrastructure. Further it is clean, abundant and readily available. The composition of

natural gas varies. It consists of predominantely methane although it can contain significant quantities of higher hydrocarbons. As already mentioned, SOFCs generally operate above 600 °C [25]. A major benefit of this high operation temperature is the possibility to run the cells directly on practical hydrocarbon. Because of this, a complex and and expensive fuel reformer is not necessarily needed [46]. Since hydrocarbon fuels still have the problem of coking, ammonia may be an alternative [36]. Other possible fuels are for example dimethyl ether (DME) or methanol [46].

Table 2: List of possible fuels for SOFCs [36]

Fuel	Formula	Volum. densities ($\frac{mol}{l}H_2$)	Gravim. densities (wt% H)
Ammonia	NH_3	60	17.6
Gaseous Hydrogen	H_2	10	100
Liquid Hydrogen	H_2	35	100
Metal Hydride	Mg_2NiH_x	39	3.6
Methanol	CH_3OH	49	12.5
Nature Gas	CH_4	21	25
Gasoline	C_8H_{18}	55	15.8

2.3.2 Approaches for Fuel-Reforming

The following section gives a short overview on the different possible approaches for fuel-reforming in SOFCs.

a) Internal Reformation of Hydrocarbon Fuels

Internal reforming of the fuel within an SOFC stack is preferred. The main reasons for this are the increase of the operational efficiency and the reduction of complexity. The increase in efficiency is due to the recuperation of waste heat from the stack into the fuel supply [46]. According to Singhal et. al. [46], internal reforming can be achieved by following approaches:

- Indirectly, using a seperate fuel reforming catalyst within the SOFC stack
- Directly on the nickel anode
- A combination of direct or indirect approaches: A seperate catalyst within the SOFC system to convert a significant proportion of the hydrocarbon fuel to synthesis gas is used. The balance of the fuel reforming occurs directly on the nickel anode.

Nonetheless there are several problems associated with internal reforming in SOFCs. A particular problem is the deposition of carbon from hydrocarbon pyrolysis. The effects of

carbon deposition, as well as other damaging aspects of non-hydrogen fuels, are discussed in section 2.3.5. Because of the high speed and strongly endothermic nature of the fuel reformation reactions (see equations 2.43 and 2.44), instabilities in coupling them with the slow and exothermic fuel cell reactions can occur [46].

Direct Internal Reforming

Direct internal reforming of the fuel on the anode offers the simplest and most cost effective design for SOFC systems. Figure 7 illustrates the potential reaction pathways that can occur on the anode. In direct reforming, the anode has to fulfill three roles [46]:

- The anode acts as a reforming catalyst. It has to catalyse the conversion of hydrocarbons to hydrogen and carbon monoxide.
- The anode has the role of an electrocatalyst. Therefore the anode is responsible for the electrochemical oxidation of H_2 and CO to water and CO_2.
- The anode has to be an electrically conducting electrode.

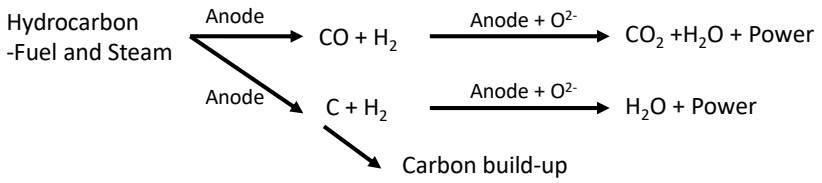

Figure 7: Possible reaction pathways in a directly reforming SOFC [46]

An advantage of the direct internal reforming is the formation of steam by the consumption of hydrogen. This steam can then be used to reform more of the hydrocarbon fuel. Thus the electrochemical reactions help to drive the reforming reaction to completion. Unfortunately the endothermic nature of the reforming reaction also represents a disadvantage. This is due a sharp cooling effect at the cell inlet induced by the endothermic direct reforming. The cooling effect results in an inhomogenous temperature distribution and a steep temperature gradient along the length of the anode. Potential result of this is cracking of the anode and electrolyte materials, since this temperature gradient can be hard to control. A further problem with direct reforming is the susceptibility of the nickel anode to catalyse the pyrolysis of methane and higher carbons (see equation 2.58). This results in deleterious carbon deposition and the build up of deactivating carbon which subsequently leads to a rapid cell deactivation [46, 52].

Indirect Internal Reforming

Indirect internal reforming uses a seperate catalyst to reform the hydrocarbon fuel to synthesis gas. This catalyst is integrated into the SOFC stack upstream of the anode. Nontheless the heat from the exothermic fuel cell reaction is still utilised. Figure 8 schematically shows the reaction pathways in an SOFC with indirect internal reforming. This type of reforming is less efficient and more complicated than direct reforming. However, it still represents a significantly more efficient, simpler and more cost effective approach than using an external reformer. The main advantage of indirect reforming over direct reforming is that it is easier to control from a thermodynamic point of view [46].

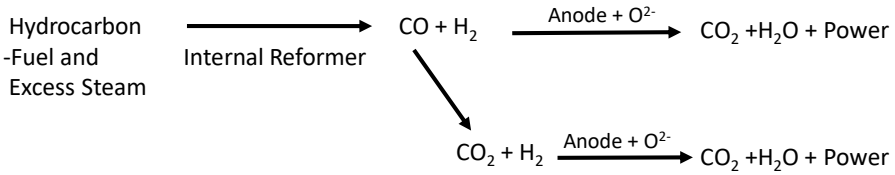

Figure 8: Schematic of reaction pathways in an indirect internal reforming SOFC [46]

b) Direct Electrocatalytic Oxidation of Hydrocarbons

In theory it is possible to operate SOFCs on natural gas or other hydrocarbon fuels without adding any oxidant to the fuel. In this case, the hydrocarbon fuel is oxidised directly on the anode using the oxide ions that have passed through the solid electrolyte from the cathode [46, 48].

There are several possible reactions. Methane can be partially oxidised by the oxide ions to carbon monoxide and hydrogen, as expressed by equation 2.39. Another potential reaction is the full oxidation of hydrocarbon to CO_2 and water, as given in equations 2.40 and 2.41. A third possibility is the combination of partial and total oxidation, as shown in equation 2.42 [46].

$$CH_4 + O^{2-} \longrightarrow CO + 2H_2 + 2e^- \tag{2.39}$$

$$C_nH_{2n+2} + nO^{2-} \longrightarrow nCO + (n+1)H_2 + 2ne^- \tag{2.40}$$

$$CH_4 + 4O^{2-} \longrightarrow CO_2 + 2H_2O + 8e^- \tag{2.41}$$

$$C_nH_{2n+2} + (3n+1)O^{2-} \longrightarrow nCO_2 + (n+1)H_2O + 2(3n+1)e^- \tag{2.42}$$

Again, the main problem of direct electrocatalytic oxidation of hydrocarbon fuels at the anode is the tendency towards carbon deposition through hydrocarbon decomposition [46].

2.3.3 Steam-Reforming of Hydrocarbon-Fuels

The term steam reforming describes a reaction of hydrocarbon with steam to produce a hydrogen/carbonmonoxide mixture as the actual fuel for the cell [38]. The following equations show the reactions of hydrocarbon steam reforming for methane (equation 2.43) and higher carbons in general (equation 2.44). The reactions are strongly endothermic. In the case of methane, the reaction requires $\Delta H = +206\ kJmol^{-1}$ [46], [34].

$$CH_4 + H_2O \rightleftharpoons CO + 3H_2 \qquad \Delta_R H(T^0) = 206\ \text{kJ/mol} \tag{2.43}$$

$$C_nH_{2n+2} + nH_2O \rightleftharpoons nCO + (2n{+}1)H_2 \tag{2.44}$$

In addition to methane-steam reforming, the simultanously occuring exothermic water-gas shift reaction (equation 2.45) has to be taken into consideration [34].

$$CO + H_2O \rightleftharpoons H_2 + CO_2 \qquad \Delta_R H(T^0) = -41.2\ \text{kJ/mol} \tag{2.45}$$

According to [34], the methane-steam reforming reaction is favored at higher temperatures. This can be shown using equation 2.46, which states the equilibrium-constant K_r of steam reforming [11].

$$K_{pr} = 1.026710^{10} exp\left(-0.2513Z^4 + 0.3665Z^3 + 0.5810Z^2 - 27.134Z + 3.2770\right) \tag{2.46}$$

$$Z = \frac{1000}{T(K)} - 1 \tag{2.47}$$

Figure 9 uses equations 2.46 and 2.47 to plot K_r as a function of the temperature. Similarly, the behaviour of the water-gas shift reaction can be calculated using 2.48. The corresponding plot is shown in figure 10 [11], [34].

$$K_{ps} = exp\left(-0.2935Z^3 + 0.6351Z^2 + 4.1788Z + 0.3169\right) \tag{2.48}$$

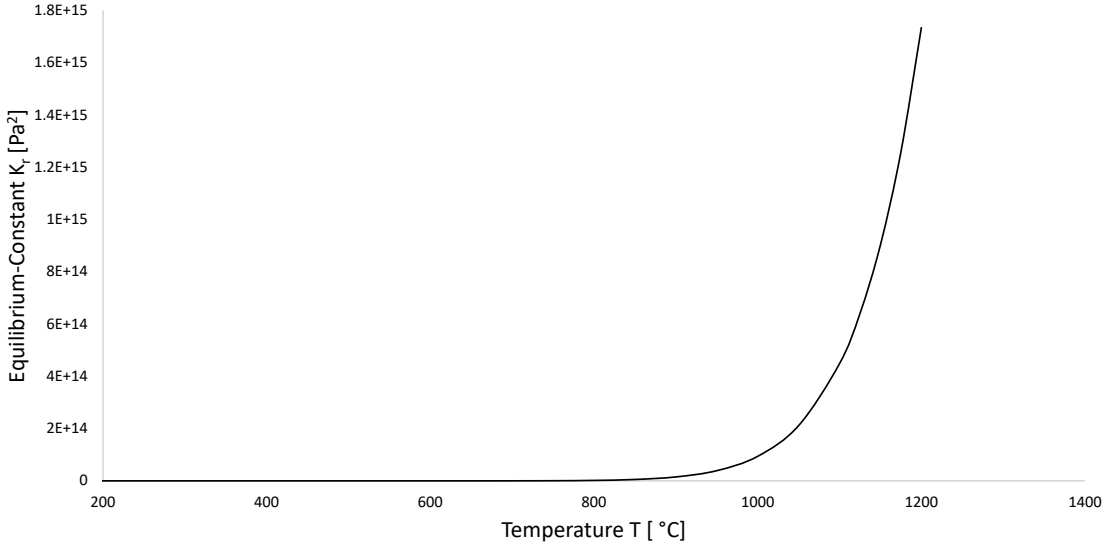

Figure 9: Equilibrium constant of the steam reforming reaction as a function of temperature [11, 34]

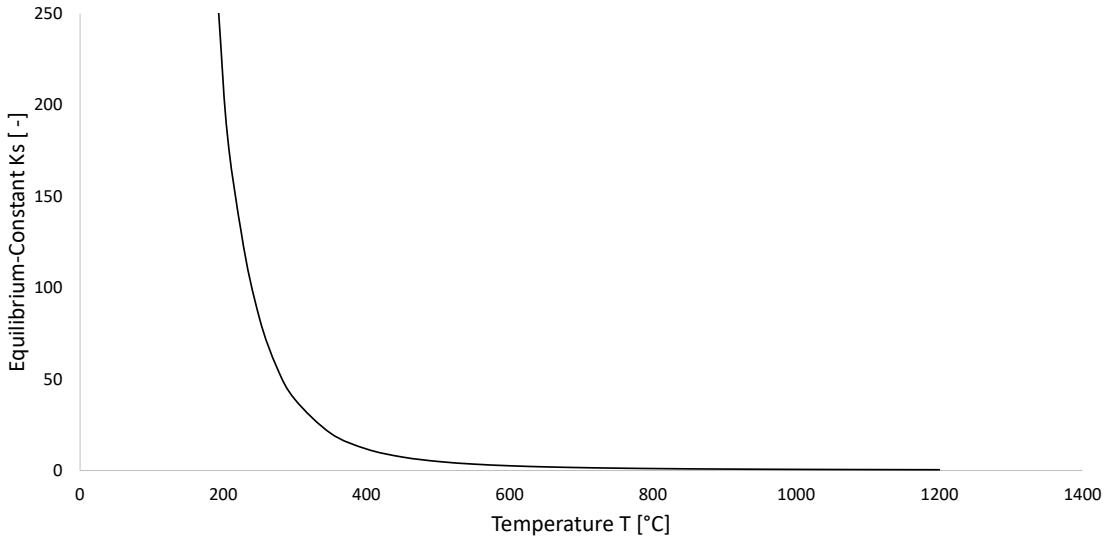

Figure 10: Equilibrium constant of the water-gas shift reaction as a function of temperature [11, 34]

In steam reforming catalysis, steam to carbon ratios of around 2,5-3 are common. Thereby excess of the stoichiometric requirement of equation 2.43 is given. Fuel reforming takes

place on nickel particles at the anode. Reactions leading to the deposition of carbon are minimised (see chapter 2.3.5) [46, 56]. Figure 11 states the equilibrium composition assuming a S/C-ratio of 2.

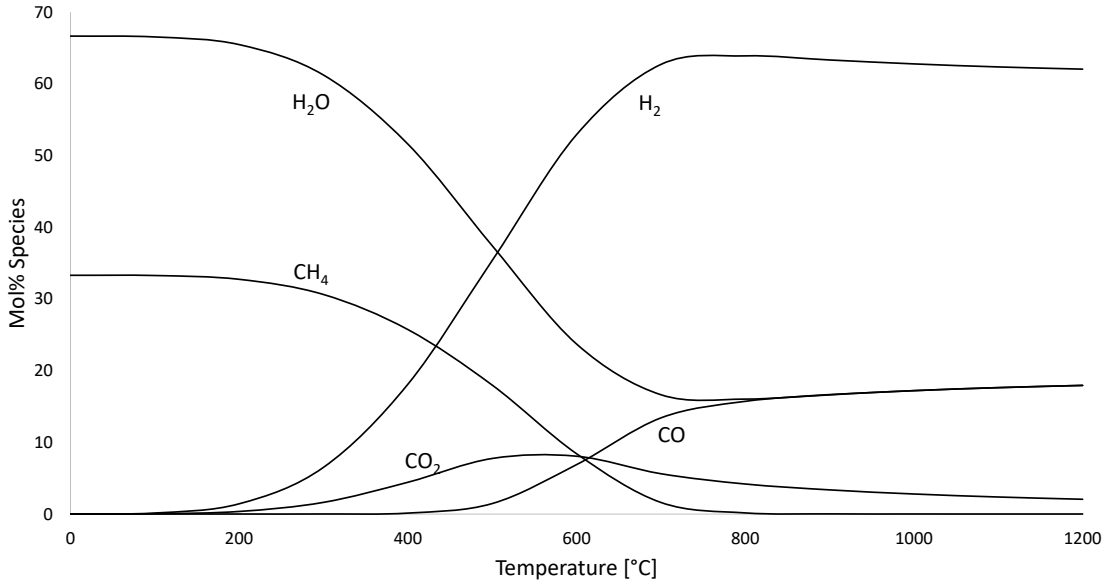

Figure 11: Equilibrium composition for a S/C-ratio of 2 as a function of temperature. [9, 34]

The possible reaction pathways in an internally reforming SOFC running on natural gas and steam can be seen in figure 12 [46].

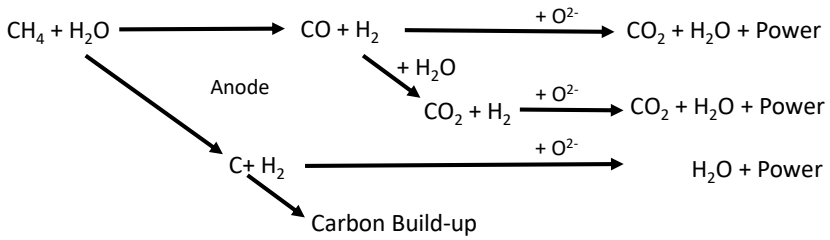

Figure 12: Possible reaction pathways in an internal reforming SOFC running on natural gas and steam [46]

2.3.4 Chemical Kinetics of Fuel-Reforming

a) Reaction Rate

According to [31], the change in concentration of a component P is defined as the reaction rate r_P of the component:

$$r_P = \frac{d[P]}{d\tau} \tag{2.49}$$

[P] in equation 2.49 represents the concentration of P. Because the concentration of educts is decreasing, their reaction rate is negative. Since products are formed in the course of a reaction, their rate of formation is positive. The ratio of the mol numbers of the used and generated components is defined by the stoichiometric coefficients of the reaction equation. The law of conservation of mass dictates that reduction of educts has to be equal to the increase of products. The general equation of the reaction rate can be written as follows [31]:

$$r = \frac{r_P}{\nu_{stP}} \tag{2.50}$$

The variable ν_{stP} in equation 2.50 is the stoichiometric coefficient of the component P. The reaction rate r is influenced by various parameters like the temperature, the pressure, the concentration of componentes and the presence of a catalyst. In general, the reaction rate can only be determined experimentally. In such experiments the concentration of a component has to be measured over time. In order to model the reaction rate [31] chooses following approach:

$$r = k \cdot [A]^a \cdot [B]^b \ \ldots \ [D]^d \cdot [E]^e \ldots \tag{2.51}$$

In equation 2.51, k describes the reaction rate constant of the reaction of interest while a, b, ... determine the reaction's order. The reaction-rate constant k depends heavily on temperature as well as pressure. The dimension of k can vary depending on the reaction order, so that the dimension of the reaction rate r becomes $mol/dm^3 s$ [31].

According to [34], two different approaches for the description of the kinetics of the heterogenous catalysed methane steam reforming reactions are common. These two apporaches are the use of an exponential equation and the Langmuir-Hinshelwood approaches. Langmuir-Hinshelwood approaches assume that the surface-coverage of the active catalyst determines the speed of a reaction. The mentioned exponential equations describe a monotonous dependency between the partial pressure of one or more educts and the reaction rate, similar to equation 2.51. For [34], exponential equations are the most common methode for describing the reforming kinetics of methane steam reforming. Therefore this thesis focuses on possible

exponential approaches to describe the methane steam reforming in greater detail.

Table 3 shows a selection of different approaches using exponential equations, compiled by [34].

Table 3: Compilation of exponential approaches for describing the kinetics of methane-steamreforming on Ni/YSZ-Anodes [34]:

Nr.	reaction-rate r [unit depends on definition]	T [°C]	P 10^5 [Pa]	E_A [kj/kmol]	Author
1	$r = k \cdot p_{CH_4}^{1}$	700 - 800	1.0	182	[43]
2	$r = k \cdot p_{CH_4}^{1} \cdot p_{H_2O}^{-1.25}$	800 - 1000	1.0	75 - 100	[33]
3	$r = k \cdot p_{CH_4}^{1.3} \cdot p_{H_2O}^{-1.2} \cdot p_{H_2}^{0.4}$	1000	1.0	-	[22]
4	$r = k \cdot p_{CH_4}^{1.25}$	-	-	-	[49]
5	$r = k \cdot p_{CH_4}^{1.4} \cdot p_{H_2O}^{-0.8}$	900	1.0	208	[4]
6	$r = k \cdot p_{CH_4}^{0.85} \cdot p_{H_2O}^{-0.35}$	-	1.0	95	[3]
7	$r = k \cdot p_{CH_4}^{1} \cdot p_{H_2O}^{1}$	840 - 920	1.0	150	[39]

b) Influence of the temperature on the reaction rate

The temperature dependence of the reaction rate constant is described by the Arrhenius equation [31, 35, 42]:

$$k = A \cdot exp\left[\frac{-E_a}{R_m \cdot T}\right] \tag{2.52}$$

With the variables in 2.53 being the frequency factor A, the activation energy E_a, the universal gas constant R_m and the temperatur T. The Arrhenius equation can be extended to model temperature dependence [31]:

$$k = A' \cdot T^b \cdot exp\left[\frac{-E_a}{R_m \cdot T}\right] \tag{2.53}$$

The activation energy represents the energy needed for a reaction to take place, as illustrated in Figure 13.

By plotting a diagram where the ordinate stands for the logarithm of the reaction rate

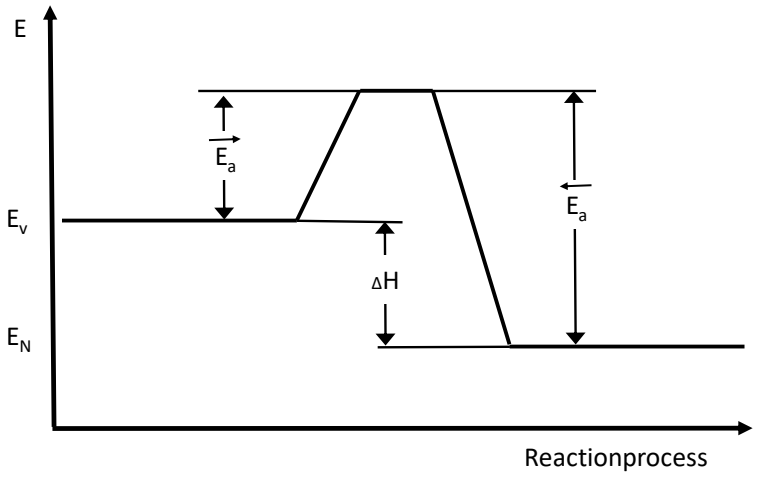

Figure 13: Principle of the energy barrier a reaction has to overcome [61]

constant $ln(k)$ and the abscissa represents the reciprocal value of the absolute temperature T, a Arrhenius-plot can be obtained. Generally, the resulting plot gives a straight line. The slope of a straight line in the Arrhenius-plot can be used to calculate the activation energy E_a, as shown in equation 2.54. Further, the intersection of the resulting straight line and the ordinate (1/T=0) is equal to the logarithmn of the pre-exponential factor A [35].

$$tan(\Phi) = \frac{E_a}{R} \tag{2.54}$$

According to [35] at least three different values of k that were obtained at different temperatures should be used to determine E_a and A.

Due to the generally high values of E_a, the exponential term is more sensitive to temperature than the pre-exponential factor A. Significant deviations from the linear behaviour can occur due to the temperature dependency of E_a and A over the course of a larger temperature range ($\Delta T > 100K$). Another possibility for nonlinear curves in Arrhenius-plots may be caused by complex reaction mechanisms or a change in the dominant mechanism in the area of interest [35].

2.3.5 Damaging Effects of Fuels

a) Damaging Effects of Carbon Depositions

Nickel has the proprensity to promote hydrocarbon pyrolysis and the buildup of carbon [52]. The buildup of carbon (coking) is a critical problem to be minimised or avoided. A problematic region is the fuel supply inlet manifold, especially the internal reforming catalyst and the anode. In these areas almost no hydrogen is present. Thus carbon-forming reactions proceed at a faster rate than the carbon removal reactions [46]. The formation of coke occurs due to cracking of hydrocarbon to the corresponding alkene. This is followed by formation of a carbonaceous overlayer that undergoes further dehydrogenation to form coke [46]. Depending on the given S/C-ratio and temperature, besides the steam reforming and watergas-shift reactions additional reactions may be of relevance. These are the endothermic methane cracking reaction (equation 2.55) and the Boudouard-reaction (equation 2.56) [34].

$$CH_4 \rightleftharpoons 2H_2 + C_{solid} \qquad \Delta_R H(T^0) = 74.8\,kJ\,mol^{-1} \tag{2.55}$$

$$2CO \rightleftharpoons CO_2 + C_{solid} \qquad \Delta_R H(T^0) = -173.3\,kJ\,mol^{-1} \tag{2.56}$$

Both reaction 2.55 and 2.56 produce solid carbon. Further, equation 2.57 states the Carbon-monoxide-reaction while equation 2.58 illustrates the deposition of carbon for general higher hydrocarbons [5, 46, 58].

$$CO + H_2 \rightleftharpoons C + H_2O \tag{2.57}$$

$$C_nH_{2n+2} \rightleftharpoons (n{+}1)H_2 + nC \tag{2.58}$$

It has to be noted that the most likely source of deleterious carbon buildup in SOFCs is the presence of higher hydrocarbons in natural gas rather than the methane itself. Nonetheless there is the possibility of utilising higher hydrocarbons such as gasoline and diesel using internal reforming SOFCs. This, however, represents a major challenge in terms of avoiding coking on any of the active components of the cell [46].The hydrogen and carbon monoxide can then react individually with oxide ions emerging from the electrolyte. Usually the conversion of CO is sluggish. Therefore the water-gas shift reaction (see equation 2.45) also occurs on the anode to produce more hydrogen [56].

A major problem with direct use of hydrocarbons as fuels in SOFCs is that the formed coke can subsequently form to block up and contaminate the anode. An excess of steam or oxygen is generally required to prevent carbon deposition and coking. Otherwise these effects result in deactivation and poor cell durability [56].

Typically, if a hydrocarbon such as methane is fed directly into an SOFC anode, the buildup of a carbon layer interrupts the function of an SOFC. Additives to the Ni+YSZ cermet can

inhibit this process. This carbon layer has two deleterious effects [56]:

- The disruption of the anode by pushing the nickel particles apart
- The formation of a barrier at the nickel surface and thus preventing gas reactions

Further results of coking are loss of reformation activity over time, loss of cell performance and poor durability. In extreme cases the growth of carbon filaments or whiskers can restrict the gas flow in the fuel supply system, eventually leading to actual physical blockades. Higher hydrocarbons are more reactive and show a much greater propensity towards carbon deposition than methane [13, 46].

The cell damaging effect of carbon depositions on the anode strongly depends on the anode used and the catalyst type. Although being the most commonly used, the Ni-YSZ anode structure has the greatest tendency to adsorb carbon. This is the case because its excellent catalyst performance enables carbon formation reactions. The carbon depositions are subsequently blocking the catalyst surface and the porous gas channels [5, 58].

An approach for classifying the formation of carbon in SOFCs is to differentiate between different formation mechanisms. One is reversible carbon deposition on the anode surface. Thereby deposited carbon can be oxidized by electrochemical reactions under the supply of oxygen ions. The other is irreversible carbon formation where carbon particulates are formed. The formed carbon particles can flow with the bulk gas streams and may clog the gas channel, causing a disturbance of the fuel gas flow. The reversible carbon depositions have no significant influence on the cell performance while the latter can cause damage in the gas flow path. Possible outcomes of the formation of carbon particulates are damage of the flow path and a change of gas partial pressures eventually leading to a decay in cell performance [32].

At high current densities, with steam and carbon dioxide being formed electrochemically and therefore with a higher oxygen partial pressure over the anode, methane can oxidise on a nickel cermet without serious carbon deposition. It is presumed that the oxidation products of the cell reform the incoming fuel. Nevertheless, it may not be practical for commercial operation to maintain a current and therefore a power density above the necessary threshold [23, 38].

b) Damaging Effects of Fuel Impurities

Damaging mechanisms regarding fuels in SOFCs can also be caused by fuel impurities. Thereby, sulphur is most prevalent. This is because typically sulphur compounds are added to natural gas as odorants to make leaks more easily detectable. Even the lower limit around

10 ppm can damage nickel electrodes. The upper limit for sulphur of around 100 ppm could cause failure in just about 1 h of operation [56]. Furthermore, hydrogen sulphide and carbonyl sulphide are also frequently present in natural gas at low levels. At low concentrations of sulphur-containing compounds the adsorption of sulphur on nickel is reversible. Thus, low concentrations of sulphur in the feed gas can be tolerated. This is especially the case when operating at higher temperatures [46].

c) Damage due to Formation of Nickel Oxide

The formation of nickel oxide at the anode of an SOFC decreases the catalytic activity for the hydrogen oxidation. Although the formation of nickel oxide is partly reversible, it has to be avoided to maximize the long term stability at high fuel utilisation. The oxidation of nickel could occur due to the reaction with H_2O and CO [44].

3 Evaluation of Test Results

3.1 Segmented Single SOFC Testbed Layout

This chapter describes the layout of the testbed used as a reference. The design and build-up of the equipment was not part of this thesis. Experimental data gathered from the described equipment was used to validate the CFD calculation as well as the testbed itself. At this point, only the equipment needed in the course of this thesis is explained. For a full description of all elements see [15, 16, 53]. Illustration 14 gives an overview of the setup. The fuel flow field

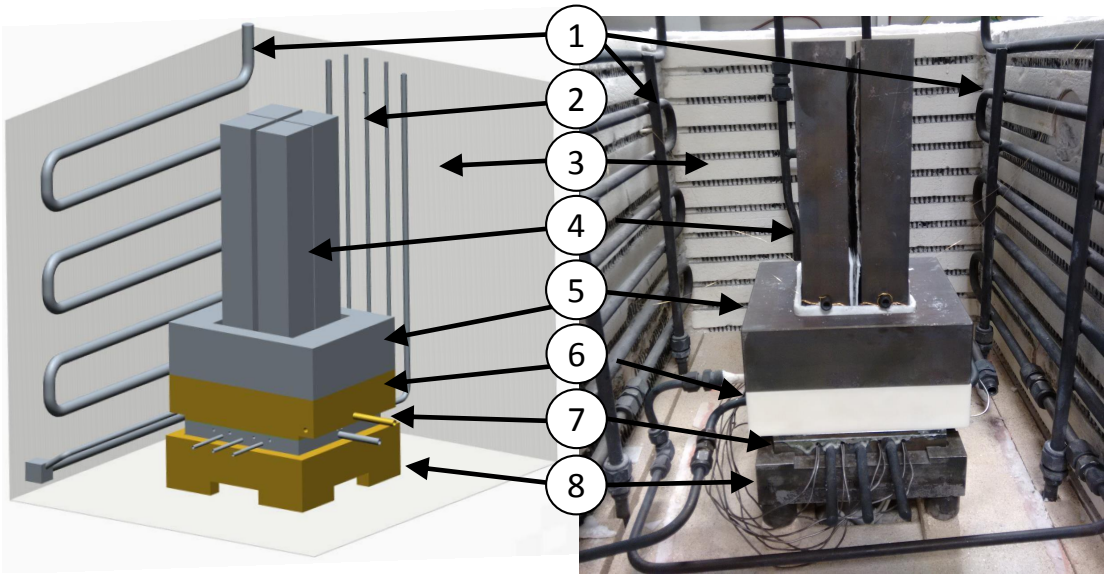

① Gas channels
② Measuring channels
③ Heated oven walls
④ Metal stamps
⑤ Metal frame
⑥ Ceramic frame
⑦ Fuel flow field
⑧ Baseplate

Figure 14: Overview of the Reference-Test Rig [8]

and the cell are assembled ⑦ (see also figure 15) and put on a baseplate ⑧. The air flow field is realised by ceramic stamps in the inside and a ceramic frame around them ⑥. The weight of a metal frame ⑤ is used to fix the ceramic frame. To establish electrical contact between the cell and the interconnect on the anode side a nickel mesh is used. The cathodes

are contacted via gold meshes placed between the ceramic stamps and the cathodes. To ensure contact, metal stamps ④ are used as weights. The operating environment of the cell is simulated by placing the cell assembly inside an oven. Heating is provided by the oven walls ③. To ensure that the fuel and air entering the cell have the same temperature as the oven environment, both are routed through the oven using meander shaped gas pipes ①. The measuring channels ② are used to transport gas drawn from the cell into a gas analyzer.

3.1.1 Flow Field and Cell Assembly

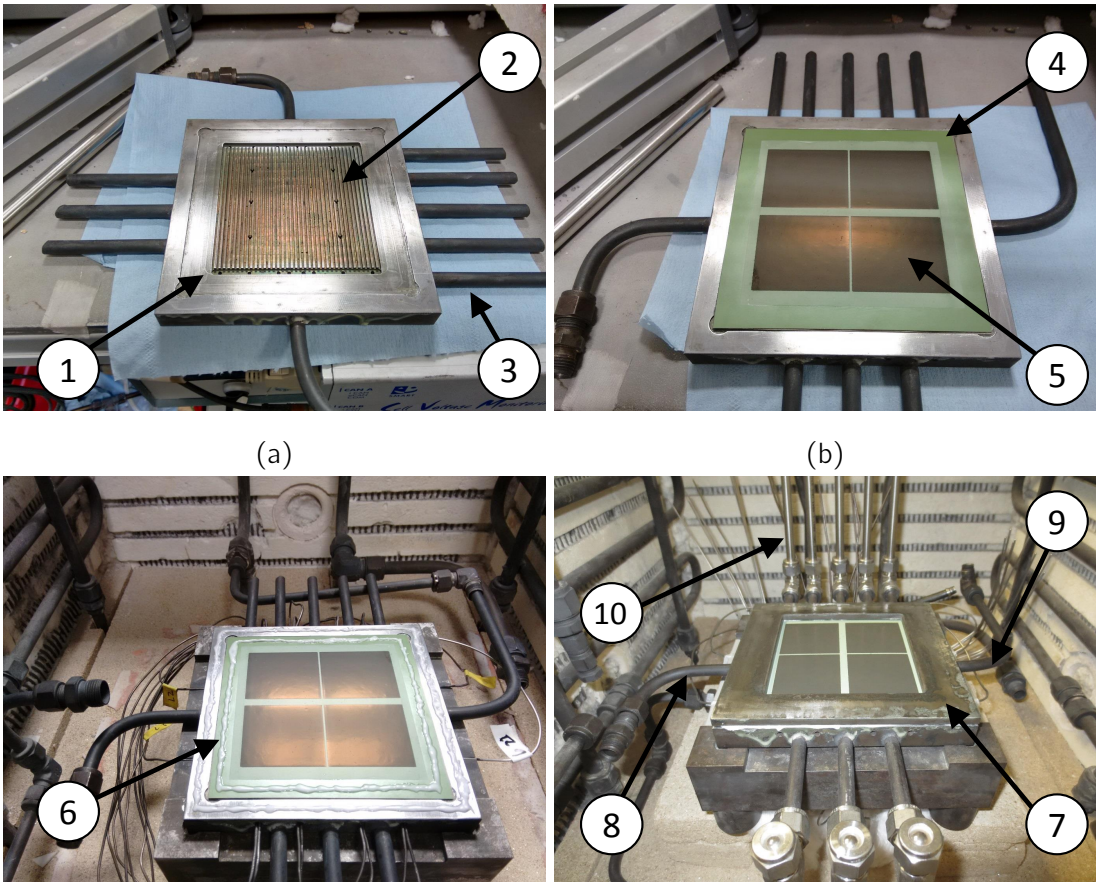

(a) (b)

(c) (d)

1 Flow field
2 Measurement holes
3 Gas channels
4 Electrolyte
5 Cathodes
6 Glass seal
7 Sealing frame
8 Fuel inlet
9 Fuel outlet
10 Measurement pipes

Figure 15: Assembly of cell and flow field [8]

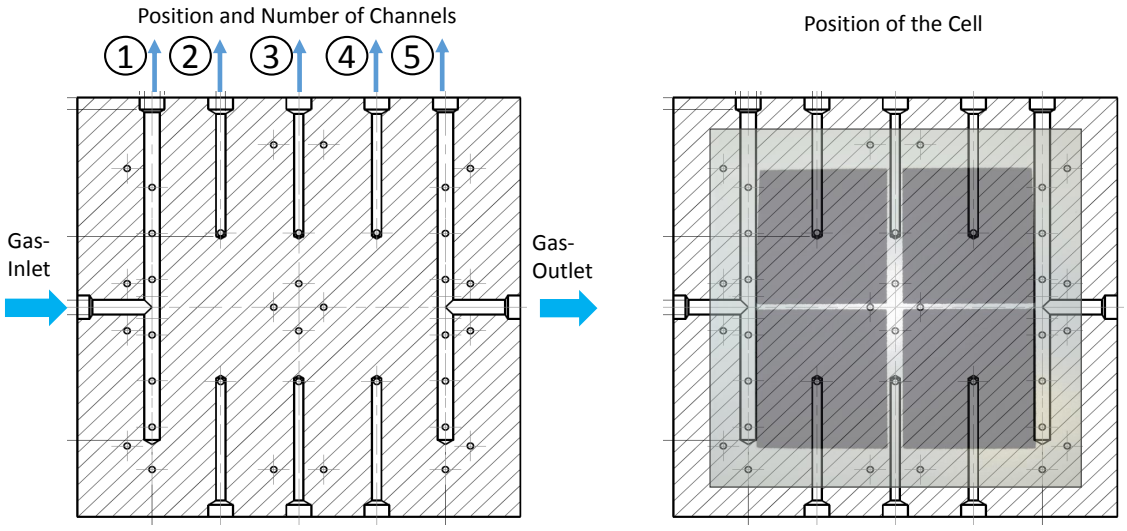

Figure 16: Position of gas channels in the flow field [8]

Figure 15 shows details of the fuel flow field and cell assembly. The fuel flow field ① also acts as the interconnect for the anode of the cell. Further, the fuel flow field also features 6 holes ②. These holes are used to draw gas from the flow field into the gas analyzer in order to measure the gas composition at the respective location (see also figure 16). The extracted gas is subsequently transported via measurement pipes ③ into a gas analyzing unit.

The fuel cell itself is placed on top of the fuel flow field with a nickel net between the two parts, as shown in figure 15-b. This is mainly to ensure electrical contact. Additionally, the nickel mesh can potentially act as a catalyst. Further, in figure 15-b the electrolyte ④ and the position of the cathodes ⑤ can be identified.

In figure 15-c the application of the glass solder ⑥ is shown. The counterpart in bonding of the flow field and the cell is the sealing frame ⑦, shown in figure 15-d. This configuration seals off the fuel flowpath and fixes the cell in the assembly. Further, in figure 15-d the pipe for fuel inlet and outlet (⑧ and ⑨) as well as the measuring pipes are visible.

a) Anode Flow Field Gas Channel Layout

All channels lie below the anode flowpath. The positions of the channels are illustrated in the cut view shown in figure 16. Channels ① and ⑤ are mixing channels. During the fuel cell's operation, anode gas flows through these channels at all times. Channels ②, ③ and ④ are

designated only for gas measurements. Using channels ① to ⑤ anode gas can be drawn for gas analysis. Figure 16 also shows the position of the cell in regard to the positions for gas measurement.

b) Measurement of Voltage and Current

Current and voltage are measured between the gold nets contacting the cathodes and the flow field. The flow field thereby acts as the anode interconnect. As shown in figure 17, the gold mesh between the ceramic stamps and the cathode is connected to the measuring equipment using five gold wires. The four outer wires are used to draw current from the cell into an electronic load. The voltage loss occuring at higher currents can not be neglected. This is especially an issue since the ohmic resistance in these wires is temperature dependent and the testbed is operated at elevated temperatures above 600 °C. To avoid incorrect voltage measurements due to voltage losses, a seperate gold wire in the middle of the gold mesh is used to measure the difference in electric potential between the anode interconnect and cathode. This wire draws only a minimal ammount of current. Voltage losses are therefore assumed to be small and will not be considered in the course of this thesis.

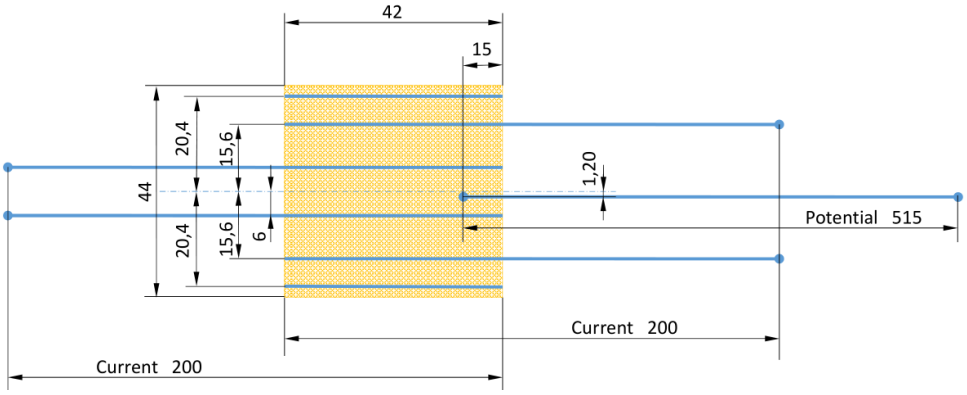

Figure 17: Sketch of a gold mesh and the contact wires for measuring current and voltage [8]

c) Temperature Measurement

The temperature distribution along the cell is measured using K-type thermocouples. According to [45], this type of thermocouple is applicable in a temperature range of -200 °C to 1250 °C. The respective standard measurement tolerance is 0.75 %. Measurements are performed at 34 different points, as illustrated in figure 18. The measuring points can

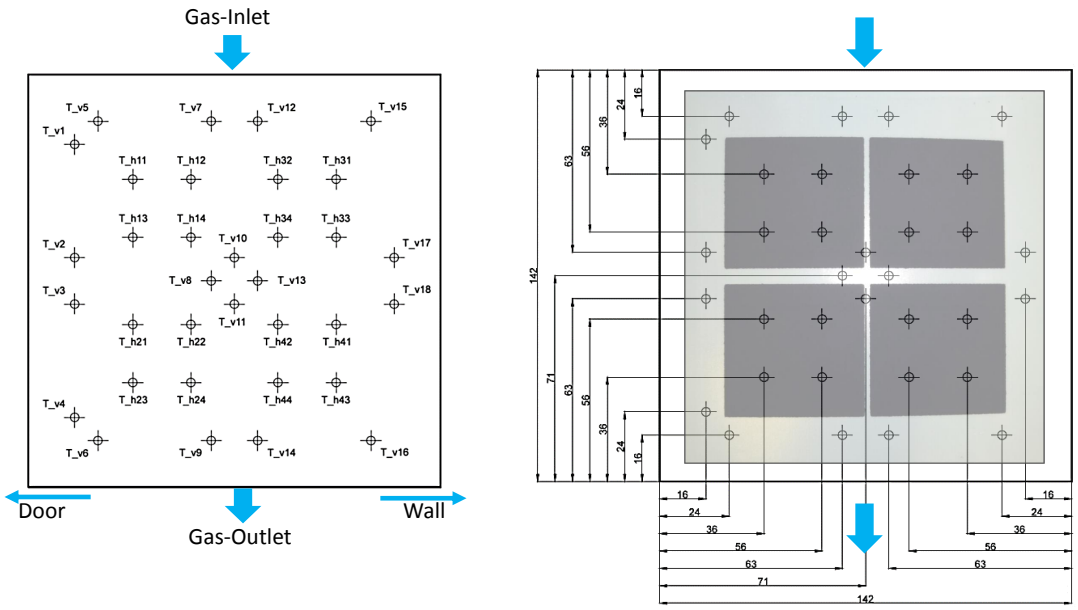

Figure 18: Position of Thermocouples [8]

be divided into two groups, depending on how the thermocouples are positioned. The 18 thermocouples T_v1 to T_v18 are positioned vertically while the 16 thermocouples T_h11 to T_h44 are positioned horizontally. Looking at the position of the cell in relation to the measured points it can be seen that the horizontally positioned thermocouples are used to measure the temperature at the cathodes. All temperatures are measured in the same plane, as illustrated in figure 19. This measuring plane ① is positioned 15 mm above the bottom of the flow field ②. Figure 19 also shows the holes from which the horizontal thermocouples are inserted ③ as well as the ports for gas analysis ④,⑤ and the fuel inlet ⑥.

3.1.2 Function of the Testbed

The principal setup of the testbed is illustrated in figure 20. A total of 47 thermocouples is placed in the testbed. These thermocouples are connected via National Instruments (NI) modules to a PC ① in order to monitor and store measured data. Valves to open the gas lines ② and mass flow controllers (MFCs) ③ to control the respective volume flow of forming gas (Arcal F5: 90 % N_2, 5 % H_2), methane (CH_4), hydrogen (H_2), nitrogen (N_2) and air can be used to set a certain fuel composition and supply the cell with air.

In order to provide the required steam for the steam reforming reaction, a seperate mixing pipe inside the oven ④ is used. The working principle of this steam generator is illustrated in 21. Air and hydrogen flow through a three-pipe-arrangement inside the oven. Using

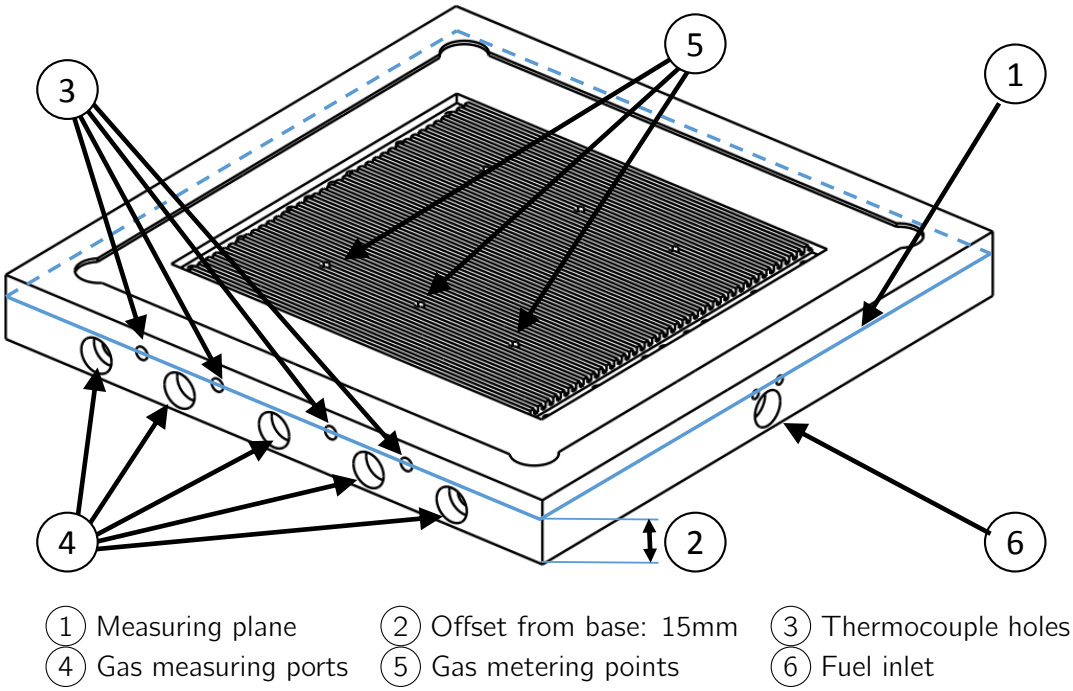

Figure 19: Flow field details and thermocouples measuring plane [8]

the elevated temperatures and a nickel mesh as a catalyst, H_2 reacts with O_2 from air to H_2O. The thereby generated steam is led outside the oven, mixed with the remaining fuel components and subsequently routed into the oven to fuel the cell ⑤. The gas analyzer ⑥ can drag fuel from the cell for analysis. Exhaust gases are filtered before leaving the testbed. Further, various auxiliary devices ⑦ are needed to supply, control and safely operate the testbed.

3.2 Measurements of the Gas Compositions in the Testbed

Using the setup shown in section 3.1, the gas mass flows and compositions as well as the temperatur distribution in the test rig can be obtained. This chapter's focus is the compilation, evaluation and verification of the raw data provided by Dufour [15].

In order to state unambiguous results, instead of the drawn current per cathode the current density will be used for further considerations. This is beneficial since the stated current was drawn seperately from all four cathodes. Figure 22 states the translation from the measured current to the respective current densities via cell geometry.

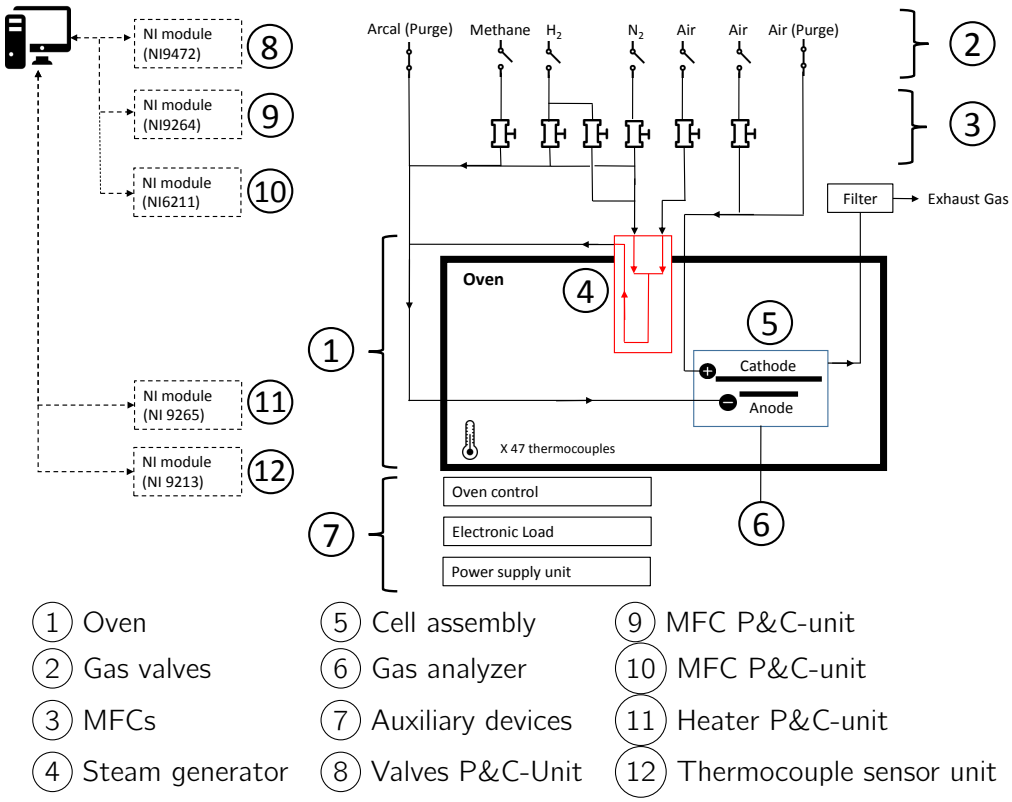

Figure 20: Schematic of the test rig [8]

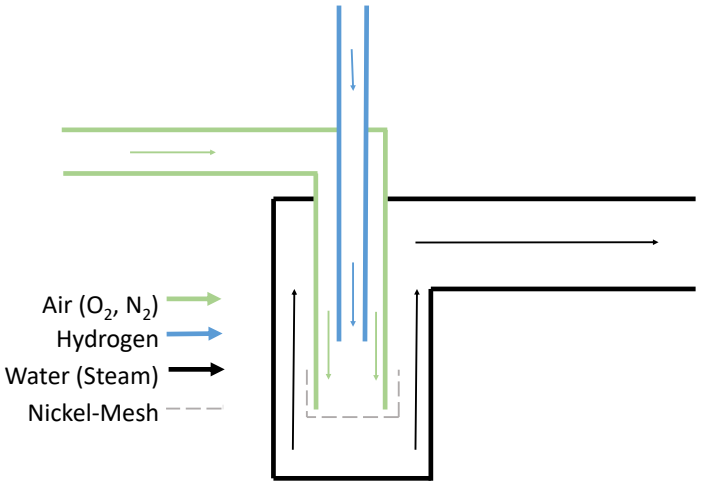

Figure 21: Scheme of the Steam-Generator (KitKat) [8]

As described, the gas flows are set by MFCs. Using the set values and the equation for ideal gases as well as the gas constant of each component (see table 5), the mass flows

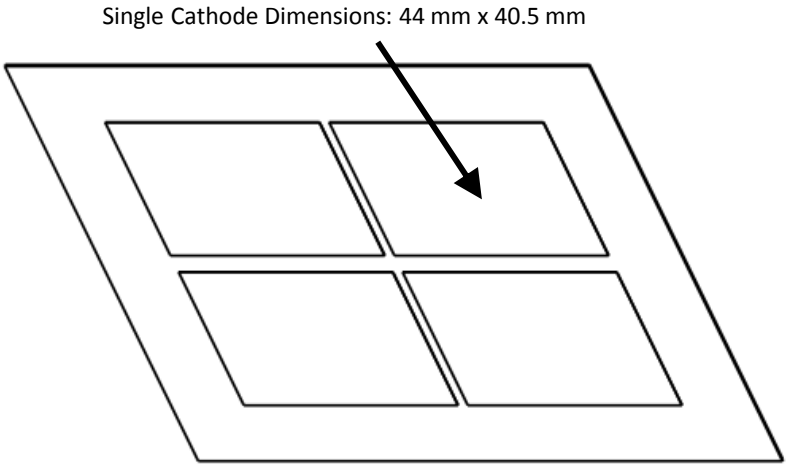

$I_{Segment}$ [A]	i $[\frac{mA}{cm^2}]$
0	0
1	56
2	112
3	168
4	224
5	280
6	336
7	393
8	449
9	505
10	561
11	617
12	673

Figure 22 & Table 4: Translation from current to current-density for a single cathode

Table 5: Gas constants of the occuring species

R	CH_4	H_2	O_2	N_2	H_2O
$[\frac{J}{kgK}]$	518,353	4124,237	259,827	296,839	461,401

and compositions of the gases entering the system can be obtained. Therefore, the fuel composition entering the testbed is known. The composition of air is assumed to be 79 vol-% N_2 and 21 vol-% O_2. The according values are stated in table 6-a.

Table 6: Fuel gas composition
(a) Fuel composition as set by MFCs [15]
(b) Assumed fuel composition after steam generator

	$\dot{V}$ [Nl/h]	$\dot{m}$ [g/h]	ν [-]
CH_4	14.50	11.09	0.09
H_2	37.50	3.37	0.23
O_2	17.18	24.53	0.10
N_2	96.82	120.99	0.58
$\sum$	167.00	159.99	1.00

(a)

	$\dot{V}$ [Nl/h]	$\dot{m}$ [g/h]	ν [-]
CH_4	14.50	11.09	0.10
H_2	3.14	0.28	0.02
H_2O	34.39	27.62	0.23
N_2	96.82	120.99	0.65
$\sum$	149.82	159.99	1.00

(b)

Assuming a complete reaction of hydrogen and oxygen to steam in the steam generator, the fuel composition stated in table 6-b is expected at the inlet of the cell.

Table 7: Air composition as set by MFCs [15]

	$\dot{V}$ [Nl/h]	$\dot{m}$ [g/h]	ν [-]
O_2	31.50	44.97	0.21
N_2	118.50	148.09	0.79
$\sum$	150.00	193.06	1.00

3.2.1 Determination of wet Gas Composition from dry Measurements

As illustrated in figure 16 of chapter 3.1, gas measurements are performed on five positions along the cell. A main drawback of these measurements is that all the H_2O in the probed gas compositions is condensed by the gas analyzer. Therefore, the measured mole fractions refer to a dry gas composition. In order to obtain valid results of the actual mole fractions of the gas at the measured points, the mole fractions including H_2O need to be calculated. A good approximation can be achieved by using the data of the mole flows entering the testbed determined by the MFCs. Thereby it is assumed that no other species than the ones accounted for by the MFCs enter the system and no leakage occurs.

Due to its inert behaviour no change in the molar stream of the species N_2 is expected. Based on the measurements of the dry volume fractions of channel 1 to 5 (see figure 16), the dry molar flows of the measured species can be determined. This is done by assuming the difference between the sum of the measured percentages and 100 % to be the volume fraction of N_2. Using the known molar flow of N_2 determined by the MFCs as a reference and the dry mole fractions determined by the gas analyzer, the dry molar flow of all measured species can be calculated.

In order to obtain the gas composition also including H_2O as a species, the balance of atoms at each point is assumed. The total molar flow of all atoms entering the system is measured by the MFCs. Subsequently, the difference in H- and O- atoms to the measured values of the gas analyzer is assumed to be in the form of H_2O. That is, if the needed ratio of 2 hydrogen atoms to 1 oxygen atom is applicable.

The validity of the calculation was checked by a second method to find the molar flow of H_2O. Thereby the molar flows of the dry fuel composition based on the results of the gas analyzer were calculated as described above. The molar flow of H_2O was subsequently determined by assuming the difference between the molar flow measured by the MFCs and the calculated dry molar flow to be H_2O. The results show good accordance. Further, the deviation between the molar flow of elements measured by the gas analyzer and the molar flow set by the MFCs has been evaluated. Detailed results can be found in the appendix.

A major limitation of the described procedure is that it is only applicable if no current is

drawn from the fuel cell. Reason for this is the transport of oxygen ions from cathode to anode which subsequently renders atom balances invalid. However, since the knowledge of the wet composition is needed to evaluate the obained measurements, the calculated wet fuel compositions along the cell are used for detailed investigations of reforming kinetics at OCV.

3.2.2 Gas Composition at Cell Inlet and Outlet

As illustrated in figure 23, the measured fuel composition at the cell inlet (Channel 1) is not constant with the temperature. This indicates that reformation already occurs at some point between where the gas flow is set and the first gas metering point at the cell inlet. In theory, assuming that no reforming happens in the fuel pipes inside the oven, no methane should have been reformed until this position.

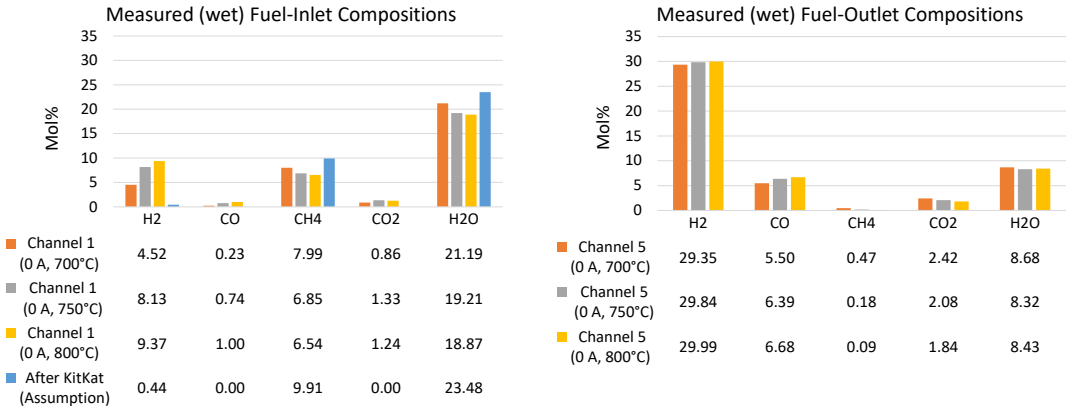

(a) (b)

Figure 23: Influence on temperature on fuel composition.
(a) Comparison of measured fuel inlet compositions
(b) Comparison of measured fuel outlet compositions

One possible explanation for the different inlet compositions is that a major part of the reforming happens in the catalysed environment at the cell anode itself. In this case reformed gas would be sucked out of the flow field. This, however, seems unlikely since the channels 1 and 5 do not suck fuel directly from the flow field but from common mixing channels (see chapter 3.1). Another possibility is that steam reforming also takes place in the fuel pipes inside the oven which are connected to the cell inlet. A further finding displayed in figure 23 is, that the fuel composition at cell outlet (measuring channel 5) shows little temperature dependence. The working theory at this point is that the gas composition at cell outlet is near the equilibrium composition for the respective temperature. Therefore, figure 24 states the measured gas compositions at cell outlet as well as the equilibrium composition for the

operating temperatures of the test rig. The equilibrium compositions were obtained using a Matlab tool provied by AVL [8], which operates by minimizing the Gibbs enthalpy. The results shown in figure 24 indicate that for all temperatures the fuel composition at cell outlet is near the equilibrium composition.

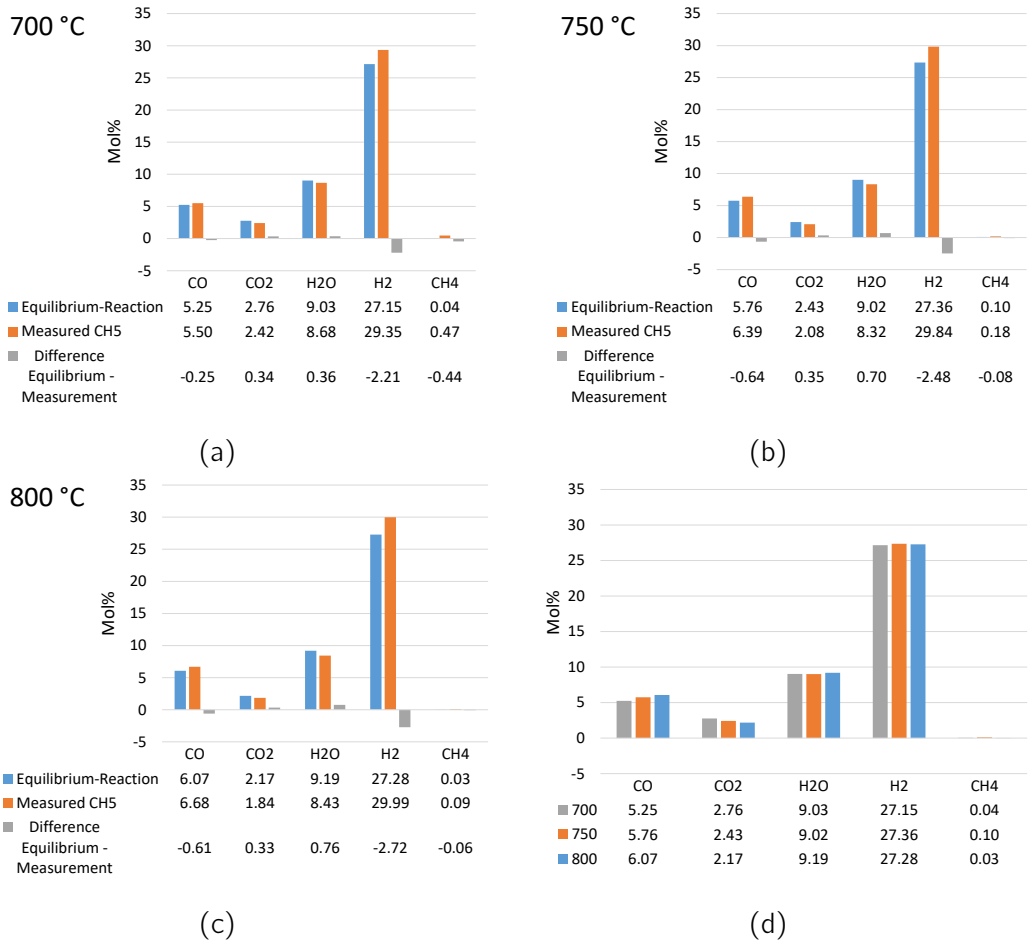

Figure 24: Comparison of measured gas compositions at channel 5 and gas composition through equilibrium reaction
(a) 700 °C (b) 750 °C (c) 800 °C
(d) Comparison of the respective equilibrium compositions

In order to eliminiate the possibility of a systematic measuring error in the data provided by Dufour [15], the validity of given results was investigated. This was necessary since the data gathered from the testbed is subsequently used as boundary conditions for CFD simulations. Therefore, in the course of this thesis, a seperate test run of the test rig was conducted.

3.2.3 Validation of provided Raw Data via seperate Test Run

The aim of the performed test run was to check where in the test rig the reformation of the methane in the fuel composition is likely to take place. Further, an estimation on how much fuel is reformed not on the anode of the cell but in the fuel pipes inside the oven should be given.

a) Experimental Procedure

In order to determine how much fuel reforming takes place specifically in the fuel pipes inside the oven, the segmented cell structure inside the oven is bypassed. Gas for analysis is drawn directly from the end of the fuel pipe inside the oven. Doing so, it is ensured that if a change in the gas composition is measured this change can only be due to reforming in the fuel pipes. The segmented cell structure itself is kept inside the oven, so that as little changes as possible are made to the test rig. Measurements of the species CH_4, H_2, CO and CO_2 were performed at 700, 750 and 800 °C. Temperatures were held at a constant level until an even temperature distribution inside the oven was established. Doing so, stable reforming conditions were realized. The fuel composition stated in table 6-a was mixed from H_2, CH_4, N_2 and air. The respective mass flows were set by MFCs. The steam required for the steam reforming of methane was generated using the steam generator described in section 3.1.

b) Calibration of Measuring-Equipment

Following the manual [1], the gas analyzer was calibrated seperately using pure N_2 as zero-point gas as well as pure CH_4, H_2 and air to calibrate the endpoint of the scale. Air was thereby assumed to be 79 % N_2 and 21 % O_2. The calibration for the species CO and CO_2 could not be performed. Therefore the respective factory settings were used. The temperature inside the oven was measured by a K-type thermocouple placed in the middle of the oven. The installation and calibration of this sensor was performed previously by Dufour [15].

c) Results and Interpretation

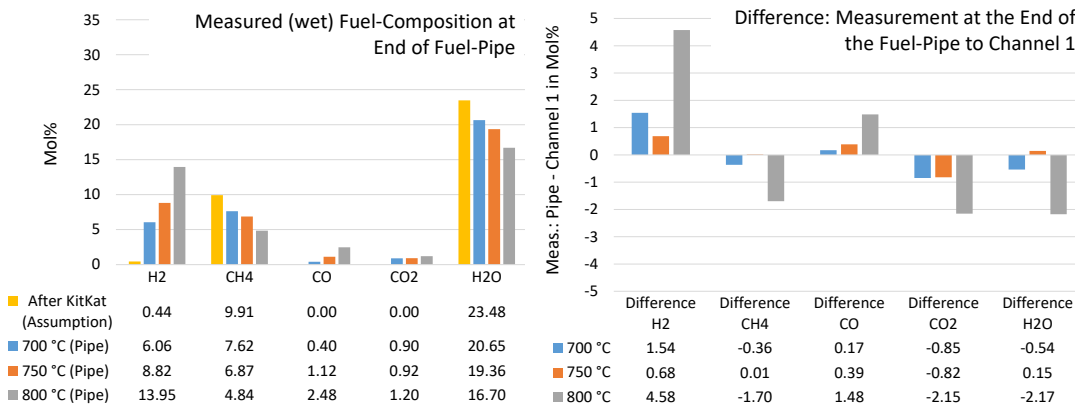

(a) (b)

Figure 25: Validation of fuel composition at cell inlet
(a) Measured fuel composition at end of fuel pipe
(b) Comparison of measurements at fuel pipe outlet (figure 25-a) to measurements at channel 1 (figure 23-a)

It can be seen from figure 25 that the measured fuel compositions through reforming processes in the fuel pipes leading to the cell inside the oven at 700 °C and 750 °C show good accordance to the composition at the inlet of the cell (channel 1) measured by [15].

However, a deviation for the results at 800 °C is noticeable. A pre-startup inspection of the testbed showed a gas leak, which might be a possible explanation for this. It was corrected before the test described was conducted. This gas leak might have also been present during the measurements performed by [15]. Another possible source for the deviation between the two measurements is that in order to correct the gas leak, the insulation of the steam generator had to be replaced. The renewed insulation might have provided better damming. This could have led to a higher efficiency of the steam generator subsequently leading to a better conversion of methane.

It is concluded that the deviations between the theoretical fuel composition assuming no methane reforming and the measured fuel compositions at the inlet of the cell (channel 1) result from steam reforming inside the fuel pipe leading to the cell. A likely explanation is that the nickel fraction (see table 8) in the used material acts as a catalyst. Therefore the measured fuel composition at the cell inlet at the respective temperature is used as the boundary condition for the fuel composition in further CFD analysis.

Table 8: Chemical composition of X15CrNiSi25-21 in mass% [19]

	C	Si	Mn	P	S	Cr	Ni	N
min.	-	1.5	-	-	-	24.0	19.0	-
max.	0.2	2.5	2.0	0.045	0.015	26.0	22.0	0.11

3.2.4 Gas Compositions along the Cell

To make a valid statement about the composition of the fuel gas along the cell, the flow of oxygen ions from the cathode to the anode has to be taken into consideration. The four cathodes draw current seperately. The corresponding mass flow is calculated using the Faraday equation [26] as stated in 3.1.

$$\dot{m}_{O_2} = \frac{I \cdot n_{cat} \cdot M_{O_2}}{z \cdot F} \tag{3.1}$$

The variables in equation 3.1 are the current drawn per cathode I, the number of cathodes in the system n_{cat}, the molar mass of oxygen M, the charge number of oxygen z and the Faraday constant F. Using equation 3.1, the volume flow at standard condiditions can be determined, as stated in equation 3.2.

$$\dot{V}_{O_2} = \dot{m}_{O_2} \cdot \frac{T_N \cdot p_{measure}}{p_N \cdot T_{measure} \cdot \rho_{O_2}} \tag{3.2}$$

Figure 26: Plot of the calculated oxigen flow over current density (a) and calculated values according to equations 3.1 and 3.2 (b)

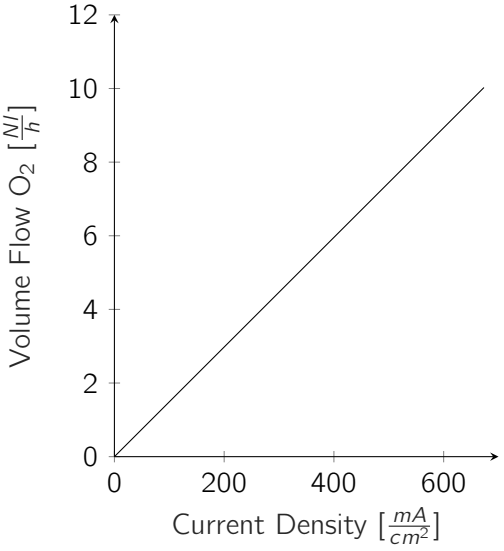

(a)

i $[\frac{mA}{cm^2}]$	$\dot{m}_{O_2}$ [g/h]	$\dot{V}_{O_2}$ [Nl/h]
0	0.000000	0.000000
56	0.000332	0.835499
112	0.000663	1.670997
168	0.000995	2.506496
224	0.001327	3.341995
281	0.001658	4.177493
337	0.001990	5.012992
393	0.002322	5.848490
449	0.002653	6.683989
505	0.002985	7.519488
561	0.003316	8.354986
617	0.003648	9.190485

(b)

The variables T_N and p_N refer to the pressure and temperature at standard state (T_N=273.15 K, p_N=101325 Pa).The resulting values for the flow of oxygen in the considered current range are stated in figure 26.

Therefore, the total amount of oxygen flowing from cathode to anode is known. However, the distribution of the oxygen flow from the cathode to the anode can not be determined based on given measurements. As a consequence, the gas composition for a single point in the anode flow field can not be determined. For further analysis, at operating points other than OCV, the measured dry results are used. Subsequently, the measured gas compositions are displayed in figures 27, 28 and 29. The plots show the change of the measured dry gas species from channel 1 to channel 5 at 700 °C, 750 °C and 800 °C. It can be seen that the three test series show qualitatively the same results.

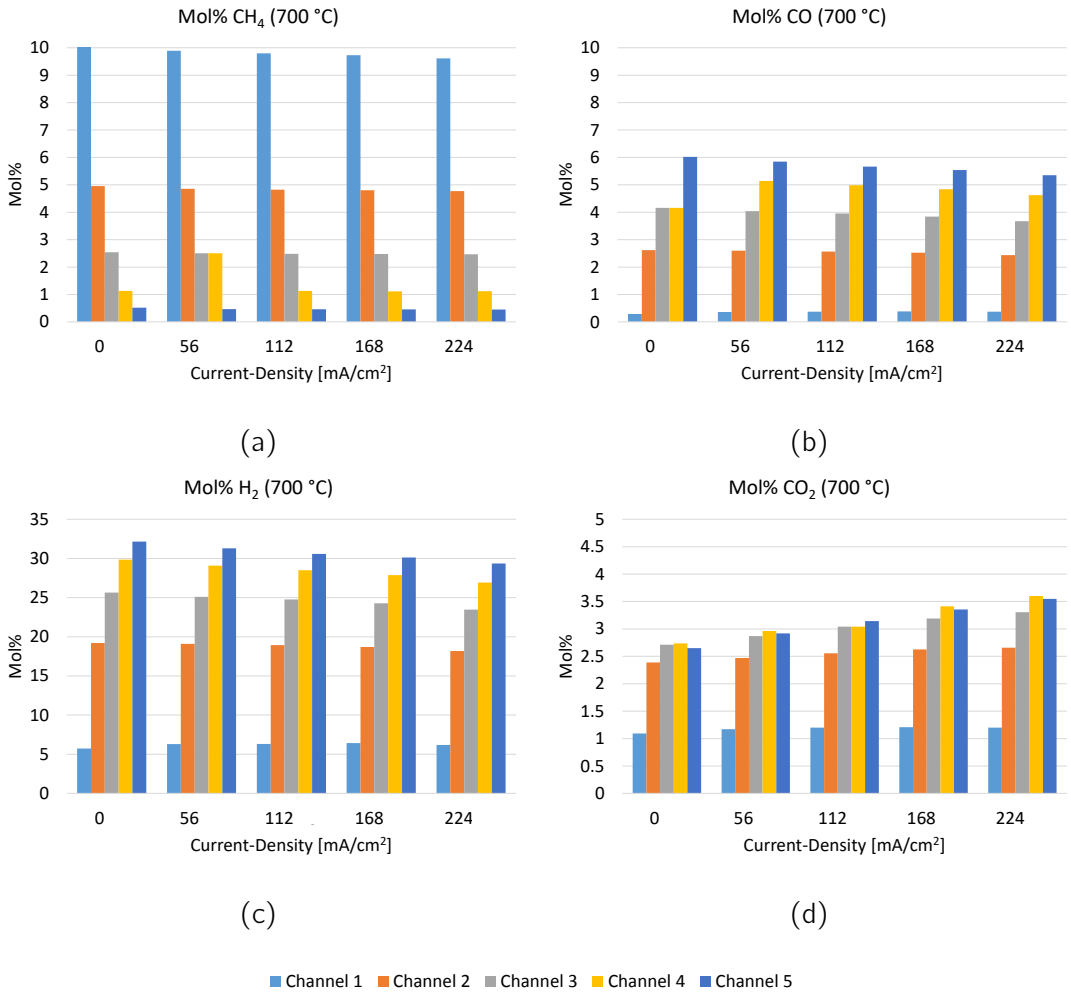

Figure 27: Plots of measured species (dry) along the cell at 700 °C

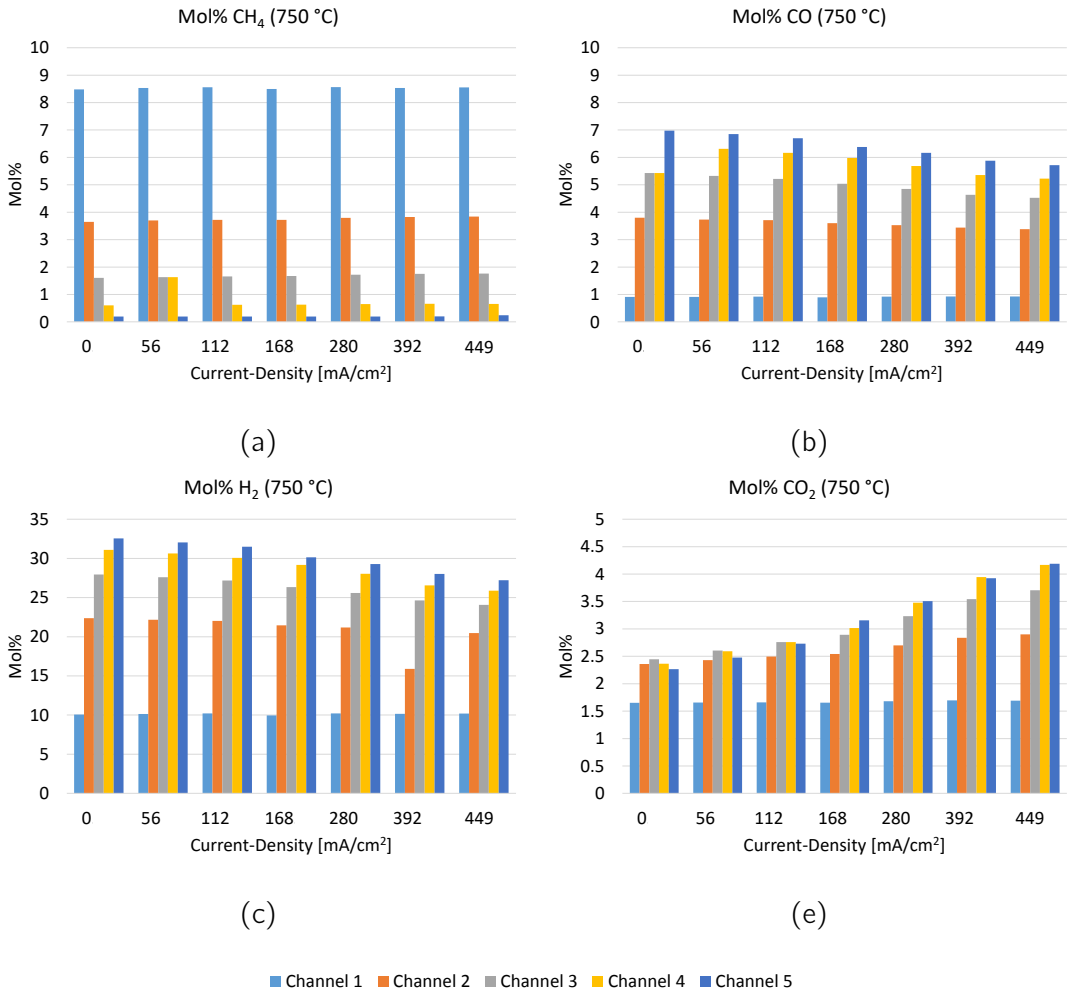

Figure 28: Plots of measured species (dry) along the cell at 750 °C

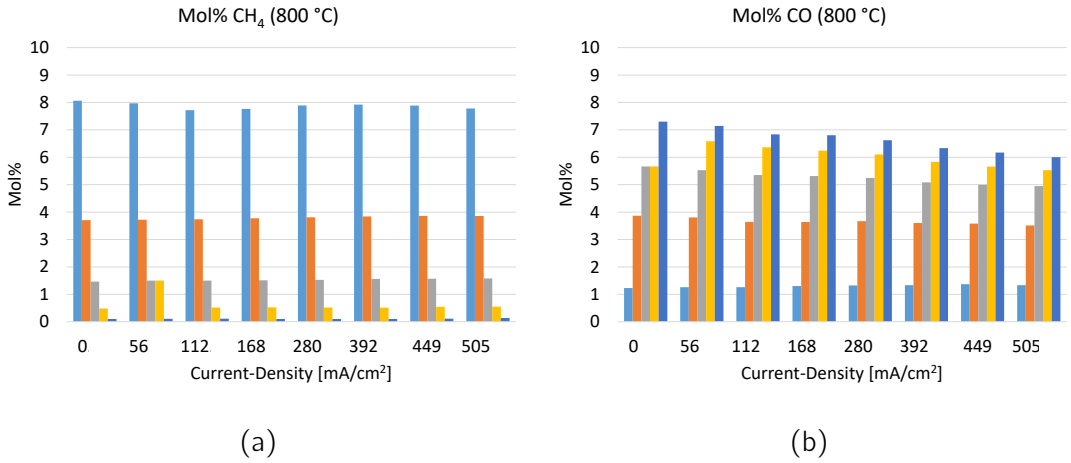

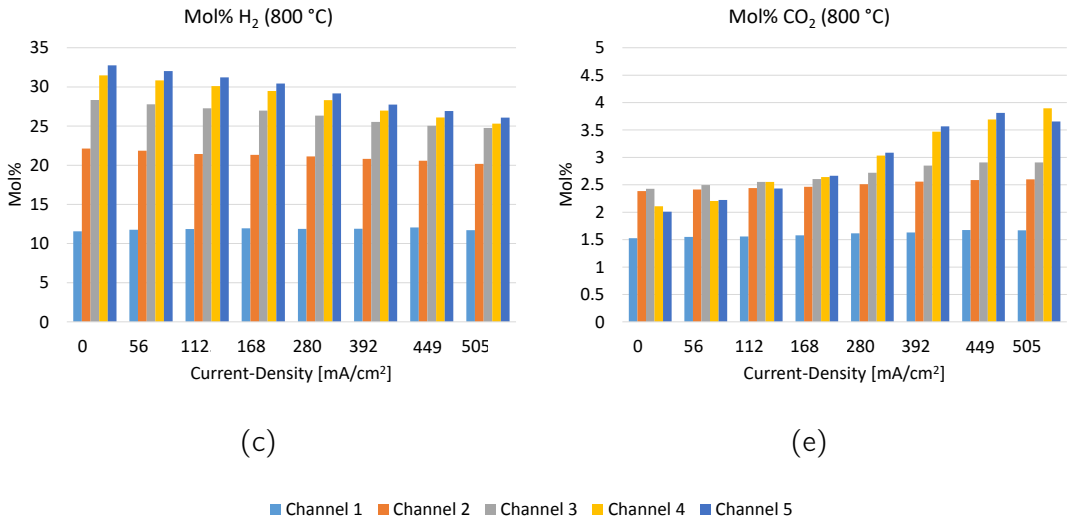

Figure 29: Plots of measured species (dry) along the cell at 800 °C

As shown in the figures 27-a, 28-a and 29-a, the concentration of CH_4 displays no correlation with the current density. It is concluded that the reforming activity (see section 2.3.3) in the testbed is independent of the drawn current. The plots show that the highest reforming activity takes place at the beginning of the flow field where the concentration of CH_4 is the highest. This is plausible, since a species' reaction rate depends on the respective concentration. Further, it is in good agreement with literature (e.g. [34], [61]).

Steam reforming implicates the increase of the products CO and H_2 with a decrease of the educt CH_4 (see chapter 2). This behaviour is supported by the measured data. The decrease in the concentration of CH_4 occurs simultaneously to the increase of H_2 and CO (see figures 27, 28 and 29 (a,c). The increase of CO_2 along the cell further indicates the presence of the water-gas shift reaction.

With increasing current density, a decrease in the concentrations of CO and H_2 can be noted. Most prominent explanation for the decrease in H_2 is it's electrochemical consumption as a fuel. The decrease of CO can bei either due to its consumption as fuel or its role as educt in the water-gas shift reaction. Contrary to the behaviour of CO and H_2, the mole fraction of H_2O increases at higher current-densities. A possible explanation for this behaviour is the reaction of carboneous gases with oxygen transported through the cell at higher currents (see figure 3.2).

3.3 Evaluation of measured Temperature Profiles

As described, the temperature distribution in the testbed is measured using a total of 47 thermocouples (for details see section 3.1). Unfortunately, these thermocouples displayed considerable deviations to each other as well as to the set temperature in the oven. A possible reason for this could be the use of seperate National Instruments (NI) devices. Further, a temperature drift of the various thermocouples to one another can not be ruled out. Since the amplitudes of these deviations are in the same order as the expected temperature differences to be measured, this systematic measurement error represents a major obstacle for further analyzing the temperature data.

The problem was solved by using the temperatures of all thermocouples inside the testbed and forming a mean temperature as reference. This average temperature was calculated using temperature values measured at an operating point where no current was drawn from the cell and reforming in the anode flow field could be ruled out.The difference of the various measured temperatures to the calculated mean temperature was used as a correcting value for all thermocouples. Therefore, only the deviations of the various measuring points with regard to the reference temperature are taken into consideration.

Figure 30 illustrates the effects of this process. It shows the temperature distribution at 800 °C using methane as fuel at a current density of $[i = 281\ \frac{mA}{cm^2}]$ before (30-a and 30-b) and after the application of correcting values (30-c and 30-d). The points on the edge of the plot are assumed to be at oven temperature. This procedure provides plausible temperature distributions for all measured points. In the shown example the temperature drop due to the reformation of methane is clearly visible.

The validity of the absolute values of the resulting temperatures, however, can be seen as limited. Nonetheless the resulting temperature distribution represents a good indication for further analysis and comparison to the results obtained by CFD simulations.

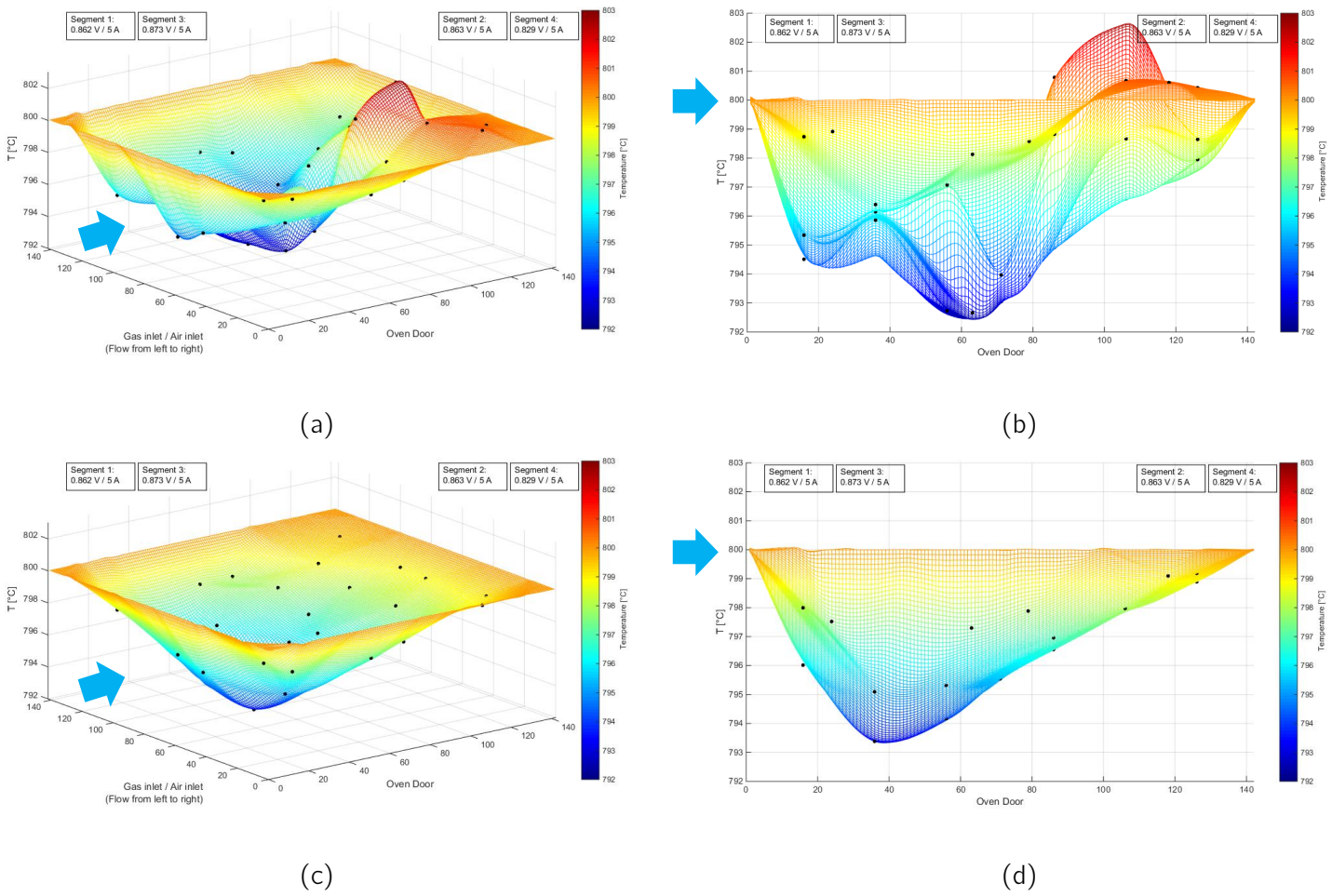

Figure 30: Comparison of uncorrected (a, b) and corrected (c, d) plots for measured temperature distribution. Exemplary measured point at 800 °C and a current density of $i = 280\ \frac{mA}{cm^2}$ using methane as fuel. Temperature at boundary assumed as 800 °C.

4 CFD Simulation of the Single SOFC Test Rig

4.1 Used CFD Model

The CFD model used was developed in a series of theses. Table 9 gives a short overview on the development of the model.

Table 9: Version history of the used CFD model

	Model	**Nr. Cells**	**Cell Types**	
1	Rasinger [51]	6719331	· Hexaeder · Tetradeder	· thermal flow implemented · no electrochemistry implemented
2	Schaffer [53]	8305582	· Hexaeder	· complete rebuild of the model · electrochemistry implemented · validated results using H_2 as fuel
3	Gitz [18]	10616600	· Hexaeder	· minor accuracy improvements
4	Rachinger	8956972	· Hexaeder	· validated results using CH_4 as fuel

As shown in table 9, the used CFD model is based on the model by Daniel Schaffer. The detailed description of the mesh itself, as well as the corresponding cell- and face selections, can be found in his thesis [53].

Figure 31 gives a short overview of the modelled components. All neccessary changes to the model will be discussed in detail. Further, in order to ensure confirmability, all relevant settings in FIRE® as well as the the parameters used for porosity ϵ, tortuosity τ, thermal conductivity λ, specific heat capacity c and electrical conductivity σ of all implemented components are stated in the appendix.

The emphasis of this thesis lies on the simulation and validation of CH_4 as fuel. Therefore the following chapter's focus is the determination and implementation of the corresponding FIRE® settings.

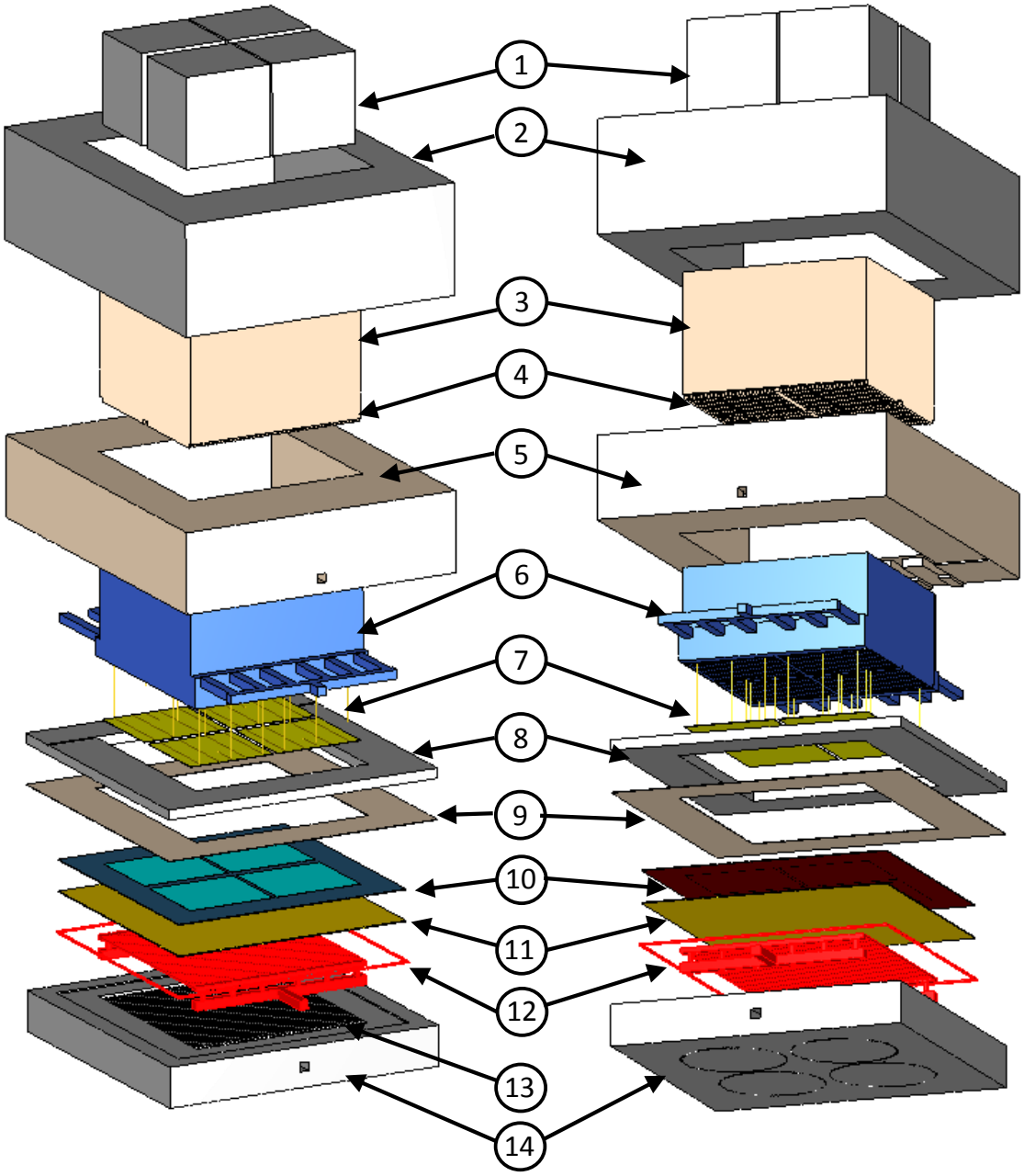

1 Metal weights
2 Metal frame
3 Ceramic stamps
4 Flow field air
5 Ceramic frame
6 Air
7 Cathode interconnect
8 Metal sealing frame
9 Glass solder
10 Fuel cell
11 Nickel mesh
12 Fuel
13 Flow field fuel
14 Anode interconnect

Figure 31: Explosion view of the CFD volume selections

4.2 Adaption of the existing CFD Model

Adaption of the Boundary Conditions for the Exterior Walls

The previous model was set up to simulate heating elements at the bottom of the cell test housing. These heaters were used to set a certain temperature profile inside the housing [18, 53]. However, the tests using a methane mixture as fuel were conducted without using heating elements. Therefore the temperatures at all exterior boundary conditions (BC) were set to be the constant value of the oven temperature.

Adaption of the Boundary Conditions for the Fuel Inlet

As shown in chapter 3, the fuel composition at the cell inlet depends on the ambient temperature of the cell housing set by the oven. In order to perform simulations at the corresponding temperatures, the fuel composition at the cell inlet has to be adapted. To account for this temperature dependence, the adapted wet composition based on the performed dry measurements at channel 1 are used as part of the BCs for the fuel inlet. The respective fuel compositions are stated in table 10.

Table 10: Fuel inlet compositions for CFD

T	H_2O [-]	H_2 [-]	CH_4[-]	CO [-]	CO_2 [-]	N_2 [-]
700 °C	0.211900	0.045150	0.079880	0.0022800	0.008618	0.6521720
750 °C	0.192100	0.081330	0.068520	0.0073530	0.013330	0.6373670
800 °C	0.188730	0.093700	0.065400	0.0095500	0.012390	0.6298300

Adaption of the Cathode Boundary Condition

In the course of this thesis, CFD calculations simulating drawn cell currents have shown the tendency to cause numerical problems. After consulting development engineers at AVL AST [9], to avoid these problems the current was linearly ramped up over a certain amount of iterations to the desired value. The implemented formula is stated in the appendix.

Adaption of the Convergence Criteria

Convergence criteria are used to determine if the result of a calculation has the desired accuracy. They are used as an indicatator if a calculation can be terminated or more iterations are necessary to improve the accuracy of the result [7]. In order to improve the validity of the results, the convergence criteria were tightened. Table 29 summarizes the convergence criteria used.

Table 11: Convergence Criteria

Iteration Limits		
Max. nr. Iterations	10000	
Min. nr. iterations	3	
Use Normalized Residuals		
Criterion	**Used**	**Value**
Pressure	YES	1e-006
Momentum	YES	1e-006
Turb. kin. energy	NO	0.0001
Turb. diss. rate	NO	0.0001
Energy	YES	1e-006
Scalar	NO	5e-008
Volume fraction	NO	0.0001
Electric potential	YES	1e-006

4.3 Fitting the Simulation to measured data

In the following section, the adjustment of the calculation to measured data (fitting) is described. First, the chemical kinetics are fitted at OCV to the measured gas compositions along the cell. Thereby it is assumed that cell operation has no influence on the investigated chemical reactions. Second, after the chemical kinetics show good accordance to measurements, the parameters for the electrochemistry are adjusted. Main goal for fitting the electrochemistry was a good agreement of measured and simulated IV-curves.

4.3.1 Reforming Reactions in FIRE®

In order to simulate hydrocarbon fuels, equation 4.1 and 4.2 are implemented in FIRE® [10]:

$$C_nH_mO_p + (\mathrm{n}-\mathrm{p})\mathrm{H_2O} \longleftrightarrow \mathrm{nCO} + (\mathrm{n}-\mathrm{p}+\frac{m}{2})\mathrm{H_2} \tag{4.1}$$

$$\mathrm{CO} + \mathrm{H_2O} \longleftrightarrow \mathrm{CO_2} + \mathrm{H_2} \tag{4.2}$$

Equation 4.1 is a general form of the endothermic hydrocarbon steam reforming reaction, while 4.2 states the exothermic water-gas shift reaction. For a detailed discussion on reactions and reaction mechanisms see chapter 2.2. Both reactions are modelled as one-step volume reactions. The volume region of the specific reactions can be restricted using an executable provided by the engineers developing FIRE® at AVL AST [9]. This is necessary, because the reactions taking place are influenced by catalytic materials, such as nickel.

The reactions 4.1 and 4.2 produce the following species mass sources in the species transport equations [10]:

$$M_{H_2} \cdot r_{H_2} = M_{H_2} \cdot [(n-p+\frac{m}{2}) \cdot r_{reform} + r_{shift}] \tag{4.3}$$

$$M_{H_2O} \cdot r_{H_2O} = M_{H_2O} \cdot [-(n-p) \cdot r_{reform} - r_{shift}] \tag{4.4}$$

$$M_{CO} \cdot r_{CO} = M_{CO} \cdot [n \cdot r_{reform} - r_{shift}] \tag{4.5}$$

$$M_{CO_2} \cdot r_{CO_2} = M_{CO_2} \cdot r_{shift} \tag{4.6}$$

$$M_{C_nH_mO_p} \cdot r_{C_nH_mO_p} = -M_{C_nH_mO_p} \cdot r_{reform} \tag{4.7}$$

Equation 4.8 states the reaction rate for steam reforming while the reaction rate of water-gas shift is stated in equation 4.9 [10]:

$$r_{reform} = k_{f,reform} \cdot c_{C_nH_mO_p} \cdot c_{H_2O}^{n-p} - k_{b,reform} \cdot c_{CO}^{n} \cdot c_{H_2}^{n-p+\frac{m}{2}} \tag{4.8}$$

$$r_{shift} = k_{f,shift} \cdot c_{CO} \cdot c_{H_2O} - k_{b,shift} \cdot c_{CO_2} \cdot c_{H_2} \tag{4.9}$$

k_f and k_b in equations 4.8 and 4.9 are the rate constants for the forward reaction and the backward reaction [10] respectivley. The rate constant for the forward reaction k_f is calculated using the extended Arrhenius equation, as described in chapter 2.3.4 [10]. For the backward reaction, the rate constants for the steam reforming of methane and the water-gas shift reaction, as stated in chapter 2.3.3, are used. Therefore, the backward reaction of each reaction is obtained using the respective equilibrium constant K_{eq}, as stated in equation 4.10.

$$k_b = \frac{k_f}{K_{eq}} \tag{4.10}$$

The chemical reactions produce heat sources in the enthalpy equation, as described by

following equation [10]:

$$\dot{Q}_{react} = -\sum_{j=1}^{n_s} \left[\dot{r}_j \cdot M_j \cdot \left(h_j + j_{j,ref}\right)\right] \tag{4.11}$$

The variables h_j and $h_{j,ref}$ in equation 4.11 are the enthalpy of formation at the local temperature and the reference temperature.

According to [10] and [11], reaction 4.1 only occurs on the surface of the anode, while 4.2 takes place in the porous void volume of the anode. Using this approach the methane reforming rate necessary for achieving accordance with the results from the testbed could not be achieved. In accordance with the responsibe FIRE® development engineers [9], the volume region of the methane reforming in the CFD model was expanded to the anode and the nickel mesh.

4.3.2 Fitting of the Chemical Kinetics

The following section explains the fitting of the chemical kinetics to achieve simulation results which are in good agreement with the measurement data provided by Dufour [15].

a) Methane Reforming Reaction

As shown in chapter 3, the local mole fraction of the relevant chemical species was measured over the course of the flow field. These results are used to validate the CFD simulation. In order to find the right settings for the equations stated in section 4.3.1, Arrhenius curve-fits are used. Doing so, the reaction rate constants of methane have to be determined using the measured data. As described in chapter 2.3.4, the reaction rate states the change of a component's concentration over time.

In order to calculate the change of the methane concentration on the flow field Δc_{CH_4}, its molar flow at the beginning and the end of the flow field and the actual volume flow through the flow field have to be known. The molar flow of methane has already been determined, as described in chapter 3. Using the equation for ideal gases to adjust the measured values from the MFCs of gases entering the system to the operating tempeature of the system, the volume flow through the flow field can be calculated. For this calculation it is assumed that H_2 and O_2 react to H_2O in the steam generator (see figures 20 and 21). This reaction implies a reduction of the volume flow. For further anlysis it is assumed that the thereby calculated volume flow remains constant, which also represents a simplification since various

reactions take place (most prominently methane steam reforming as stated in equation 2.43), subsequently changing the volume of the fuel mixture.

To determine the time it takes the fuel to pass through the flow field Δt_{FF}, the volume flow calculated above and the geometry of the flow field have to be taken into consideration. The geometry of the flow field can be taken directly from the computer aided design (CAD) data of the testbed.

Subsequently the reaction rate is determined using a finite form of equation 2.49:

$$r_{CH_4} = \frac{\Delta c_{CH_4}}{\Delta t_{FF}} = \frac{c_{CH_4,Channel\ 1} - c_{CH_4,Channel\ 5}}{\Delta t_{FF}} \tag{4.12}$$

Based on the thereby known reaction rate the reaction rate constant can be calculated. In order to do so, the reaction order of the focal reaction has to be known. Since reaction orders can not be determined using the available data from the testbed, approaches linking the reaction rate and the reaction rate constant were taken from literature. A compilation of possible equations for this purpose are stated in chapter 2.3, table 3. The partial pressures of the species of interest correlate to their molar fractions according to equation 4.13.

$$p_{Species} = p_{Ambient} \cdot \nu_{Species} \tag{4.13}$$

Since the wet molar fractions at OCV have been determined (see chapter 3) and assuming an ambient pressure of $p = 1013\ mbar$, the corresponding partial pressures of all species can be calculated using equation 4.13. Subsequently, the reaction rate constant of methane can be calculated. In oder to be able to compare different formulations, the exponential approaches 1, 4 and 6 from table 3 were used. The remaining formulations from table 3 were excluded since the recommended temperature ranges of the remaining approaches significantly exceeded the measured temperature range.

As decribed in chapter 3, measurements were performed at the three different temperatures 700 °C, 750 °C and 800 °C. Therefore an Arrhenius plot of the determined reaction rates can be drawn (see chapter 2.3.4). From the Arrhenius plot of the corresponding exponential approaches the activation energy E_a and the pre-exponential factor A are determined (see chapter 2). These values can subsequently be used as input parameters in FIRE®.

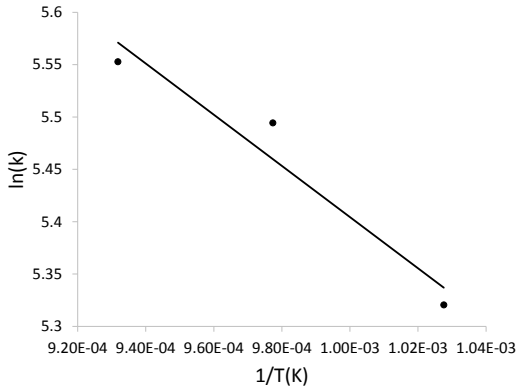

(a)

Approach 1: $r = k \cdot p_{CH_4}^1$

Interpolated Line:
$In(k) = -2443.4 \cdot \frac{1}{T} + 7.8347$

Resulting Parameters:
$E_a = 20314.43\ [\frac{kJ}{kmol}]$
$A = 2526.77$

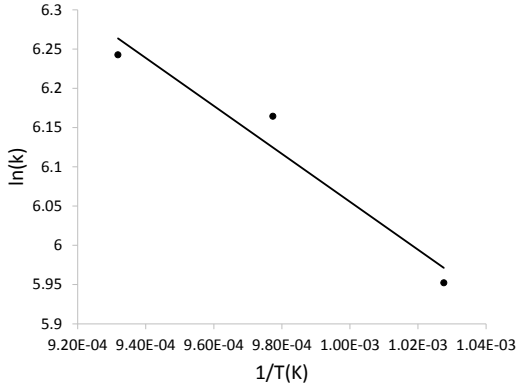

(b)

Approach 2: $r = k \cdot p_{CH_4}^{1.25}$

Interpolated Line:
$In(k) = -3052.6 \cdot \frac{1}{T} + 9.90916$

Resulting Parameters:
$E_a = 25379.31\ [\frac{kJ}{kmol}]$
$A = 8880.38$

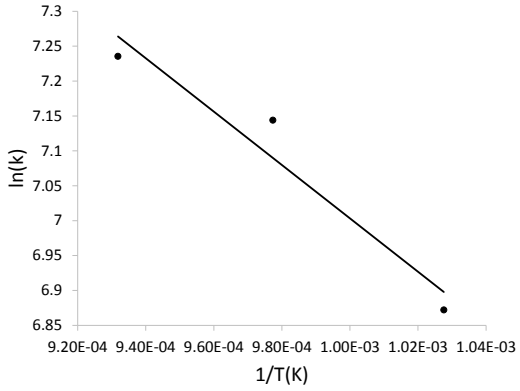

(c)

Approach 3: $r = k \cdot p_{CH_4}^1 \cdot p_{H_2O}^1$

Interpolated Line:
$In(k) = -3822.1 + 10.799$

Resulting Parameters:
$E_a = 31776.93\ [\frac{kJ}{kmol}]$
$A = 48971.80$

Figure 32: Investigation on approaches for the reaction rate.

b) Water-gas-shift Reaction

Similar to the methane reforming reaction FIRE® requires parameters for the Arrhenius equation in order to simulate the water gas-shift reaction. Unfortunately, the measurements did not provide sufficient data to perform curve fits for the water-gas shift reaction. Therefore values from literature had to be used. Table 13 states the applied parameters.

c) Results using found Parameters

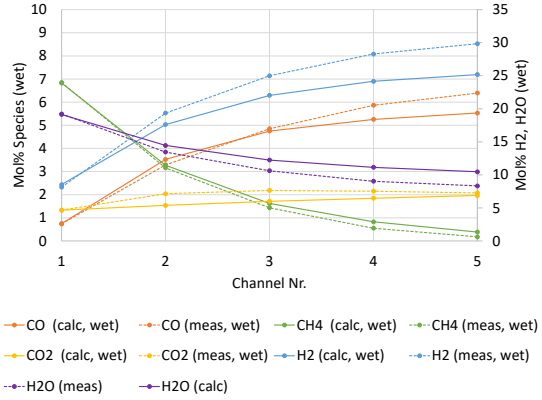

(a)

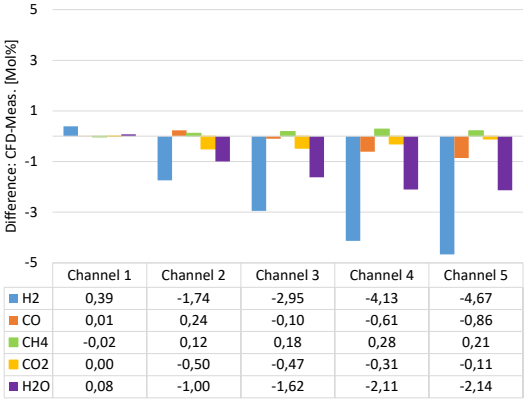

	Channel 1	Channel 2	Channel 3	Channel 4	Channel 5
H2	0,39	-1,74	-2,95	-4,13	-4,67
CO	0,01	0,24	-0,10	-0,61	-0,86
CH4	-0,02	0,12	0,18	0,28	0,21
CO2	0,00	-0,50	-0,47	-0,31	-0,11
H2O	0,08	-1,00	-1,62	-2,11	-2,14

(b)

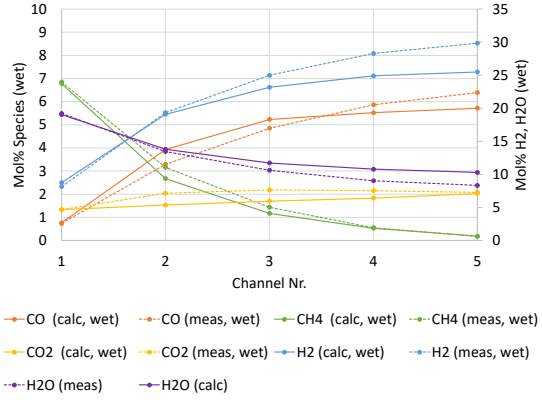

(c)

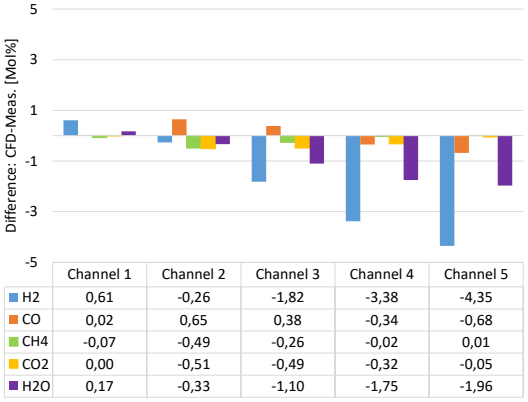

	Channel 1	Channel 2	Channel 3	Channel 4	Channel 5
H2	0,61	-0,26	-1,82	-3,38	-4,35
CO	0,02	0,65	0,38	-0,34	-0,68
CH4	-0,07	-0,49	-0,26	-0,02	0,01
CO2	0,00	-0,51	-0,49	-0,32	-0,05
H2O	0,17	-0,33	-1,10	-1,75	-1,96

(d)

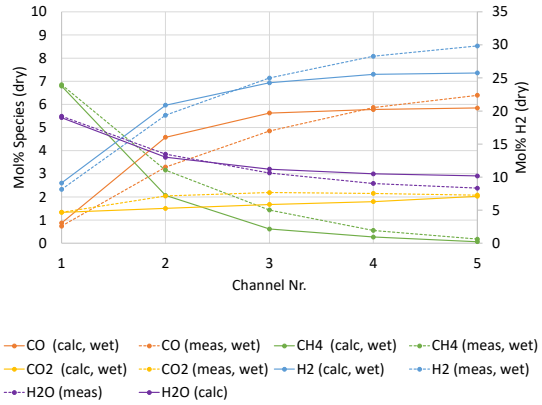

(e)

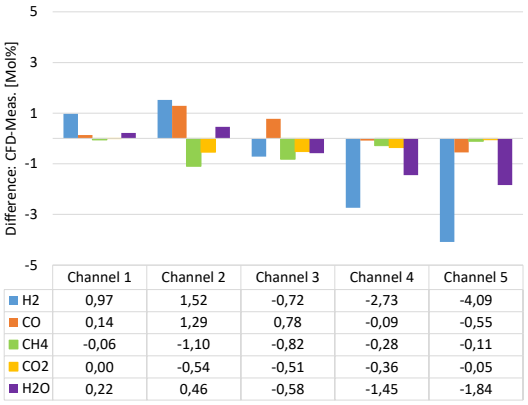

	Channel 1	Channel 2	Channel 3	Channel 4	Channel 5
H2	0,97	1,52	-0,72	-2,73	-4,09
CO	0,14	1,29	0,78	-0,09	-0,55
CH4	-0,06	-1,10	-0,82	-0,28	-0,11
CO2	0,00	-0,54	-0,51	-0,36	-0,05
H2O	0,22	0,46	-0,58	-1,45	-1,84

(f)

Figure 33: Plots of the measured and simulated fuel species at 750 °C and OCV with the found Arrhenius parameters using the approaches stated in figure 32. Approach 1 (a,b), Approach 2 (c,d) and Approach 3 (e,f)

Looking at figue 33 the different reforming behaviours of the tested approaches can be analyzed. All approaches tested show good agreement to measurements. Approach 1 (figure 33 a,b) and approach 2 (figure 33 c,d) show a good fit between measured and simulated mol fractions of methane over the course of the cell. However, the values for water and hydrogen at the end of the flow field (channel 5) show significant deviations to the measured values. Both approach 1 and appoach 2 underestimate the molar fractions of hydrogen and carbon dioxide while they overestimate the molar fraction of water. Approach 3 (figure 33 e,f) exhibits the smallest deviations for the molar fractions of hydrogen, carbon monoxide and water at the end of the cell (channel 5). On the downside, approach 3 displays relatively high deviations regarding the change of species along the cell, compared to the other reforming approaches. As argued in chapter 3, it is assumed that the fuel species at the end of the cell are in equilibrium composition. In order to get results close to the assumed equilibrium compositions, approach 3 is used for further analysis.

Table 12: Settings to simulate the reforming reaction of methane

Parameter	Value	Unit
Equation setting n	1	-
Equation setting m	4	-
Equation setting p	0	-
Pre-exponential factor A	48971.8	$\frac{m^3}{mol \cdot s \cdot K^b}$
Temperature exponent b	0	-
Activation energy	31776.93	$\frac{kJ}{kmol}$
Equilibrium coefficient	Formula (see 2.46)	

Table 13: Settings to simulate the watergas-shift reaction [11]

Parameter	Value	Unit
Pre-exponential factor A'	1.18123	$\frac{m^3}{mol \cdot s \cdot K^b}$
Temperature exponent b	2	-
Activation energy	103191	$\frac{kJ}{kmol}$
Equilibrium coefficient	Formula (see 2.48)	

4.3.3 Implemented Electrochemistry Equations in FIRE®

Simulating the electrochemistry of an SOFC, FIRE® splits the overall reaction into the oxygen reduction reaction at the cathode and the hydrogen oxidation reaction at the anode, as described in chapter 2.2. These electrochemical half cell reactions are described using the Butler-Volmer-equation explained in chapter 2.2 [10]:

$$i = i_0 \left[exp\left(\frac{n_e k_a F}{RT} \eta_{act} \right) - exp\left(-\frac{n_e k_c F}{RT} \eta_{act} \right) \right] \tag{4.14}$$

The variables in 4.14 are the charge transfer number n_e, the activation overpotential η_{act} and the exchange current density i_0 [10].

$$n_e = 2 \tag{4.15}$$

$$\eta_{act} = \phi_{ele} - \phi_{ion} - \phi_{oc} \tag{4.16}$$

$$i_0 = i_{0,ref} \left(\frac{p_{O_2}}{p_{ref}} \right)^{b_{O_2}} \left(\frac{p_{H_2}}{p_{ref}} \right)^{b_{H_2}} \left(\frac{p_{H_2O}}{p_{ref}} \right)^{b_{H_2O}} \cdot \quad exp\left[-\frac{E_{act}, i_0}{R} \left(\frac{1}{T} - \frac{1}{T_{ref,i_0}} \right) \right] \tag{4.17}$$

In equation 4.17 the hydrogen exponent b_{H_2} as well as the water exponent b_{H_2O} are zero at the positive electrode, whereas the oxygen exponent b_{O_2} is zero at the negative electrode. ϕ_{ele} and ϕ_{ion} in equation 4.16 are the electronic, respectively the ionic potential at the triple phase boundary. The open circuit potential ϕ_{oc} is calculated using the Nernst equation, as stated in equations 4.18 and 4.19. Their difference is the OCV in the TPB, as stated in equation 4.20 [10]:

$$\phi_{oc,pos} = E_0 + \frac{RT_{pos}}{4F} ln\left(\frac{p_{O_2,pos}}{p_{ref}} \right) \tag{4.18}$$

$$\phi_{oc,neg} = E_0 + \frac{RT_{neg}}{4F} ln\left(\frac{p_{H_2O,neg}}{p_{ref}} \right) \tag{4.19}$$

$$V_{oc,r} = \phi_{oc,pos} - \phi_{oc,neg} \tag{4.20}$$

The standard open circuit potential E_0 depends on the given temperature. It can be approximated by following approach [10]:

$$E_0 = 1.273 - 2.75 \cdot 10^{-4} \cdot T \tag{4.21}$$

According to [10], the parameters $i_{0,ref}$, k_c, k_a, b_{H_2}, b_{H_2O} and b_{O_2} can be used as fitting parameters in order to fit the simulation result to a reference experiment.

4.3.4 Fitting of the IV-Curves

Since the measured IV-curves for each cathode show significant deviations to one another [15], a fitting criterion suitable for the cell as a whole had to be found. Therefore, the mean values of the four cathodes on the segmented single cell were taken for comparison of simulated and measured data. Main goal was to fit the IV-curves in the area of ohmic losses. As shown by [15], this area is dominant in the given IV data series. Further, the measurement of the IV-curve at 800 °C and current densities below $i = 168\ \frac{mA}{cm^2}$ has been performed operating with an instationary fuel composition. Therefore, the gathered data below said current density is neglected and the available data is limited to the linear ohmic region.

Besides the limitation in underlying data, the decision to use only the linear ohmic region to fit the simulated and measured IV-curves also holds practical advantages. Doing so the required amount of calculations necessary to determine the viability of a set of parameters is reduced. In the given cases fitting calculations were performed at a current density of $i = 56\ \frac{mA}{cm^2}$ and $i = 280\ \frac{mA}{cm^2}$ for the test series at 700 °C as well as $i = 168\ \frac{mA}{cm^2}$ and $i = 448\ \frac{mA}{cm^2}$ for the test series at 750 °C and 800 °C. In order to fit the IV-Curves obtained via CFD simulation to the measured IV-curves, the parameters explained in section 4.3.3 were adapted iteratively. If a set of parameters fitting for two points of the linear ohmic region was identified, an additional calculation in between the investigated current densities was performed. This was done in order to ensure the viability of the result. These checks were performed at $i = 168\ \frac{mA}{cm^2}$ for 700 °C as well as at $i = 280\ \frac{mA}{cm^2}$ for 750 °C and 800 °C. Only if all three resulting mean voltages lie on the same line and the line itself is within a reasonably small distance to the measured mean IV-curve, the resulting set of parameters is considered a fit. Therefore, the transfer coefficient (TC) of the anode as well as the cathode and the exchange current density (ECD) were varied. By doing so, the parameters stated in table 14 were obtained.

Table 14: Electrochemistry settings used

	Unit	700 °C		750 °C		800 °C	
		Positive (Cathode)	Negative (Anode)	Positive (Cathode)	Negative (Anode)	Positive (Cathode)	Negative (Anode)
TC cat.	-	0.185	0.5	0.24	0.5	0.08	0.5
TC ano.	-	0.5	0.185	0.5	0.24	0.5	0.08
ECD	$\frac{A}{m^2}$	12000	39500	12000	75000	12000	325000
Ox. Exp.	-	0.25	-	0.25	-	0.25	-
Hydr. Exp.	-	-	1	-	1	-	1
Water Exp.	-	-	1	-	1	-	1
Reference-temp.	°C	700	700	750	750	800	800
Activation -energy	$\frac{J}{mol}$	120000	120000	120000	120000	120000	120000

Figures 34, 35 and 36 show the resulting IV-curves using the mentioned parameters and give a comparison to the respective measurements. Using the regression algorithm implemented in Microsoft Excel, a linear equation for the measured and the simulated results is obtained. It can be seen that for all three considered temperature series the mean values of the simulated IV-curves are fitted to the mean values of the measured IV-curves within reasonable accuracy. Further it can be observed that the measured IV-curves for 700 °C and 800 °C show a significant spread while the measured IV-curves at 750 °C are almost congruent. A likely explanation for this spread is the change of fuel composition along the cell as well as the electrochemical influence of the first row of cathodes. Therefore, the second row of cathodes is exposed to a different fuel composition as the first row. A further possible explanation for the spread of IV-curves are inaccuracies in the performed measurements. This could also explain the measured deviations between the cathode voltages to one another. The IV-curves obtained via CFD simulation also show this behaviour. The spread between the simulated IV-curves, however, is less pronounced than the spread between the measured IV-curves.

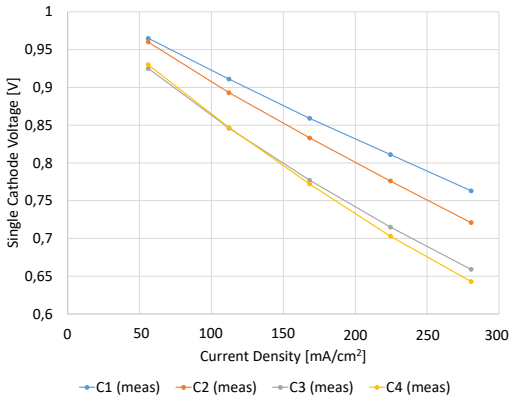

(a)

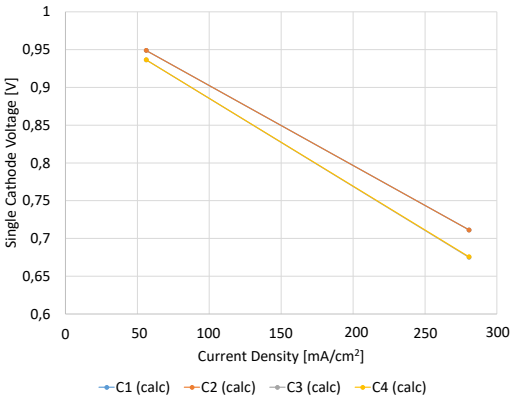

(b)

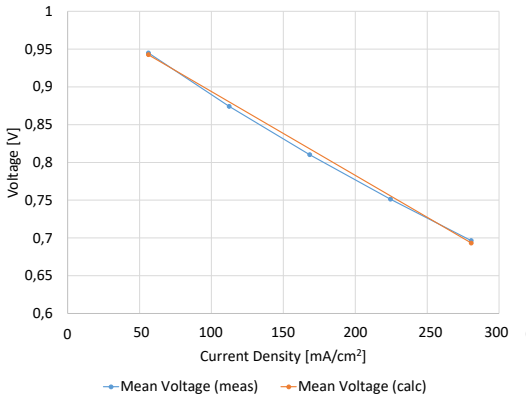

(c)

Interpolated equations

Mean values measurement:
$V = -1.105exp(-6) \cdot i + 1.001$

Mean values from CFD:
$V = -1.111exp(-6) \cdot i + 1.005$

Figure 34: Fitting of the CFD IV-curves to measured data (Methane, 700°C)
(a) Measured IV-curves for cathode 1 to 4
(b) CFD results for cathode 1 to 4
(c) Comparison of the measured and simulated mean values of cathode 1 to 4

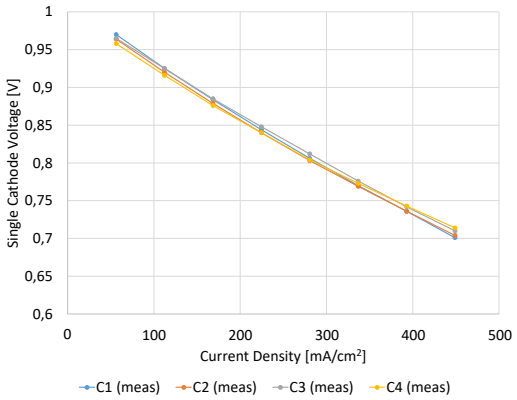

(a)

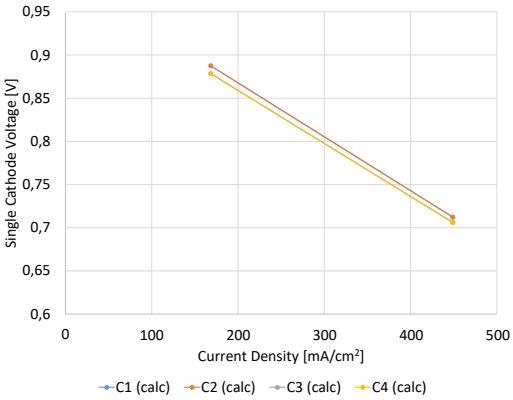

(b)

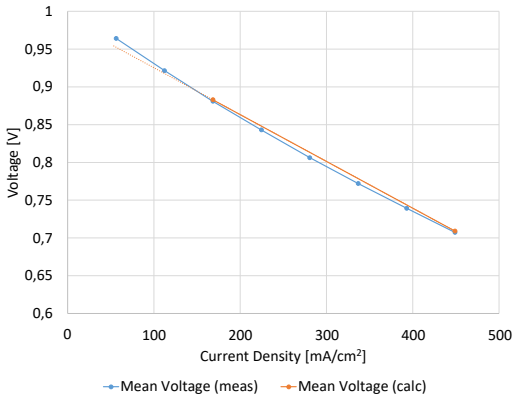

(c)

Interpolated equations

Mean values measurement:
$V = -6.521exp(-7) \cdot i + 0.99390$

Mean values from CFD:
$V = -6.197exp(-7) \cdot i + 0.9873$

Figure 35: Fitting of the CFD IV-curves to measured data (methane, 750°C)
(a) Measured IV-curves for cathode 1 to 4
(b) CFD results for cathode 1 to 4
(c) Comparison of the measured and simulated mean values of cathode 1 to 4

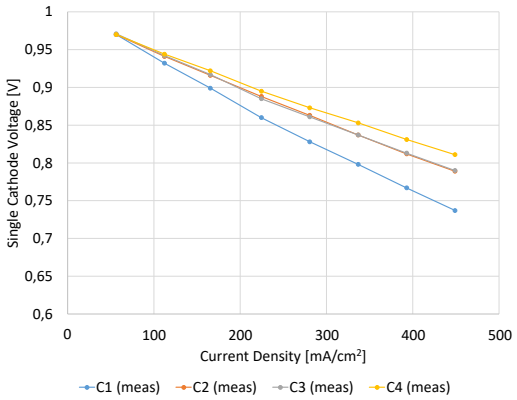

(a)

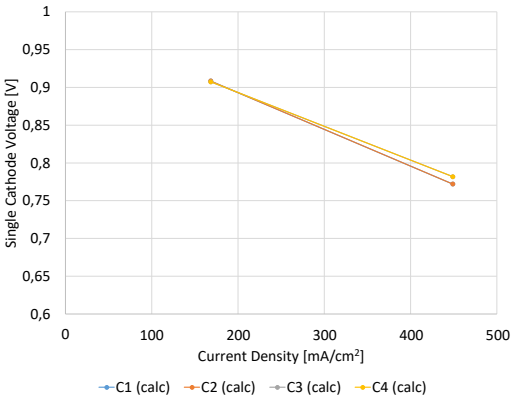

(b)

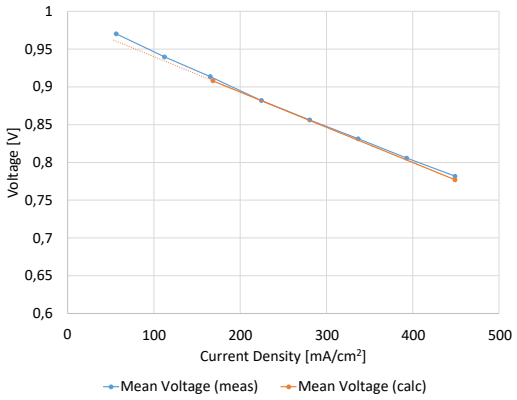

(c)

Interpolated equations

Mean values measurement:
$V = -4.789exp(-7) \cdot i + 0.993$

Mean values from CFD:
$V = -4.670exp(-7) \cdot i + 0.986$

Figure 36: Fitting of the CFD IV-curves to measured data (methane, 800°C)
(a) Measured IV-curves for cathode 1 to 4
(b) CFD results for cathode 1 to 4
(c) Comparison of the measured and simulated mean values of cathode 1 to 4

5 Comparison and Discussion of Results

The aim of this chapter is to discuss the results of the CFD simulation. For the simulation the parameters regarding fuel inlet composition, chemical kinetics and electrochemistry found in chapter 4 are used. The validity of the findings is checked using criteria stated by Wang et. al. [60]. Therefore, the simulated gas compositions and temperature profiles are compared to the measured data at different conditions of operation. Table 15 illustrates the available measured data points and the correlating performed CFD simulations.

Table 15: Overview of measured data points and respective simulation results

	700 °C		750 °C		800 °C	
Case	Measured	Simulated	Measured	Simulated	Measured	Simulated
0 $\frac{mA}{cm^2}$	✓	✓	✓	✓	(✓)	✓
56 $\frac{mA}{cm^2}$	✓	·	✓	·	✓	·
112 $\frac{mA}{cm^2}$	✓	·	✓	·	✓	·
168 $\frac{mA}{cm^2}$	✓	✓	✓	✓	✓	✓
224 $\frac{mA}{cm^2}$	✓	·	·	·	·	·
280 $\frac{mA}{cm^2}$	·	·	✓	·	✓	·
393 $\frac{mA}{cm^2}$	·	·	✓	·	✓	·
449 $\frac{mA}{cm^2}$	·	·	✓	✓	✓	✓
505 $\frac{mA}{cm^2}$	·	·	·	·	✓	·

5.1 Comparison of dry Gas Composition from CFD and dry Measurements

In order to receive comparable results, the CFD data for the fuel composition was taken at the same positions as the measurement holes in the physical testbed are located in. The position of the measurement planes are stated in the appendix. In order to be able to compare measurements of gas species along the cell to simulation data, dry results have to be used. This is due to the fact that with the used measuring equipment the mole fraction of water could not be determined. Since in operation points other than OCV oxygen ions are transported from cathode to anode, a simple balance of atoms is not possible (see chapter 3).

Because of the occuring steam reforming reactions (see section 2.3.3) and because in the presence of hydrogen and oxygen reactions producing water can not be ruled out, it is safe to assume that the molar fraction of water is not constant. However, since the fraction of water is known for every point in the CFD calculation, the wet CFD results can be adjusted to dry results for every measuring point. The underlying data is stated the in the appendix.

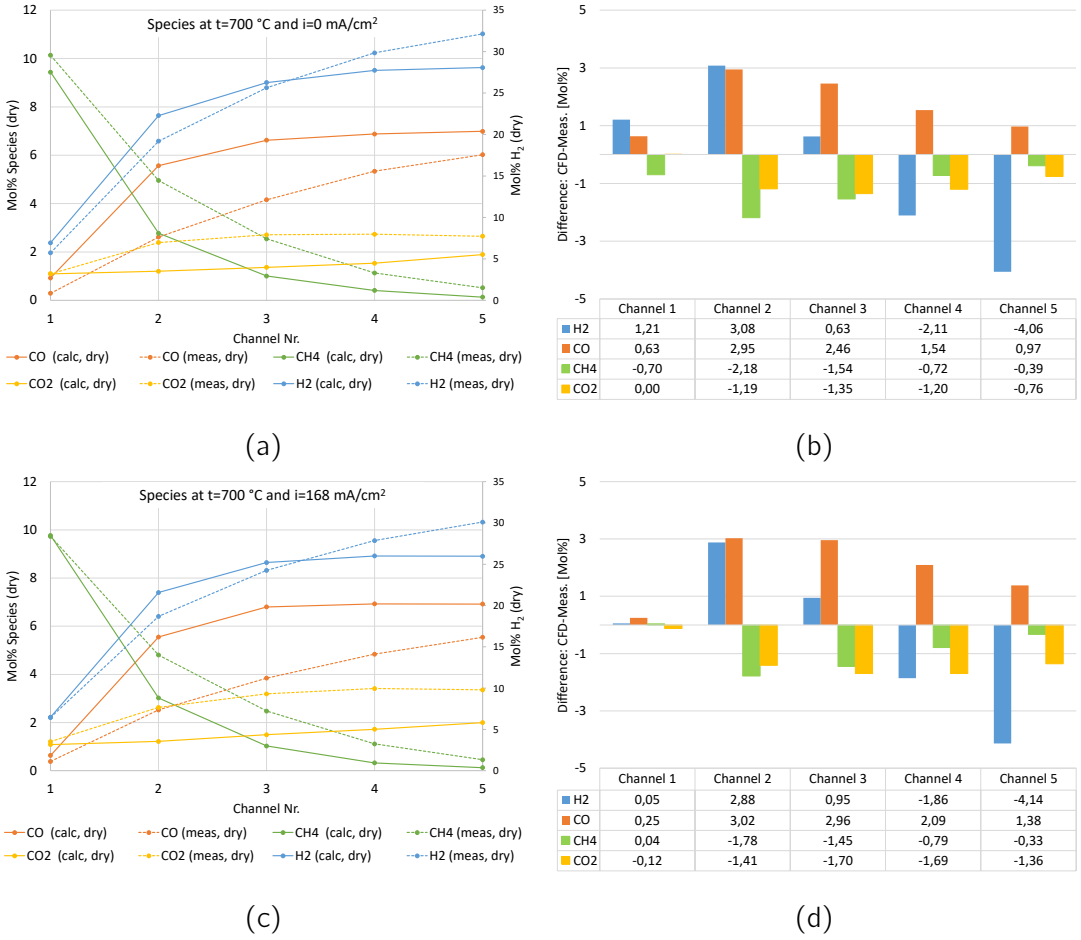

Figure 37: Plots of the simulated fuel species at 700 °C
(a,c) Comparison of the simulated (dry) and measured (dry) species along the cell
(b,d) Difference between simulation and measurement

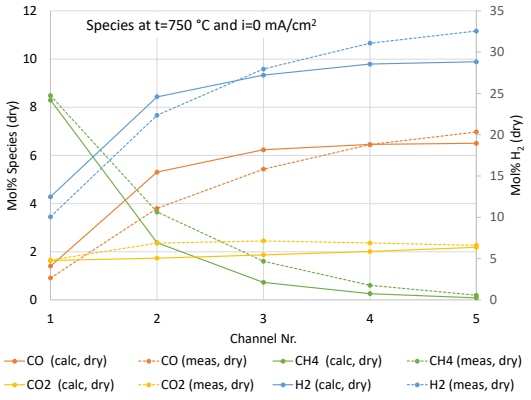

(a)

	Channel 1	Channel 2	Channel 3	Channel 4	Channel 5
H2	2,42	2,23	-0,74	-2,53	-3,72
CO	0,49	1,51	0,80	0,01	-0,47
CH4	-0,19	-1,28	-0,87	-0,34	-0,11
CO2	-0,02	-0,62	-0,58	-0,36	-0,08

(b)

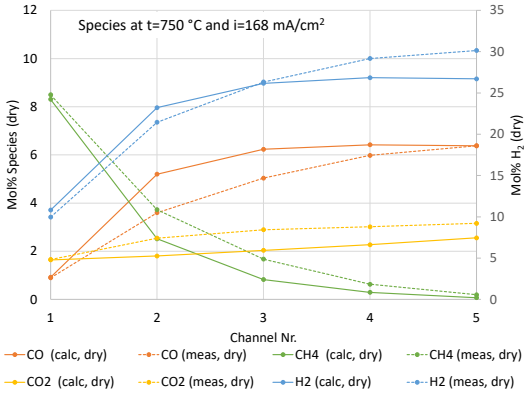

(c)

	Channel 1	Channel 2	Channel 3	Channel 4	Channel 5
H2	0,86	1,78	-0,16	-2,33	-3,43
CO	0,02	1,60	1,19	0,44	0,00
CH4	-0,19	-1,21	-0,85	-0,34	-0,12
CO2	-0,02	-0,74	-0,86	-0,74	-0,60

(d)

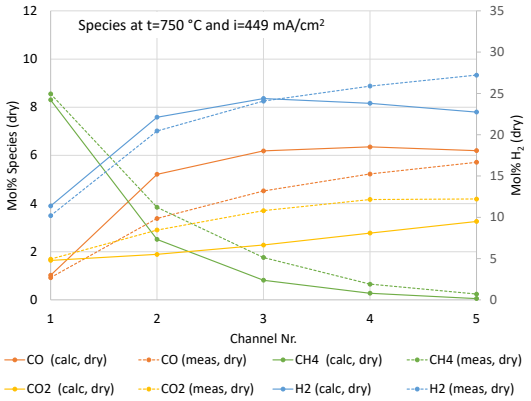

(e)

	Channel 1	Channel 2	Channel 3	Channel 4	Channel 5
H2	1,18	1,66	0,30	-2,08	-4,47
CO	0,10	1,83	1,66	1,13	0,48
CH4	-0,25	-1,33	-0,94	-0,38	-0,19
CO2	-0,05	-1,01	-1,43	-1,39	-0,93

(f)

Figure 38: Plots of the simulated fuel species at 750 °C
(a,c,e) Comparison of the simulated (dry) and measured (dry) species along the cell
(b,d,f) Difference between simulation and measurement

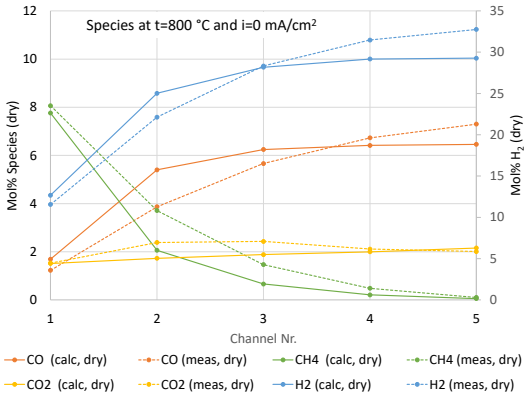

(a)

	Channel 1	Channel 2	Channel 3	Channel 4	Channel 5
H2	1,12	2,89	-0,15	-2,30	-3,48
CO	0,46	1,53	0,58	-0,31	-0,84
CH4	-0,30	-1,65	-0,81	-0,27	-0,05
CO2	-0,01	-0,66	-0,55	-0,11	0,14

(b)

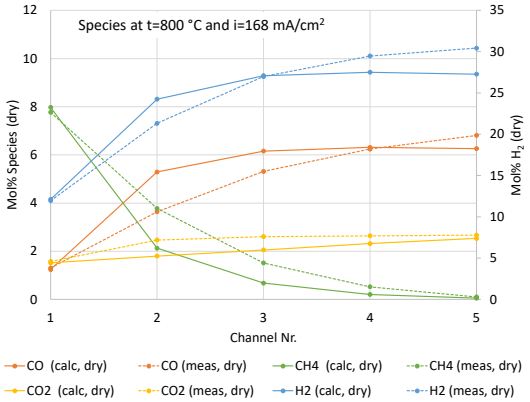

(c)

	Channel 1	Channel 2	Channel 3	Channel 4	Channel 5
H2	0,16	2,92	0,11	-1,97	-3,16
CO	-0,06	1,65	0,84	0,07	-0,55
CH4	0,20	-1,65	-0,83	-0,32	-0,05
CO2	-0,06	-0,66	-0,55	-0,32	-0,14

(d)

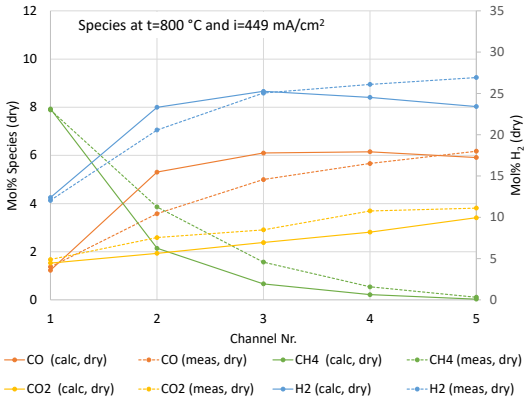

(e)

	Channel 1	Channel 2	Channel 3	Channel 4	Channel 5
H2	0,35	2,75	0,21	-1,57	-3,51
CO	-0,14	1,73	1,10	0,49	-0,26
CH4	0,04	-1,72	-0,90	-0,33	-0,08
CO2	-0,15	-0,65	-0,53	-0,88	-0,40

(f)

Figure 39: Plots of the simulated fuel species at 800 °C
(a,c,e) Comparison of the simulated (dry) and measured (dry) species along the cell
(b,d,f) Difference between simulation and measurement

Figures 37, 38 and 39 compare the simulated dry compositions to the dry measurements along the cell for all investigated temperatures and current densities (see table 15).

As discussed in section 4.3.2, in the CFD simulation the conversion of methane to hydrogen via the steam reforming reaction takes place faster than the measurements indicate. Further, also coupled with the steam reforming reaction, the molar fractions of hydrogen and carbon monoxide in the CFD simulation increase faster than stated by the measured data. The simulation results for carbon monoxide and hydrogen at the end of the flow field differ from the measured composition. A possible reason for this behaviour are inaccurate parameters for the steam reforming reaction. As stated in 4.3.2, the data obtained from the testbed allowed only to fit the steam reforming reaction to measurements. Therefore, literature values for the kinetics of the water-gas shift reaction had to be used.

As expected, the molar fraction of hydrogen decreases with increasing current density in the CFD simulation, since it is consumed as fuel. Contrary to the behaviour of the CFD simulation, the measurements show only a slight decrease of hydrogen along the cell. The molar fraction of carbon dioxide shows the largest difference between measurements and calculations at 700 °C. At 750 °C and 800 °C the results for carbon dioxide show good accordance. Nonetheless, the simulation results are lower than the measured data for any case. The difference of the investigated fuel species between simulation and measurement however is less than 5 mol% for all considered operation points.

Further it can be observed that the set of parameters used to simulate the water-gas-shift and the steam reforming reaction shows the best accordance to measurements at 800 °C. This is supported by the fact that the underlying approach for performing the Arrhenius-fit, which is needed to determine steam reforming parameters, was recommended for higher temperatures (see [34]).

5.2 Comparison of Simulated and Measured Temperatures

For every investigated operating point stated in table 15, a 3D plot as well as a 2D plot of the simulated and measured temperature distribution as well as the respective temperature difference between simulation and measurement is stated. Temperatures are compared in the measurement plane 15 mm above the base of the anode flow field. This reflects the positioning of thermocouples on the test rig (see chapter 3). The underlying data for measured and simulated temperatures is stated in the appendix.

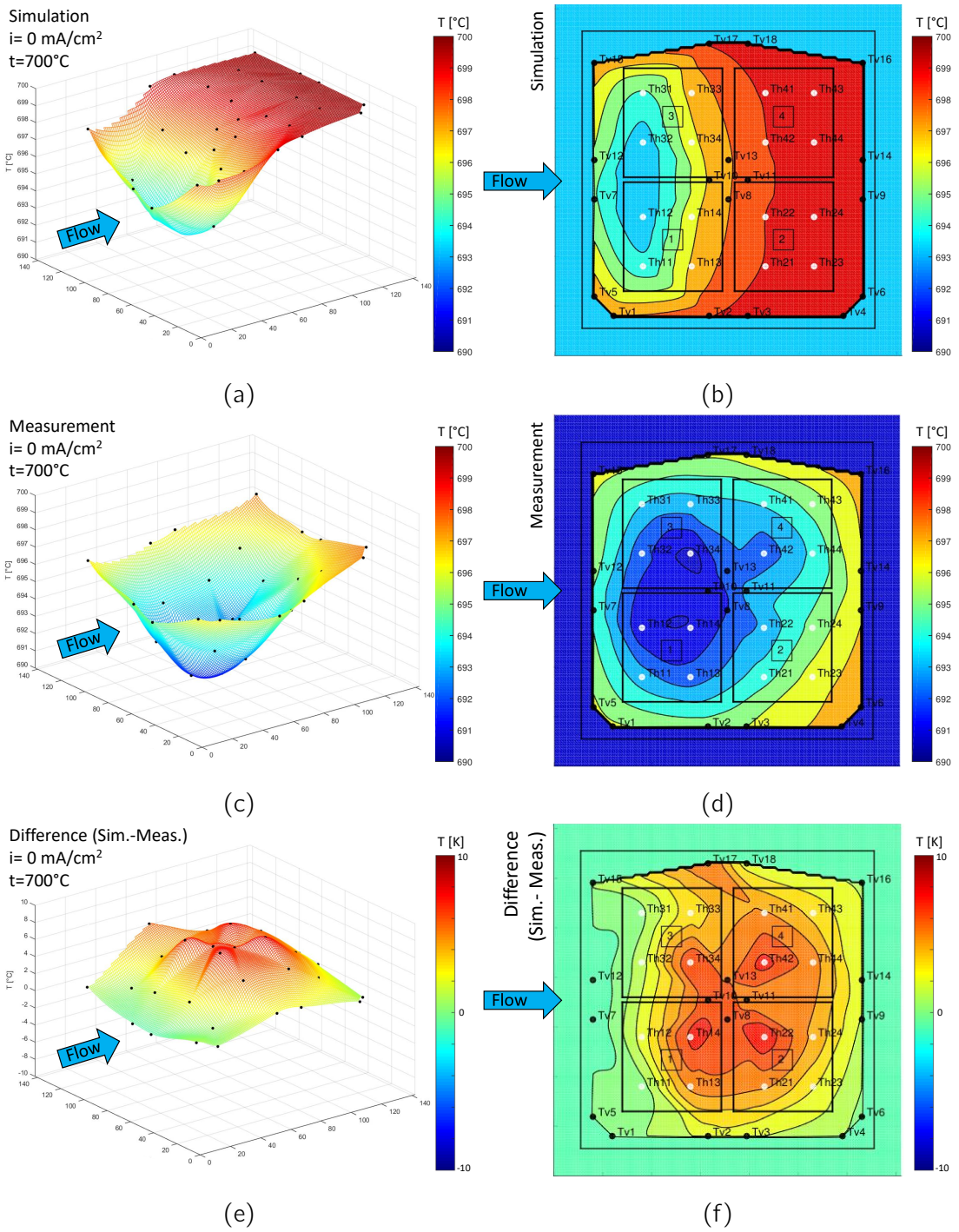

Figure 40: Plots of the measured (a,b) and simulated (c,d) temperature distributions as well as the difference between measurement and simulation (e,f) at 700 °C and $i = 0\ \frac{mA}{cm^2}$

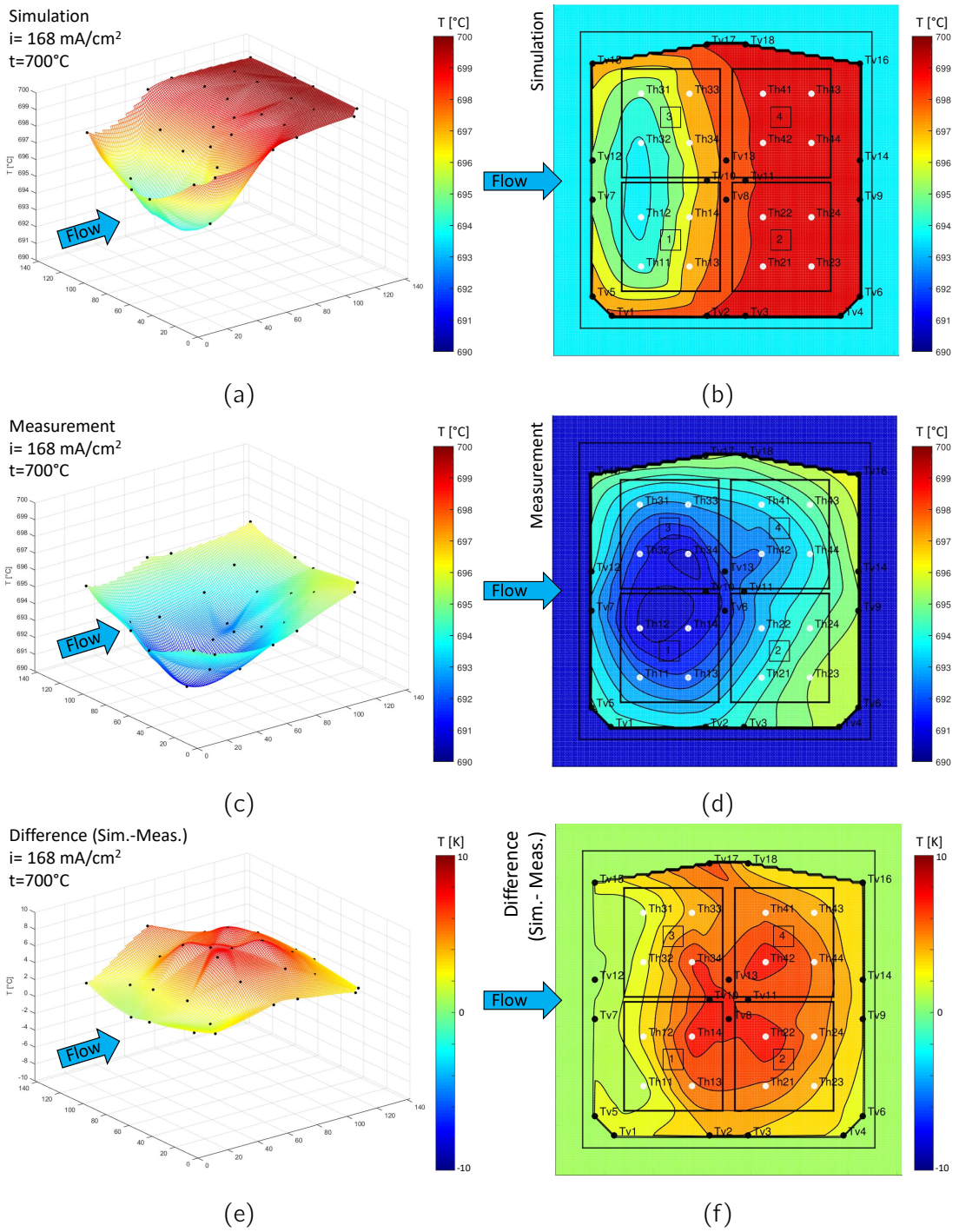

Figure 41: Plots of the measured (a,b) and simulated (c,d) temperature distributions as well as the difference between measurement and simulation (e,f) at 700 °C and $i = 168\ \frac{mA}{cm^2}$

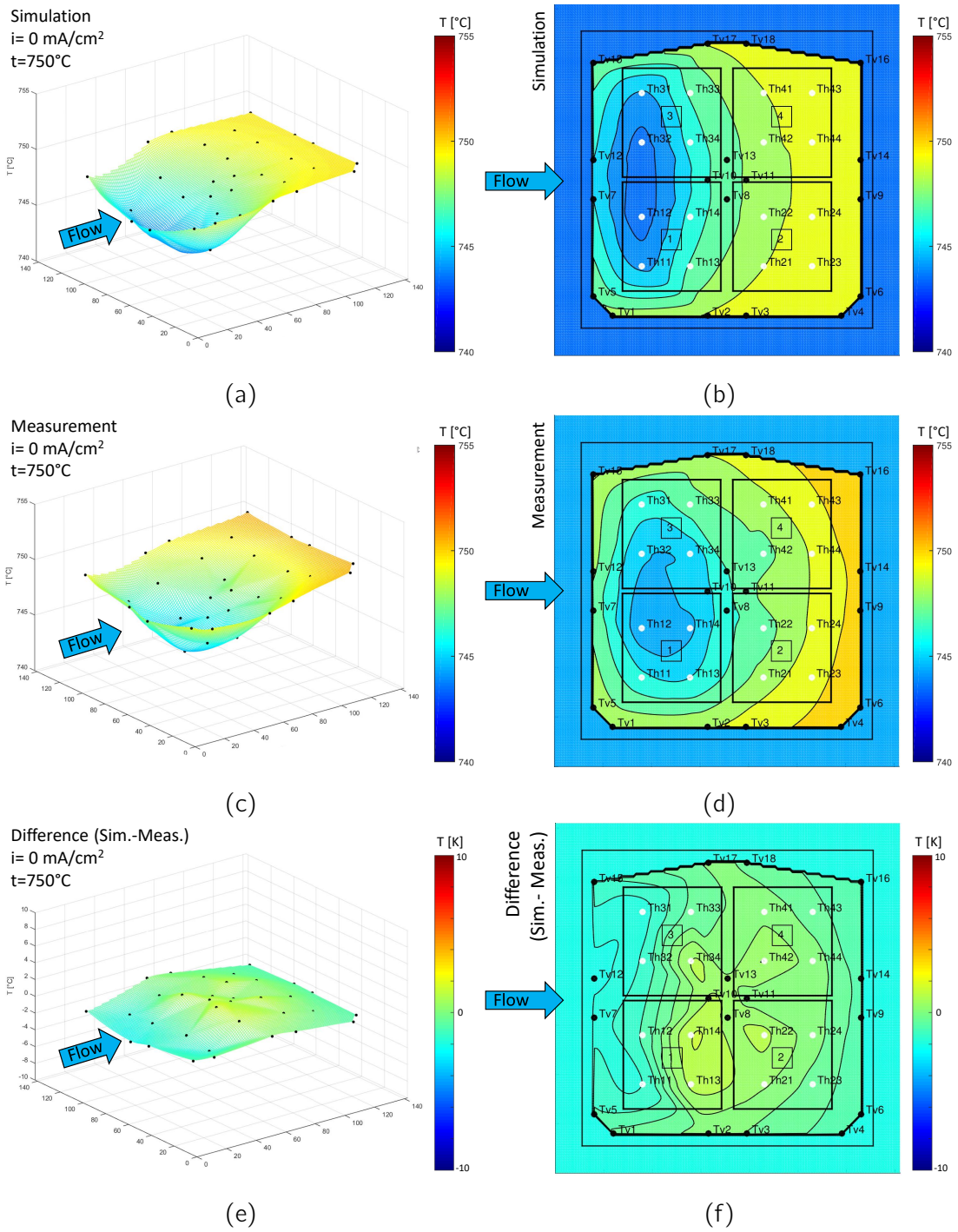

Figure 42: Plots of the measured (a,b) and simulated (c,d) temperature distributions as well as the difference between measurement and simulation (e,f) at 750 °C and $i = 0\ \frac{mA}{cm^2}$

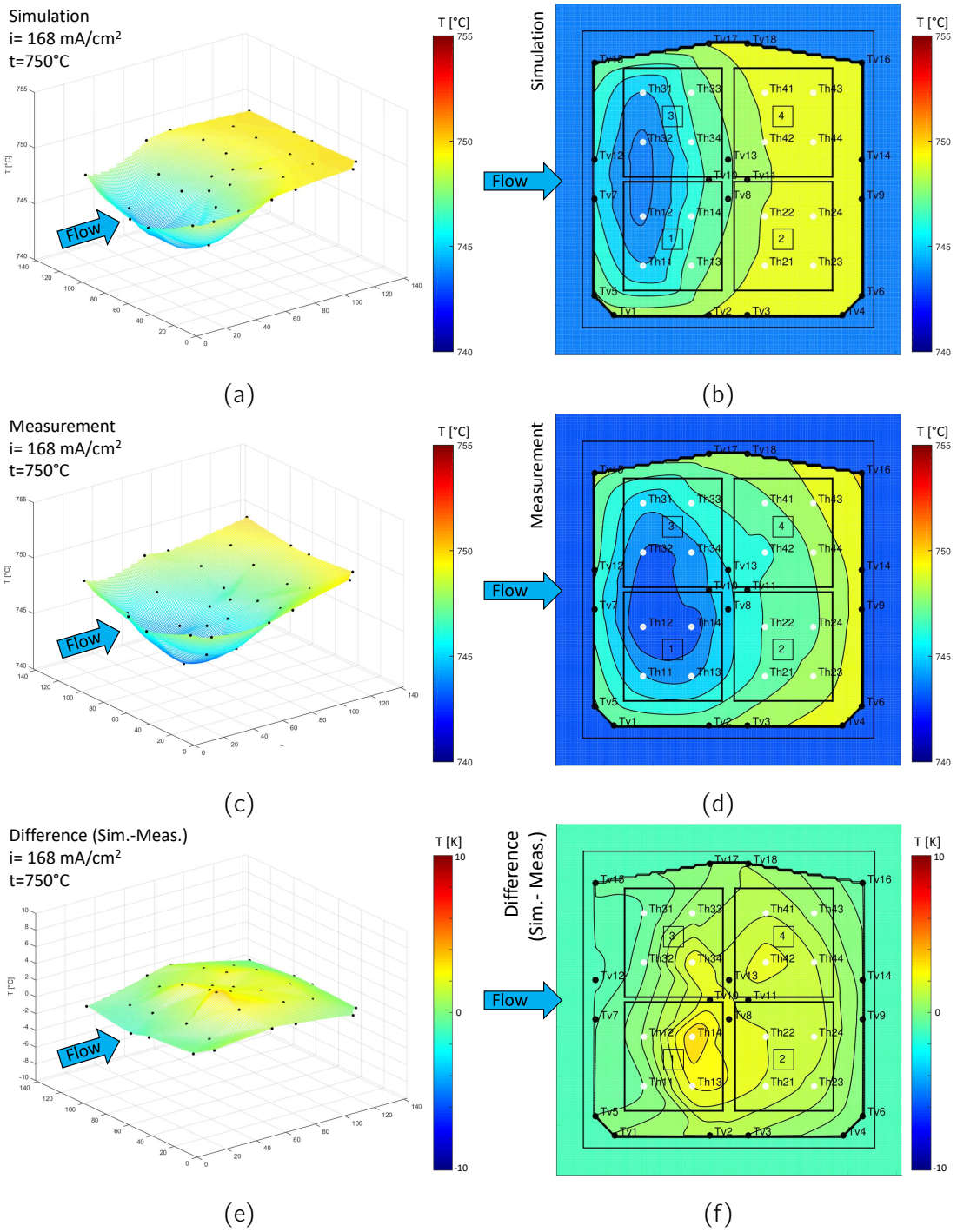

Figure 43: Plots of the measured (a,b) and simulated (c,d) temperature distributions as well as the difference between measurement and simulation (e,f) at 750 °C and $i = 168\ \frac{mA}{cm^2}$

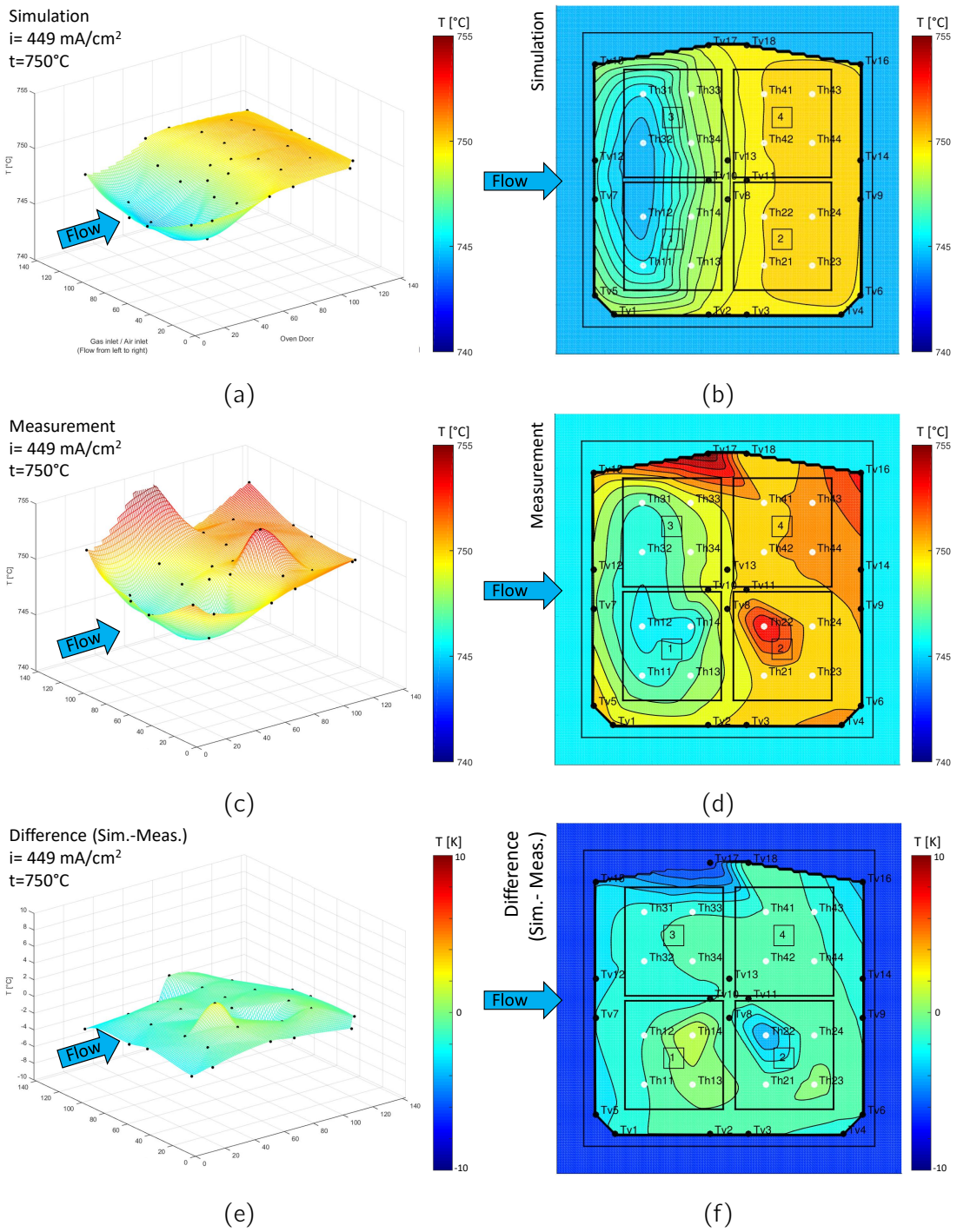

Figure 44: Plots of the measured (a,b) and simulated (c,d) temperature distributions as well as the difference between measurement and simulation (e,f) at 750 °C and $i = 449\ \frac{mA}{cm^2}$

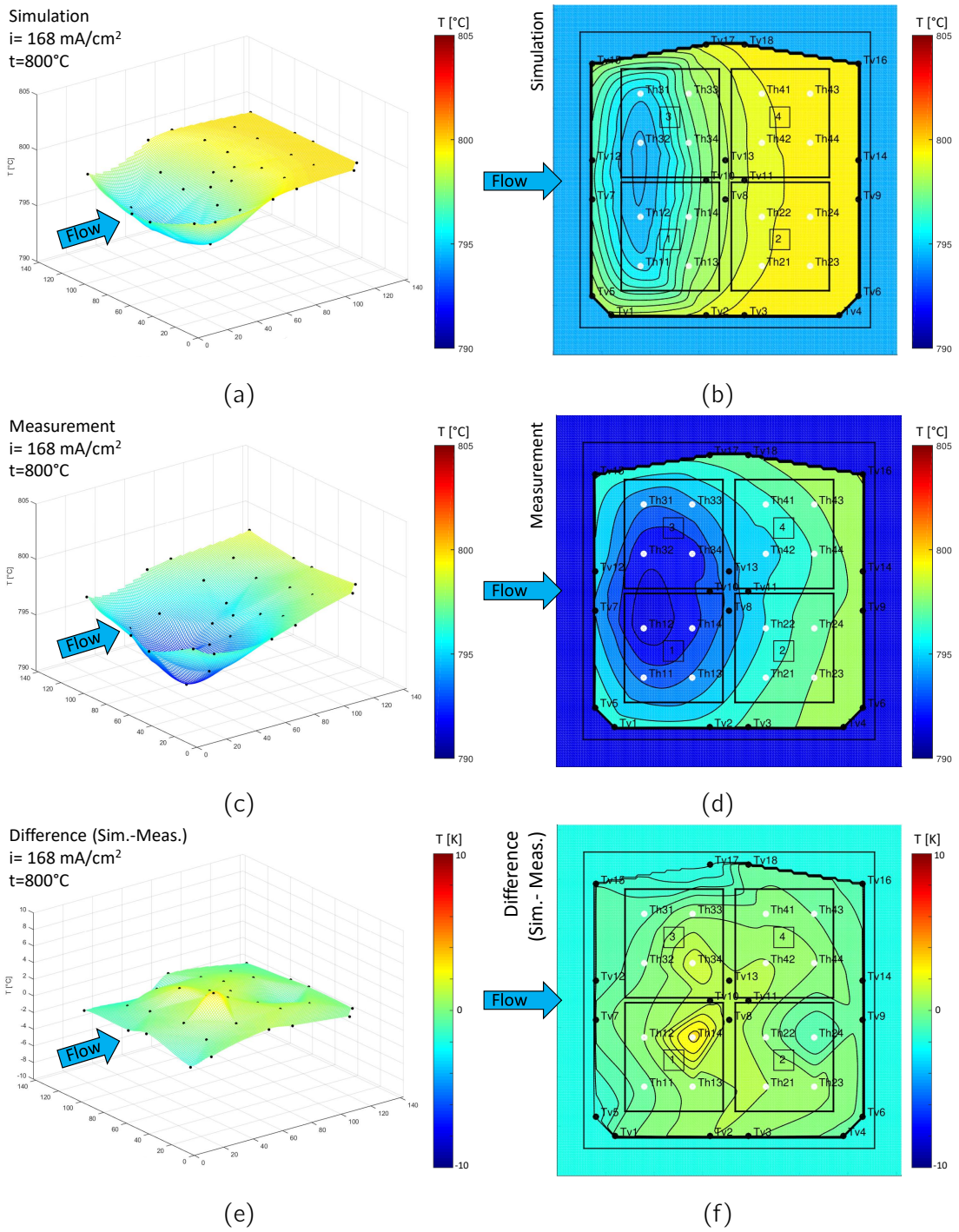

Figure 45: Plots of the measured (a,b) and simulated (c,d) temperature distributions as well as the difference between measurement and simulation (e,f) at 800 °C and $i = 168\ \frac{mA}{cm^2}$

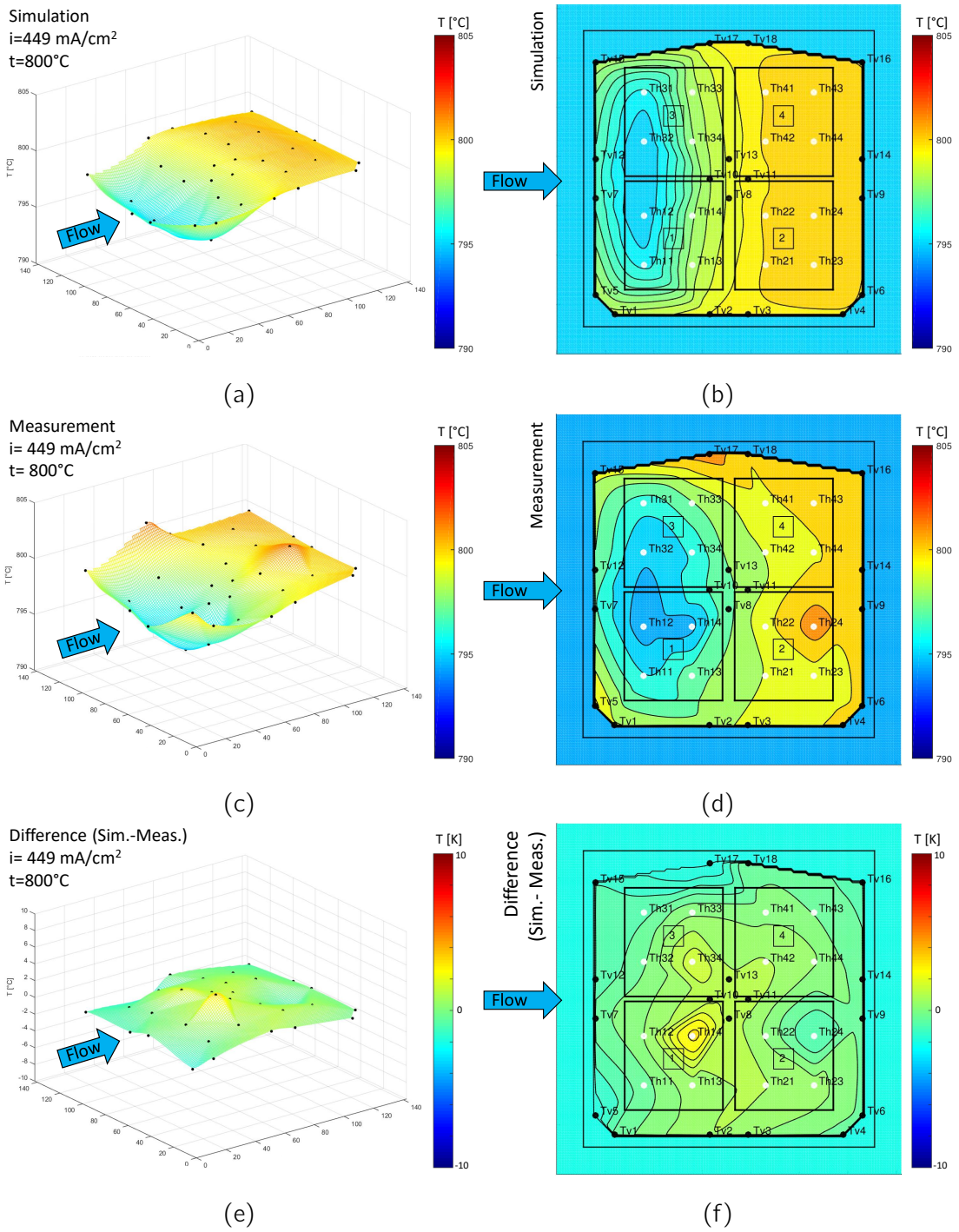

Figure 46: Plots of the measured (a,b) and simulated (c,d) temperature distributions as well as the difference between measurement and simulation (e,f) at 800 °C and $i = 449\ \frac{mA}{cm^2}$

The figures 40 and 41 show the results for an oven temperature of 700 °C while figures 42, 43, 44 as well as 45, 46 state the temperature profiles for an oven temperature of 750 °C and 800 °C respectively. Again, in addition to the temperature of the setup, the drawn current has been varied.

The investigated operating conditions are stated in table 15. In order not to operate at voltages below 0.7 V, measurements at 700 °C could not be performed at higher current densities than $i = 224\ \frac{mA}{cm^2}$. A further limitation regarding measurements is given through non-steady operation conditions at 800 °C and current densities below $i = 168\ \frac{mA}{cm^2}$. Therefore, the simulation data for the temperature can not be validated for this specific operating point.

In order to account for systematic measurement failures, the temperature measurements were corrected at an operation point where no current was drawn and using a non reforming gas (see chapter 3.3). However, a number of the used thermocouples show unreasonable temperature deviations at higher current densities ($i = 449\ \frac{mA}{cm^2}$). The affected measuring positions are T_h22, T_v17, T_h14 and T_h22. The specific reasons for these deviations could not be determined. However, possible explanations are a degradation of the thermocouples or influences of the drawn current on the testing equipment, as indicated by Dufour [15].

Another inconsistency regarding measurements can be observed when comparing the measured temperature profiles at 700 °C and $i = 0\ \frac{mA}{cm^2}$ to 700 °C and $i = 168\ \frac{mA}{cm^2}$ (see figures 40 and 41, subplots (c,d)), respectively 750 °C $i = 0\ \frac{mA}{cm^2}$ and 750 °C $i = 168\ \frac{mA}{cm^2}$ (see figures 42 and 43, subplots (c,d)). Thereby measurements indicate that at a current density of $i = 168\ \frac{mA}{cm^2}$ temperatures are slightly lower than at OCV. Theory as well as simulations clearly indicate that an increase in current density from $i = 0\ \frac{mA}{cm^2}$ to $i = 168\ \frac{mA}{cm^2}$ results in an increased temperature. Simulations show that the mentioned increase is rather small (< 1 K) though. Since the thermocouples used have a greater measuring tolerance than said temperature deviation, inaccurate measurements are a likely explanation for the results described.

As the steam reforming reactions of methane are overall endothermic (see section 2.3.3), a cooling effect in the areas where reforming takes place is expected. Simulation results as well as measurements clearly indicate that the effect is dominant where methane-rich gas enters the catalytic environment in the region of the flow field. As stated in section 5.1, by using the chosen approach for the Arrhenius equation, the simulated reforming reactions take place faster than measurements indicate. This behaviour is also reflected in the resulting temperature profiles. Considering the simulation results for the temperature distributions (see figures 40 - 46, subplots a and b), the cooling effect is dominant in the first half of the flow field. Temperature measurements (see figures 40 - 46, subplots c and d) indicate a more even distribution of the cooling effect through steam reforming.

Another effect already indicated by the distribution of dry species along the flow field (see section 5.1) is the dependence of the results on the temperature of the test rig itself.

Table 16: Temperature differences between simulations and measurements

Set oven temp.	[°C]	700		750			800	
Drawn current density	$[\frac{mA}{cm^2}]$	0.0	168	449	168	449	168	449
Temp. spread (meas.)	[K]	6.9	5.6	6.2	6.9	10.1	5.6	7.8
Temp. spread (sim.)	[K]	6.4	6.1	6.1	5.9	5.7	5.6	5.5
ΔT_{mean}	[K]	3.4	4.4	-0.2	0.9	-1.3	2.4	0.2
ΔT_{max}	[K]	6.4	6.8	1.5	3.3	1.9	4.5	3.3
ΔT_{min}	[K]	0.4	1.8	-2.2	-1.1	-6.5	0.7	-1.9
$\Delta T_{abs,mean}$	[K]	3.4	4.4	0.8	1.1	1.5	2.4	0.8
$\Delta T_{abs,max}$	[K]	6.4	6.8	2.2	3.3	6.5	4.5	3.3
$\Delta T_{abs,min}$	[K]	0.4	1.8	0.0	0.0	0.2	0.7	0.0

Comparing the temperature results of simulations and measurements, it can be seen that for higher test rig temperatures a better fit is achieved. This, again, is in accordance with the results from section 5.1, where it was shown that measured and simulated fuel species concentrations show a better fit at higher temperatures of the test rig. Further, it shows that the accuracy of the simulated reforming reactions directly affects the accuracy of the simulated temperature distributions.

Looking at the differences between measurements and simulations (see figures 40 - 46, subplots e and f), it can be seen that the simulated temperature profiles are in good agreement with measurements. Table 16 states detailed results regarding the measured temperature spread as well as the deviations between measurement and simulation. From table 16 it can be seen that in the simulations the temperature spread decreases with increasing current density. This is plausible since the heating effect due to cell operation overlays the cooling effect through steam reforming. Unfortunately, measurements do not show the mentioned behaviour. Likely reason are measurement inaccuracies. Neglecting the unaccounted temperature deviations at 750 °C respectively 800 °C and $i = 448\ \frac{mA}{cm^2}$, the least accurate results overall are obtained at a set oven temperature of 700 °C. At these operation points the simulation underestimates the cooling effect through steam reforming. The according maximum deviations are below 5 K. Hence, the temperature spread in the measuring plane is below 7 K the results still show room for improvement.

Nonetheless, when neglecting temperature deviations unaccounted for, the simulation results for 750 °C and 800 °C show good accordance to the respective measurements. The averaged differences between simulation and measurement thereby are below 2.5 K.

Concluding it can be stated, that the simulation results regarding the investigated gas species on the cell anode as well as the temperature distributions show good agreement to measurements. Therefore, the simulation is considered validated.

5.3 CFD Results

Basing on the last section, where the validity of the simulation was shown, the following section aims to state relevant data gathered from CFD calculations. Therefore, temperature distributions on the cell anode and cathode are stated. Further, the electric potential on the cathode as well as the mole fraction of oxygen in the cathode flow field are given. The mol fractions for methane, hydrogen, carbon monoxide, carbon dioxide and water in the anode flow field will be provided as well. The respective images are not in scale to each other. The positions of the used cutting planes are stated in the appendix.

To give a valid statement on the behaviour of the species in the anode flow field, two orthogonal cutting planes were used. Figure 47 illustrates the positions of these planes.

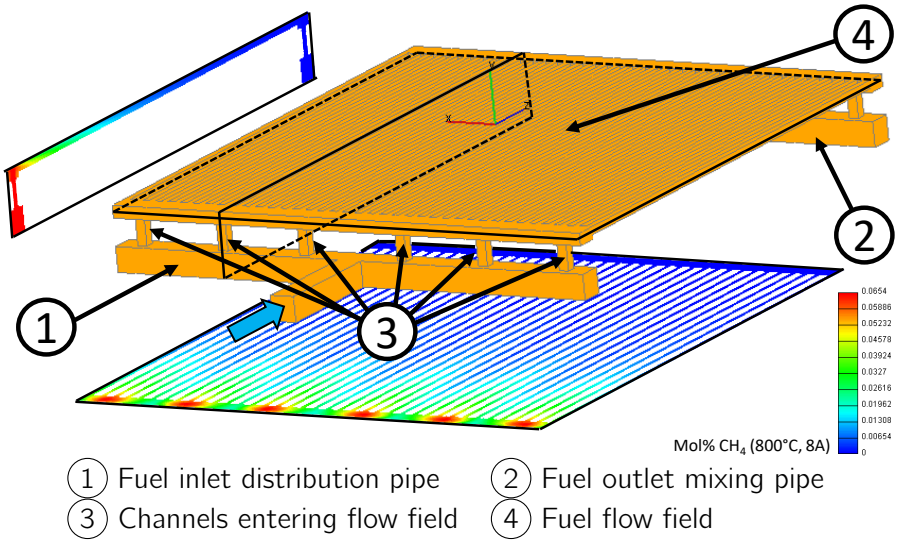

(1) Fuel inlet distribution pipe (2) Fuel outlet mixing pipe
(3) Channels entering flow field (4) Fuel flow field

Figure 47: Illustration of the CFD fuel volume and the cutting planes used to gather CFD results to investigate the fuel composition

Further, to be able to compare the CFD results, for 700 °C, 750 °C, and 800 °C colorbars use coherent scales. Exceptions to this are the CFD results for the electric potential on the cathodes. This is due to the rather small difference in electric potenial in a single step while the overall change in electric potential is rather high. In order to be able to state meaningful results, the scales of the colorbars for electric potential consider only the differences in the viewed volume cells.

CFD Results for 700 Degree Celsius

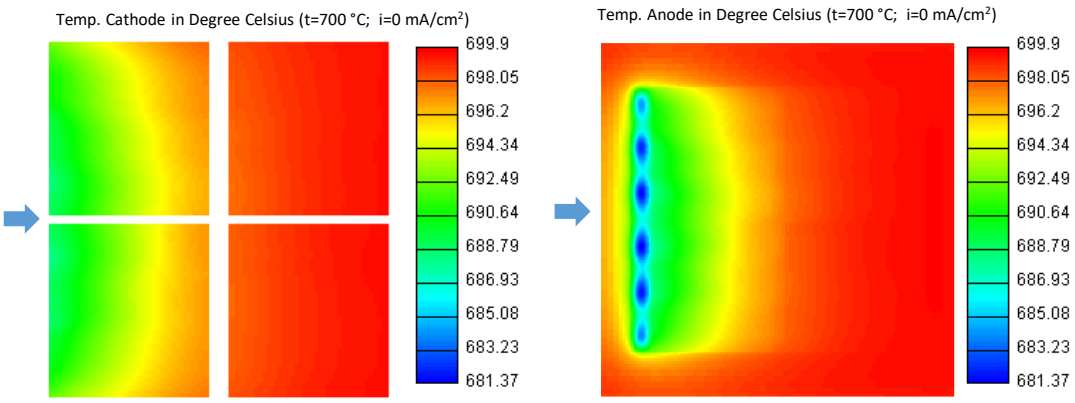

(a) (b)

Figure 48: Plots of the temperature distribution on anode and cathode at 700 °C and $i = 0\ \frac{mA}{cm^2}$

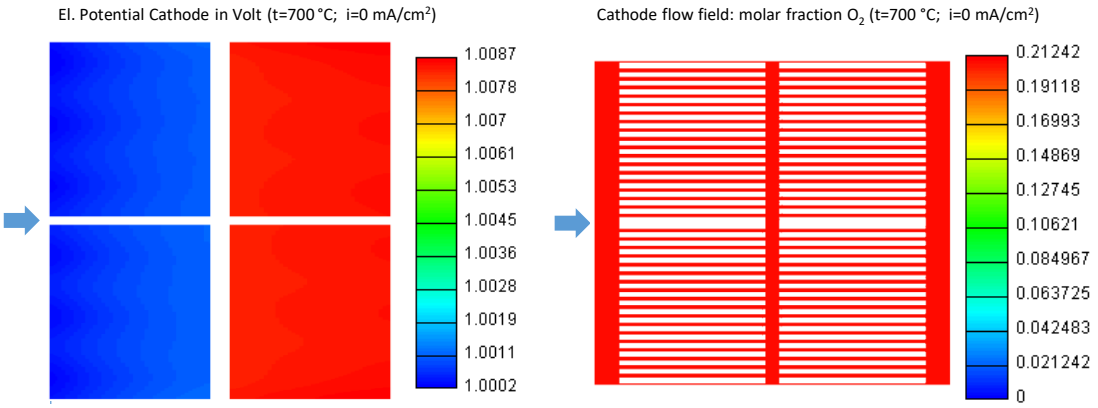

(a) (b)

Figure 49: Plots of calculated electric potential on the cathodes and the O_2 volume fraction in the cathode flow field at 700 °C and $i = 0\ \frac{mA}{cm^2}$

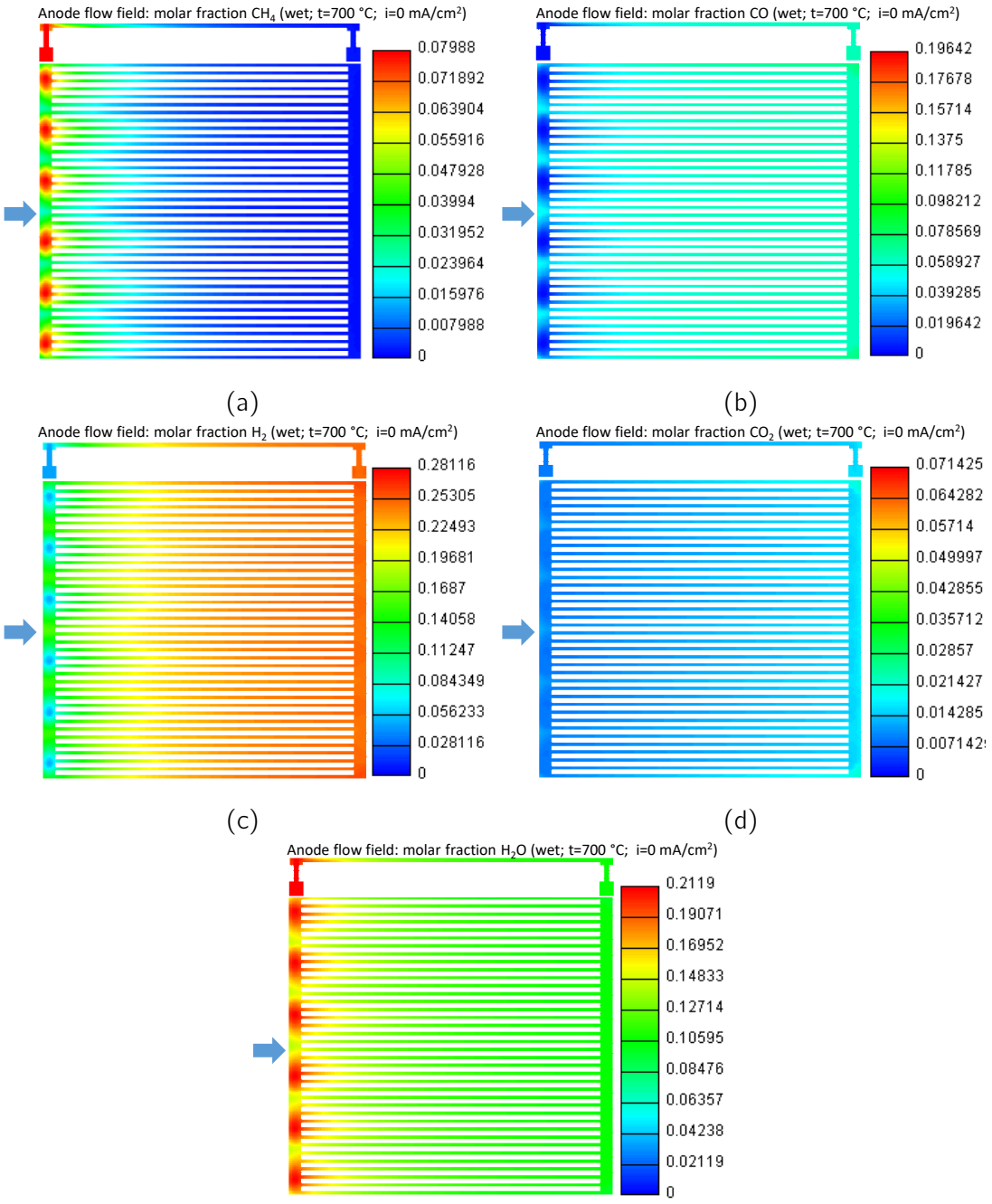

Figure 50: Plots of species (wet) in the anode flow field at 700 °C and $i = 0\ \frac{mA}{cm^2}$

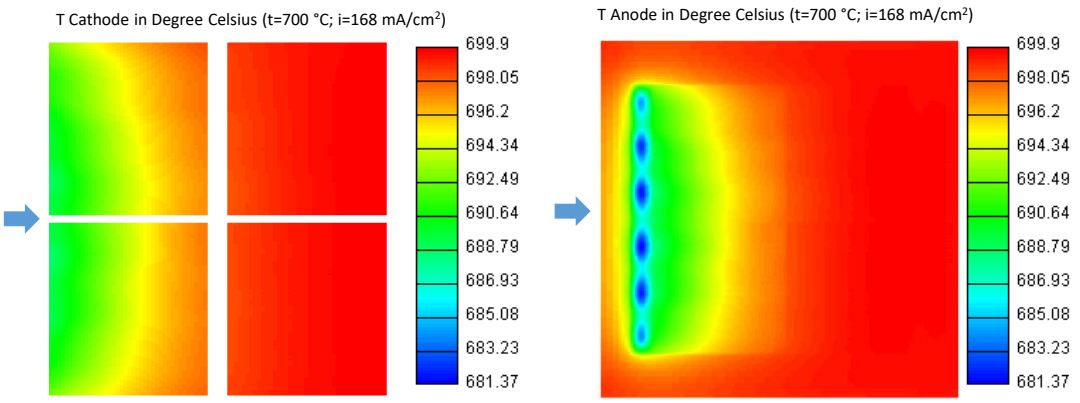

(a) (b)

Figure 51: Plots of the temperature distribution on anode and cathode at 700 °C and $i = 168\ \frac{mA}{cm^2}$

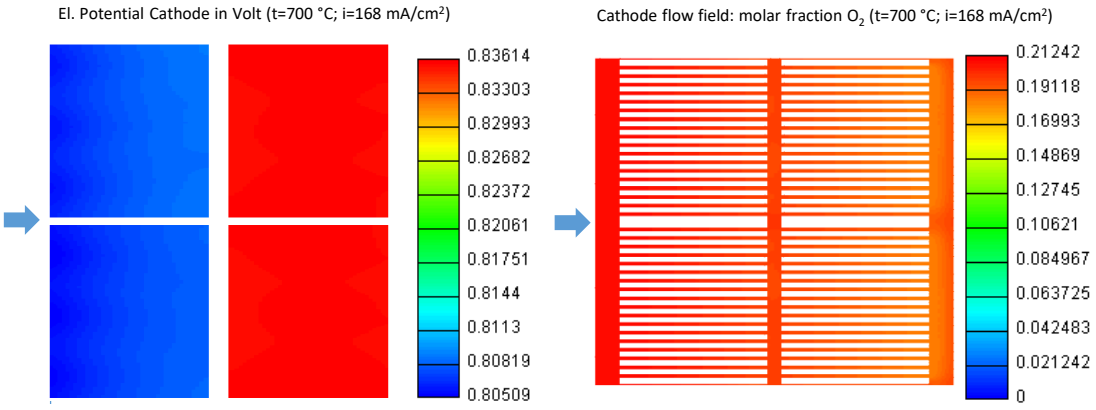

(a) (b)

Figure 52: Plots of calculated electric potential on the cathodes and the O_2 volume fraction in the cathode flow field at 700 °C and $i = 168\ \frac{mA}{cm^2}$

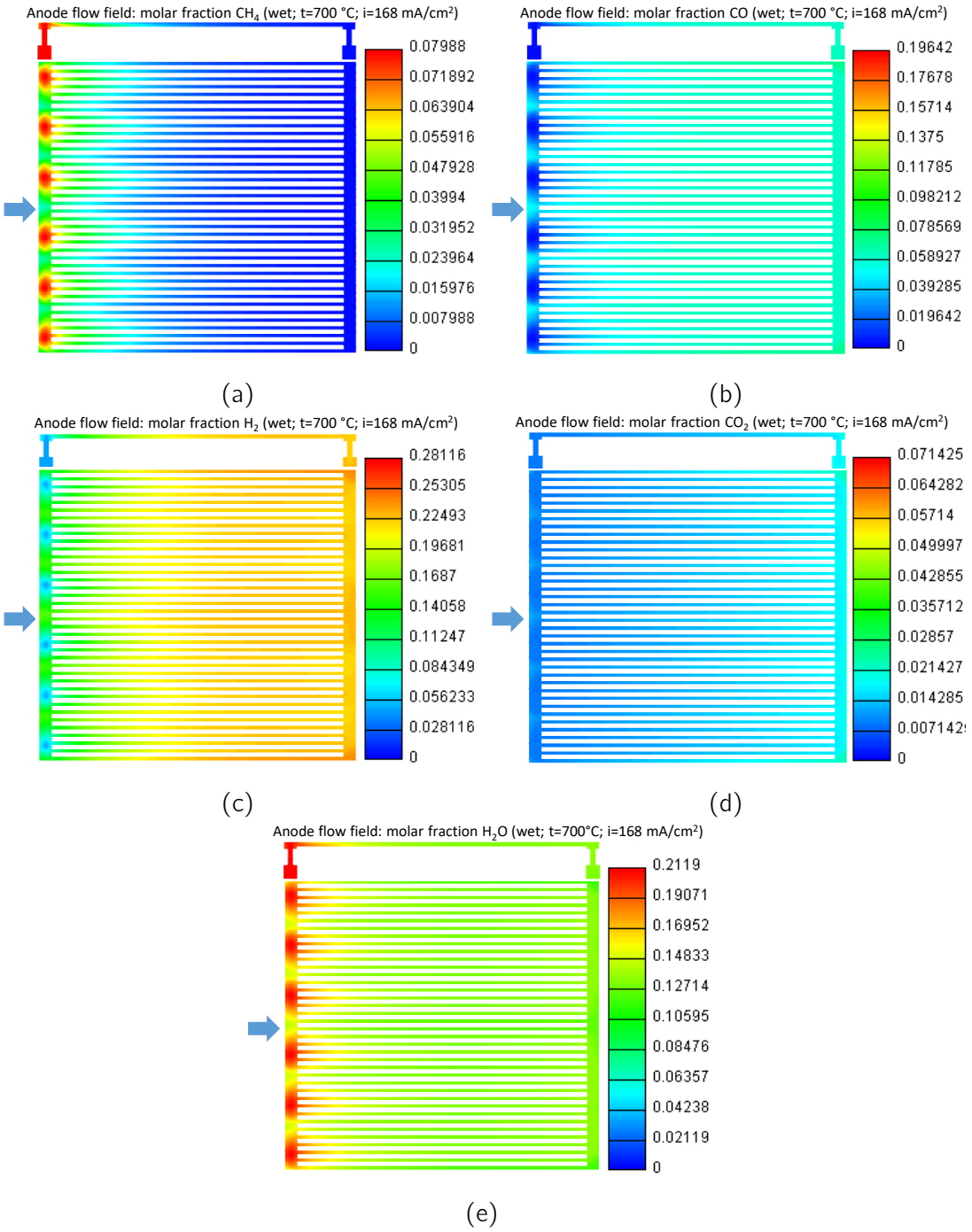

Figure 53: Plots of species (wet) in the anode flow field at 700 °C and $i = 168\ \frac{mA}{cm^2}$

CFD Results for 750 Degree Celsius

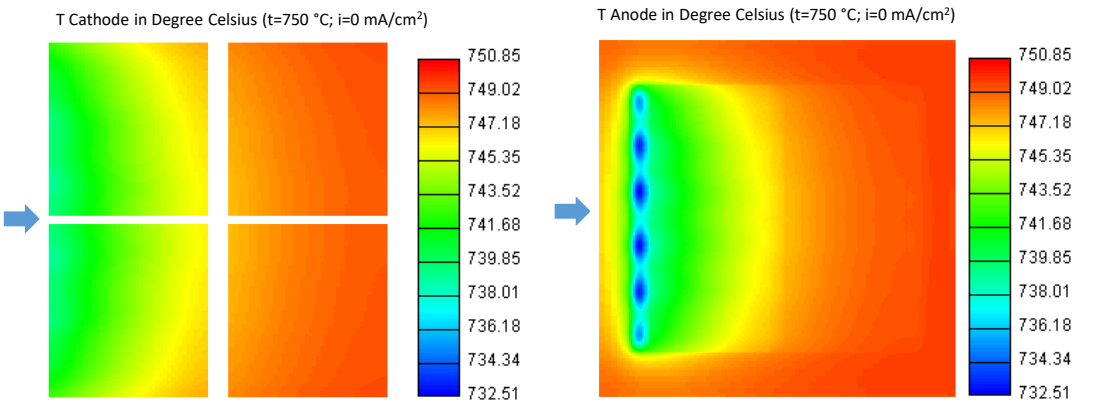

(a) (b)

Figure 54: Plots of the temperature distribution on anode and cathode at 750 °C and $i = 0\ \frac{mA}{cm^2}$

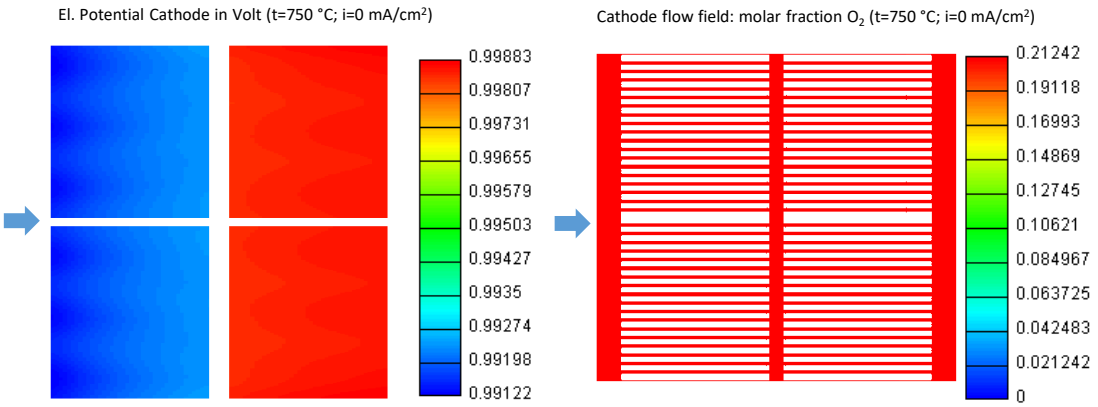

(a) (b)

Figure 55: Plots of calculated electric potential on the cathodes and the O_2 volume fraction in the cathode flow field at 750 °C and $i = 0\ \frac{mA}{cm^2}$

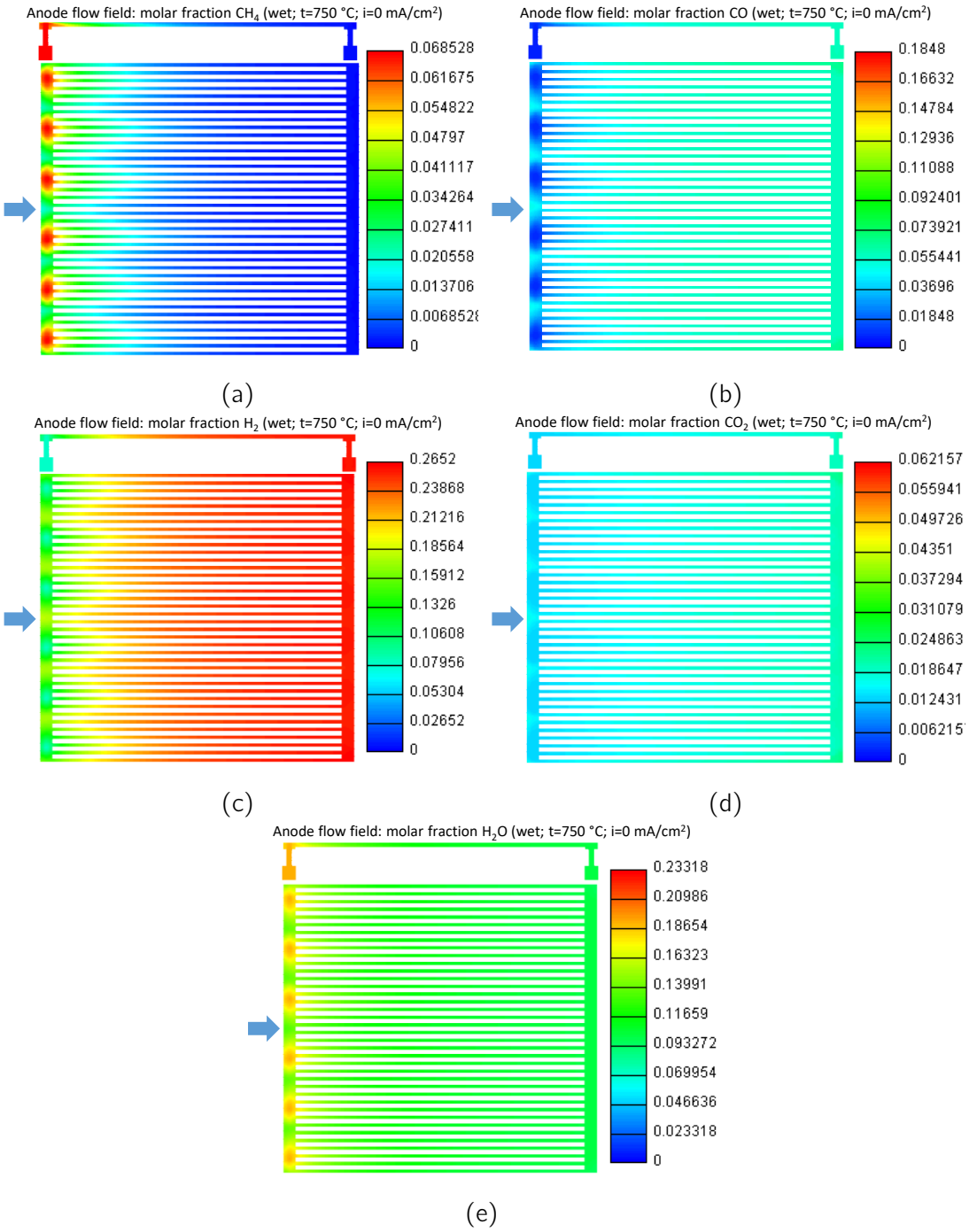

Figure 56: Plots of species (wet) in the anode flow field at 750 °C and $i = 0\ \frac{mA}{cm^2}$

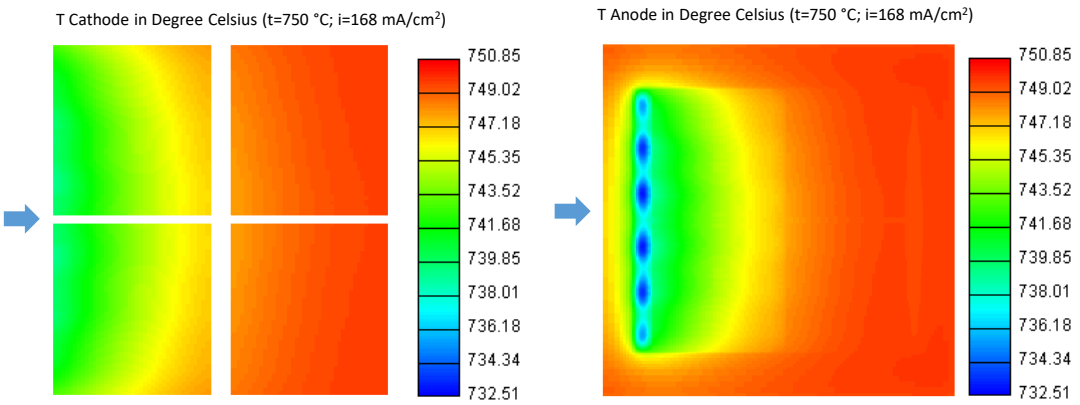

(a) (b)

Figure 57: Plots of the temperature distribution on anode and cathode at 750 °C and $i = 168\ \frac{mA}{cm^2}$

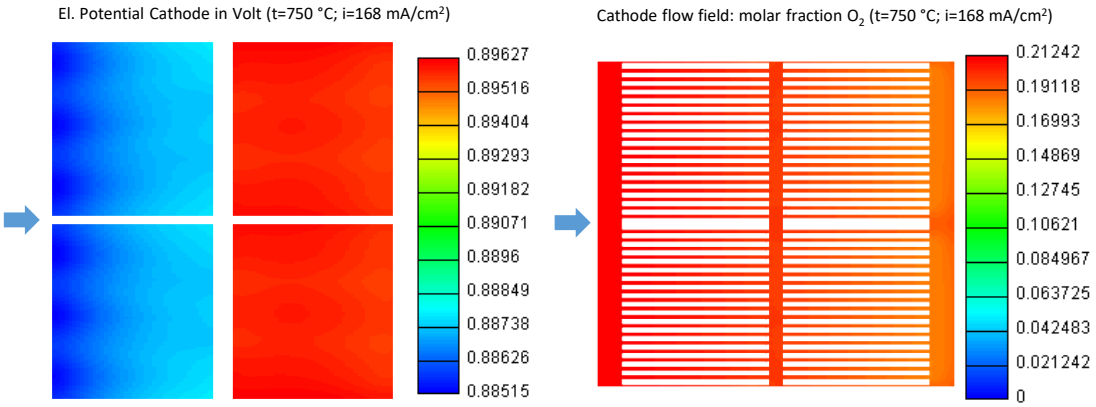

(a) (b)

Figure 58: Plots of calculated electric potential on the cathodes and the O_2 volume fraction in the cathode flow field at 750 °C and $i = 168\ \frac{mA}{cm^2}$

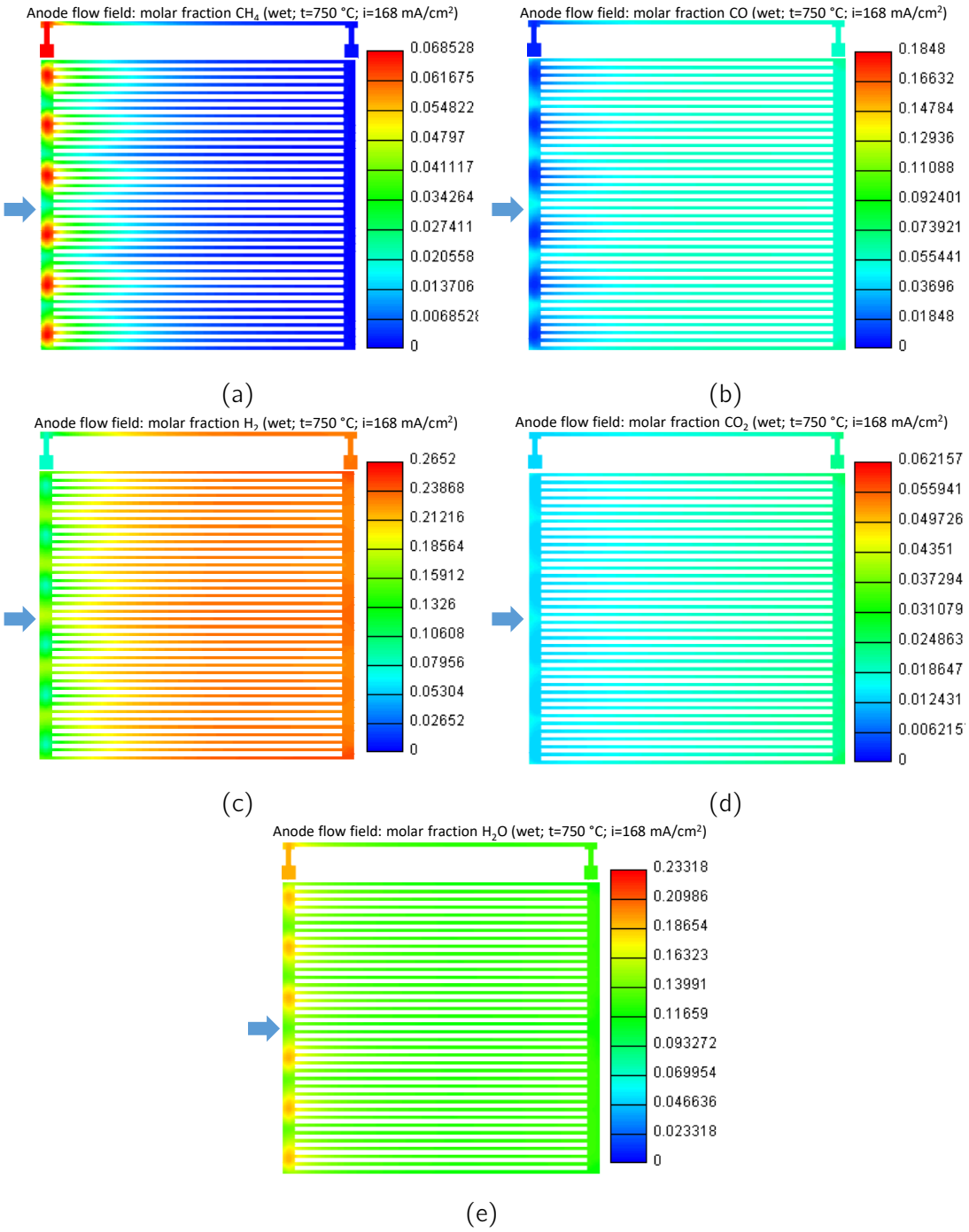

Figure 59: Plots of species (wet) in the anode flow field at 750 °C and $i = 168\ \frac{mA}{cm^2}$

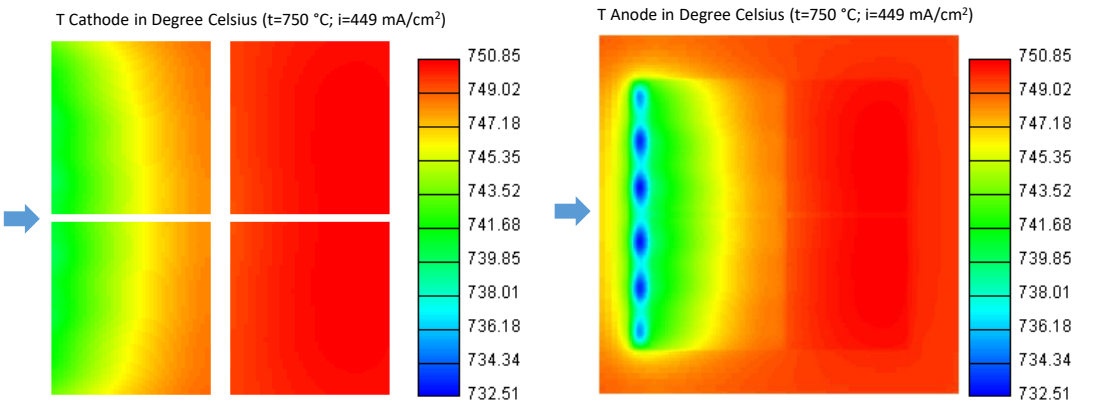

(a) (b)

Figure 60: Plots of the temperature distribution on anode and cathode at 750 °C and $i = 449\ \frac{mA}{cm^2}$

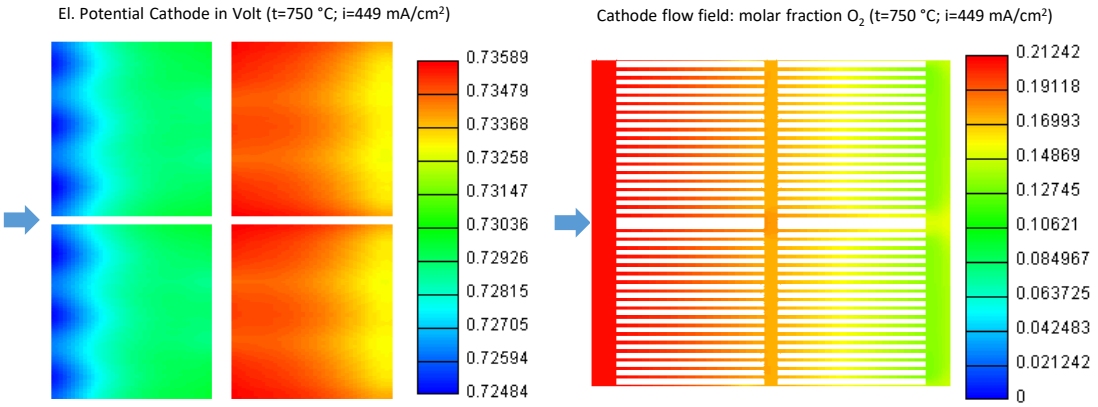

(a) (b)

Figure 61: Plots of calculated electric potential on the cathodes and the O_2 volume fraction in the cathode flow field at 750 °C and $i = 449\ \frac{mA}{cm^2}$

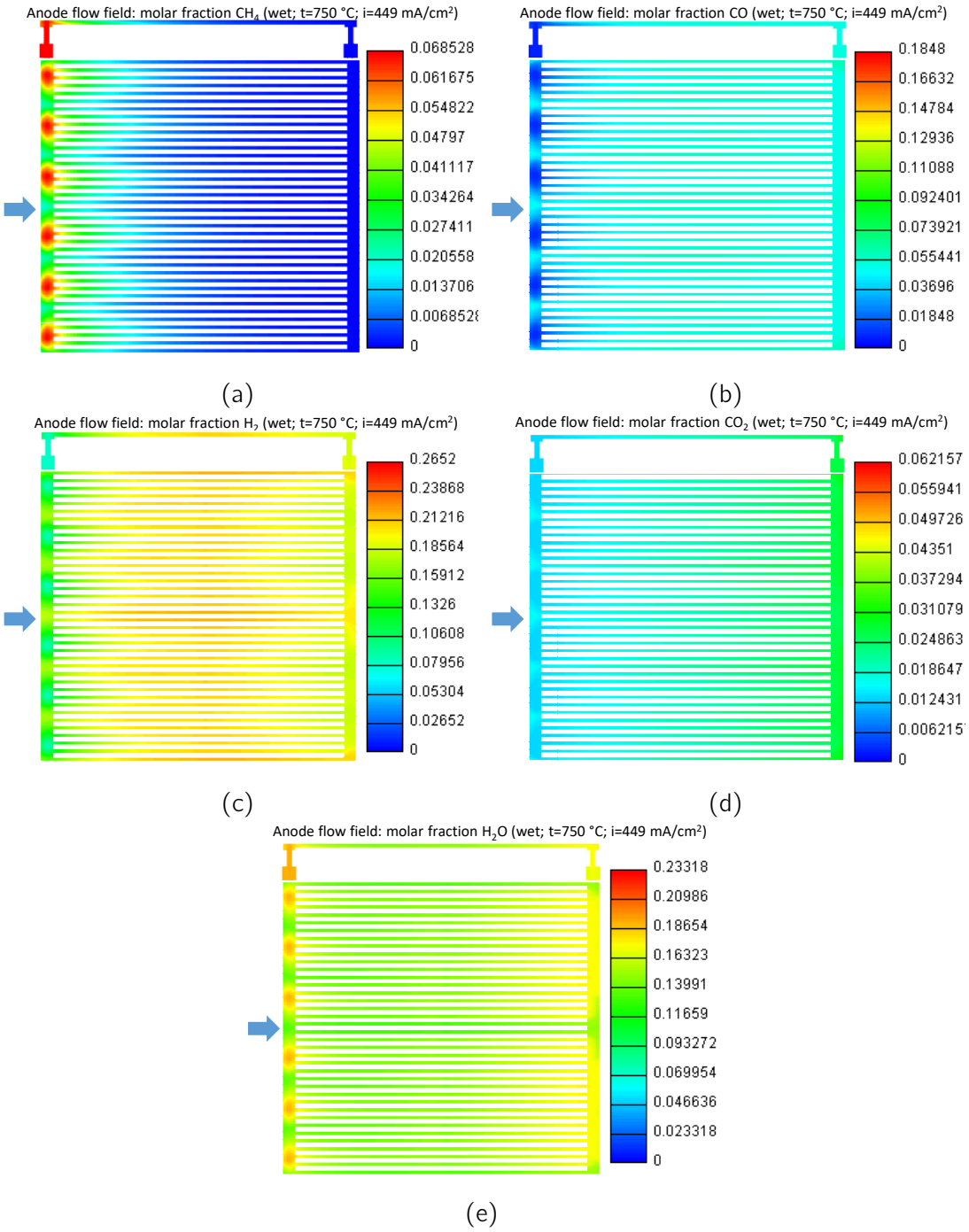

Figure 62: Plots of species (wet) in the anode flow field at 750 °C and $i = 449\ \frac{mA}{cm^2}$

CFD Results for 800 Degree Celsius

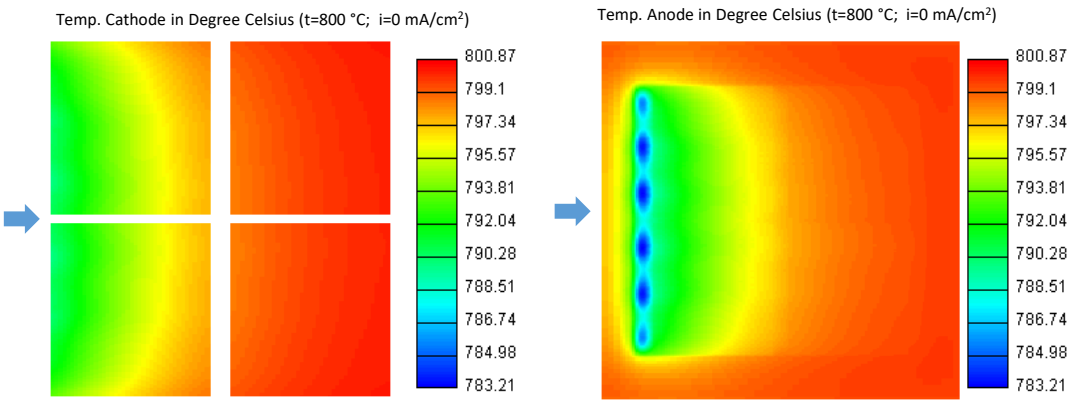

(a) (b)

Figure 63: Plots of the temperature distribution on anode and cathode at 800 °C and $i = 0\ \frac{mA}{cm^2}$

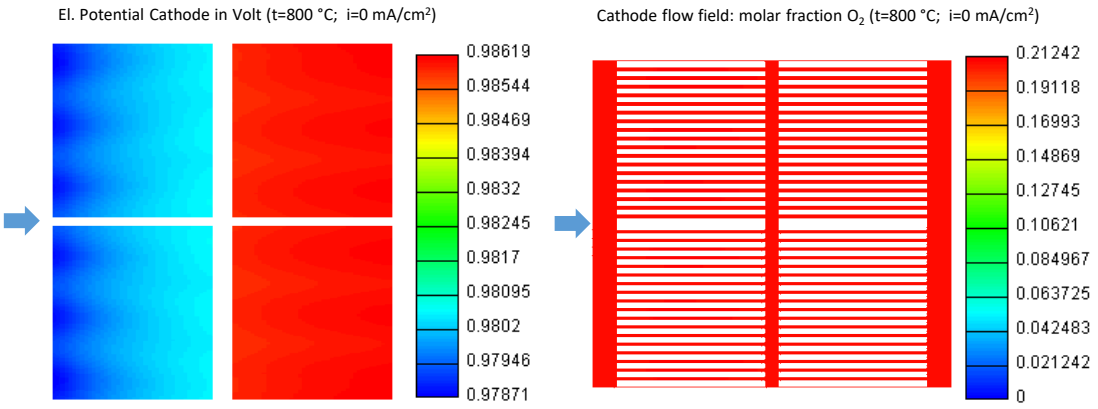

(a) (b)

Figure 64: Plots of calculated electric potential on the cathodes and the O_2 volume fraction in the cathode flow field at 800 °C and $i = 0\ \frac{mA}{cm^2}$

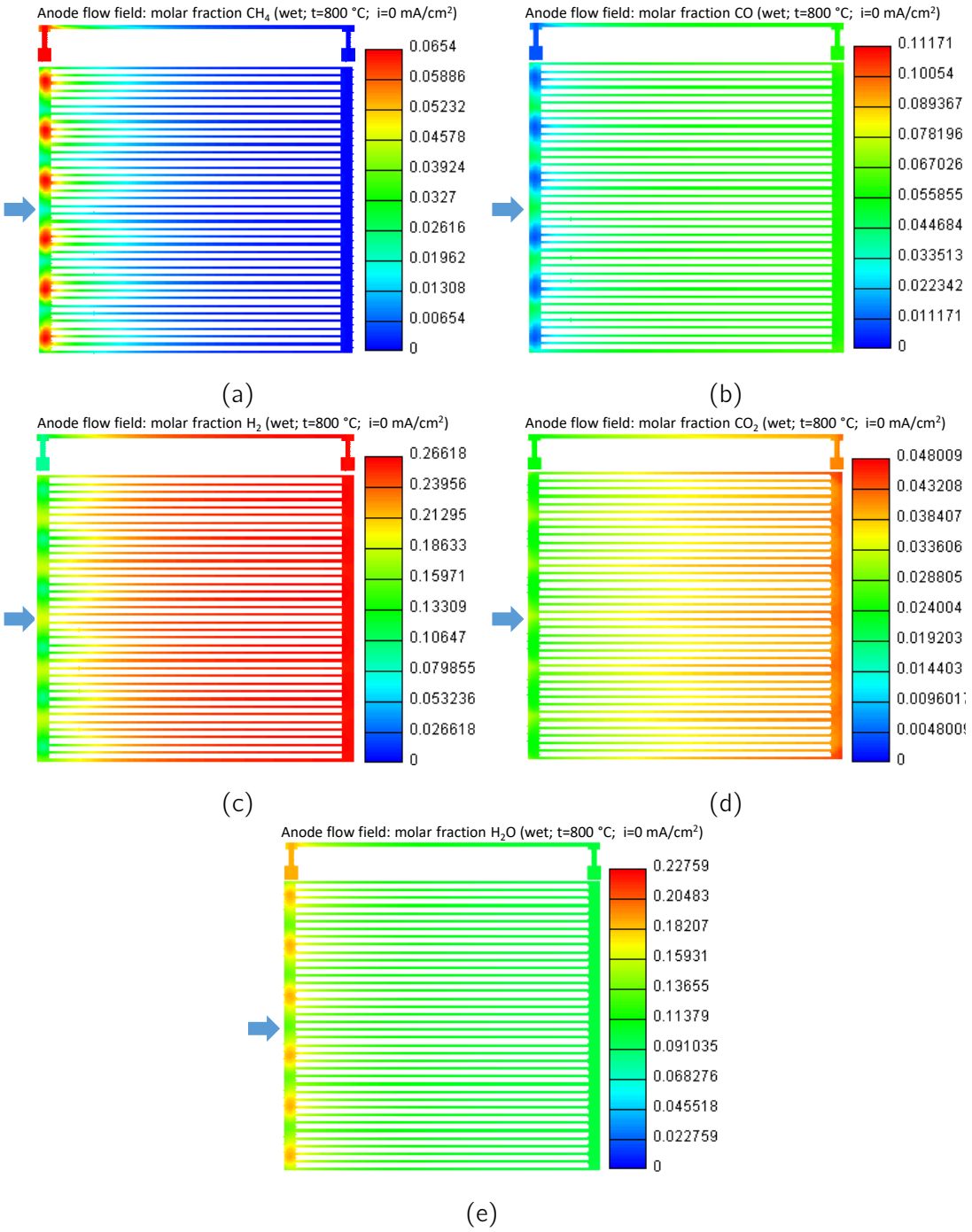

Figure 65: Plots of species (wet) in the anode flow field at 800 °C and $i = 0\ \frac{mA}{cm^2}$

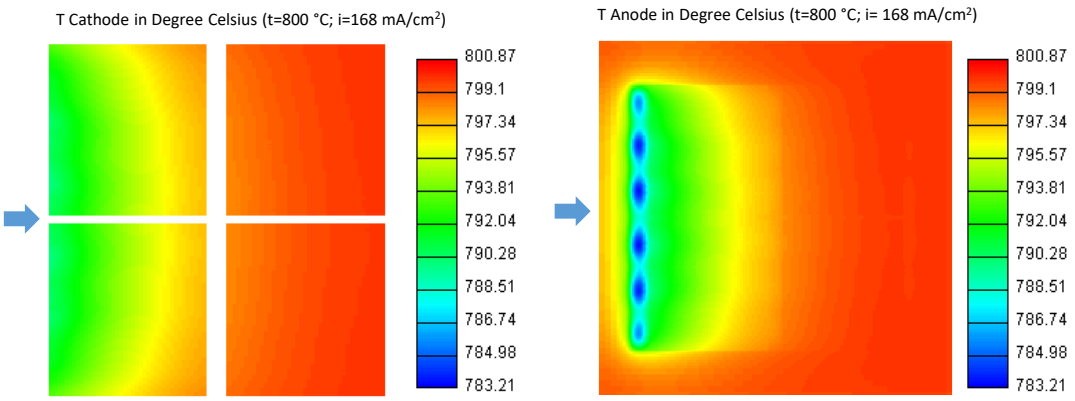

(a) (b)

Figure 66: Plots of the temperature distribution on anode and cathode at 800 °C and $i = 168\ \frac{mA}{cm^2}$

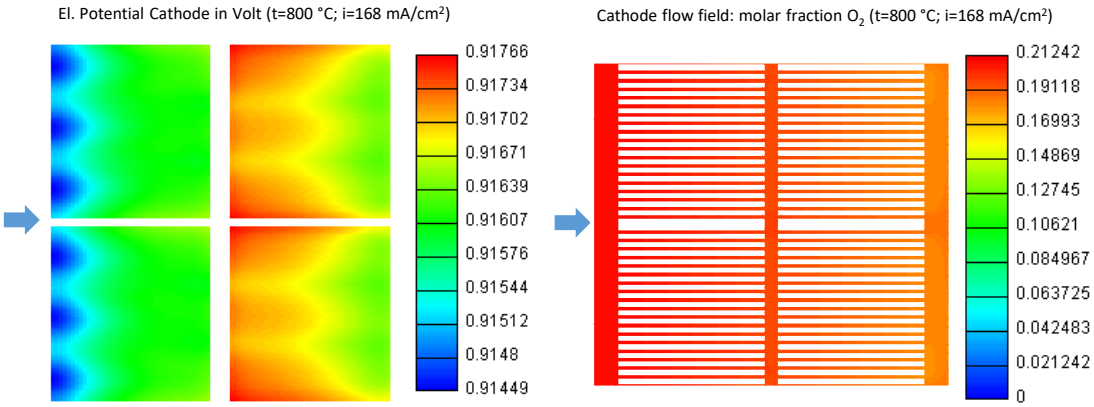

(a) (b)

Figure 67: Plots of calculated electric potential on the cathodes and the O_2 volume fraction in the cathode flow field at 800 °C and $i = 168\ \frac{mA}{cm^2}$

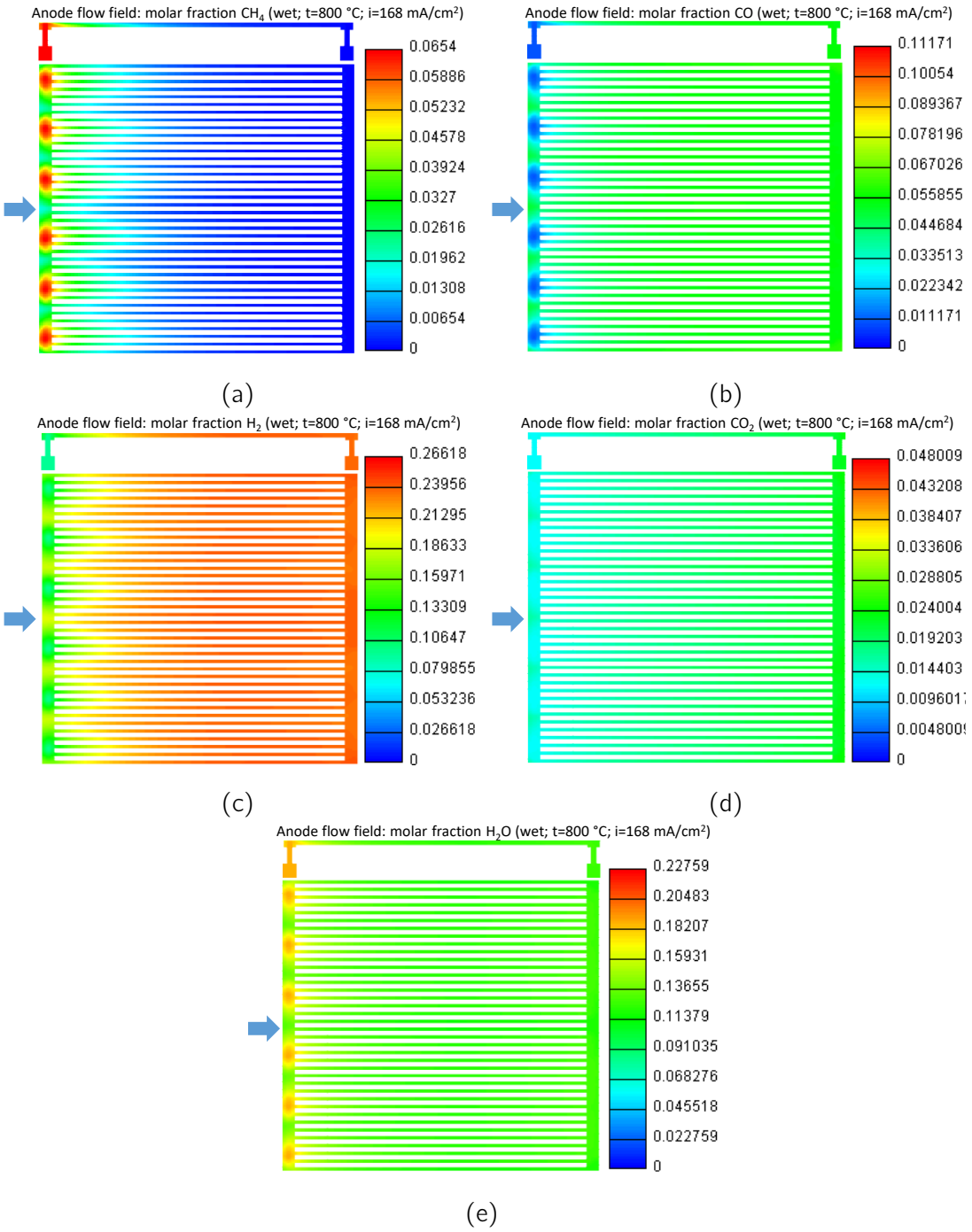

Figure 68: Plots of species (wet) in the anode flow field at 800 °C and $i = 168\ \frac{mA}{cm^2}$

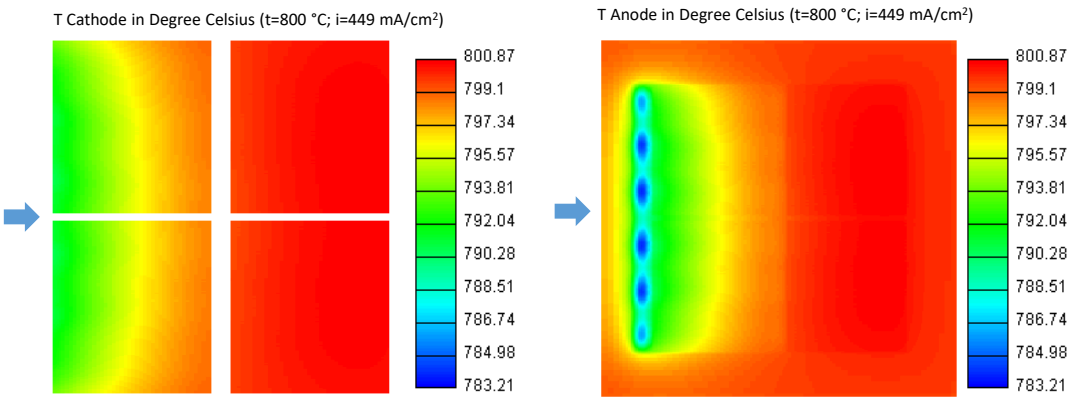

(a) (b)

Figure 69: Plots of the temperature distribution on anode and cathode at 800 °C and $i = 449\ \frac{mA}{cm^2}$

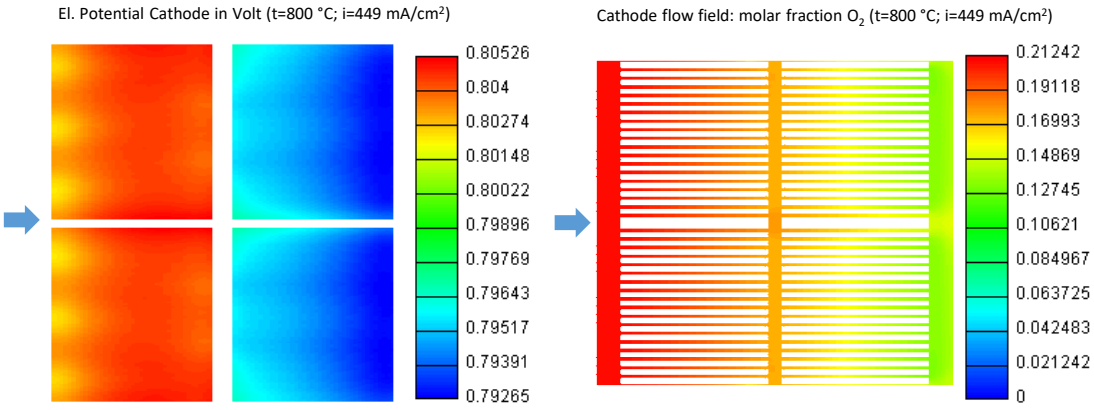

(a) (b)

Figure 70: Plots of calculated electric potential on the cathodes and the O_2 volume fraction in the cathode flow field at 800 °C and $i = 449\ \frac{mA}{cm^2}$

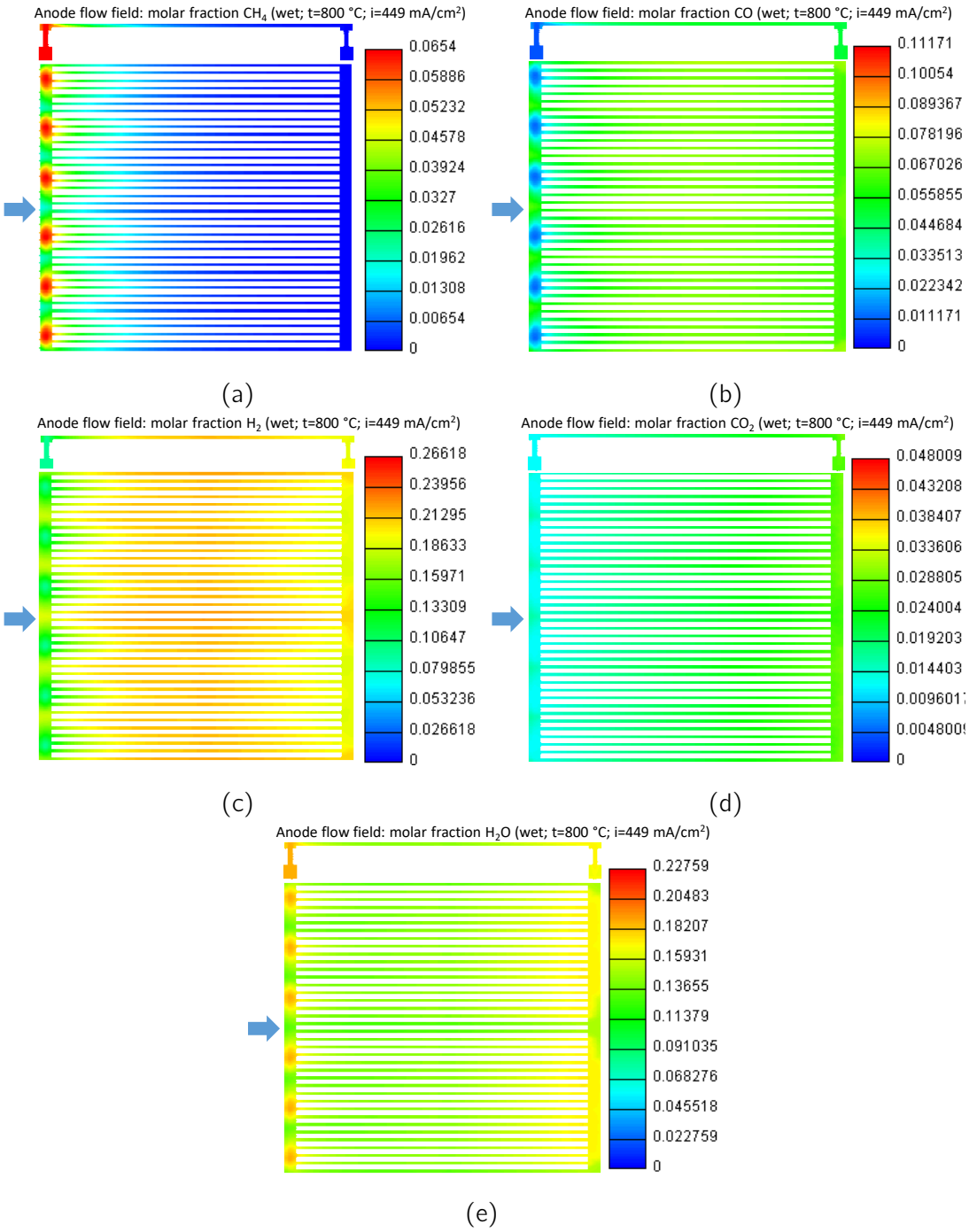

Figure 71: Plots of species (wet) in the anode flow field at 800 °C and $i = 449\ \frac{mA}{cm^2}$

Figures 48 and 51 show the temperature distributions at cell cathode and cell anode for 700 °C while figures 54, 57, 60 and figures 63, 66, 69 show the temperature profiles for 750 °C and 800 °C. From the given figures it can be seen that the simulated testbed shows qualitatively the same behaviour for all investigated oven temperatures.

The cooling effect of steam reforming is clearly visible in all simulations. The temperature decrease can be accounted for by the endothermic nature of steam reforming reactions (see chapter 2.3.3). The temperature difference occuring on the cell anode is 18 K, while the decrease on the cathode side of the cell is 10 K for all simulations. Especially on the anode side of the cell sharp local decreases in temperature can be noticed. These sharp decreases are located at the positions where the fuel channels leading from the common inlet mixing pipe to the anode flow field transport methaneous fuel to catalytic regions. A possible explanation for this locally occuring cooling effect is the presence of a stagnation point for the fuel entering the anode flow field. This is because the fluid entering the flow field is deflected at the anode, changes its direction and keeps on flowing in a right angle to the previous flow direction. Further it can be seen that the cooling effect is more pronounced the closer the single fuel inlets lie to the common fuel inlet channel.

Main catalysts for the steam reforming are the anode itself as well as the nickel mesh used to establish electrical contact (see chapter 3). As expected, at higher current densities a slight temperature increase in the areas of the cell cathodes can be noticed. Since, however, the setup only investigates a single cell, the heating effect due to cell operation is rather weak compared to the cooling effect due to steam reforming. The fact that the cooling effect due to steam reforming shows about the same magnitude for all three investigated oven temperatures (700 °C, 750 °C, 800 °C) was unexpected. The molar fraction of methane, which had to be adapted for each simulation, shows no significant influence on the temperature profile. An explanation can be given by looking at the geometry of the flow field where the stagnation point explained above forces reforming to take place at a very isolated area. It is therefore possible that the cooling effect through methane reforming is not limited by the availibility of methane.

Figures 49 and 52 show the electric potential and the mol fraction of oxygen in the cathode flow field for 700 °C while figures 55, 58, 61 and 64, 67, 70 show the values for 750 °C and 800 °C respectively.

With the exception of the operating point at 800 °C and current densitiy of $i = 449\ \frac{mA}{cm^2}$, the cathode row close to the fuel inlet displays a lower electric potential than the cathode row close to the fuel outlet. This can be explained by the availibility of fuel. Not all of the methane inserted into the anode flow field has been reformed in the area of the cathode row close to the fuel inlet. Therefore, less hydrogen is available. Since hydrogen shows the fastest reaction behaviour at a nickel anode (see chapter 2.3), it represents the main

fuel for SOFCs. Subsequently the electric potential of the cathode row close to the fuel inlet position is lower than the potential of the second row, where almost all of the available methane has been reformed to hydrogen and carbon monoxide. A second possible factor influencing the electric potential at the first cathode row is the lower temperature resulting from the endothermic behaviour of the steam reforming reaction. At higher current densitites the impact of the cooling effect through endothermic steam reforming is reflected in the cathodes electric potentials.

Another factor influencing the electric potential on the cathodes is the distribution of fuel in the anode flow field. Especially at higher current densities (e.g. figures 58-a and 67-a), the effect of the local uneven distribution of fuel is clearly visible. This uneven distribution is caused by the discontinous insertion of fuel into the anode flow field though six channels leading gas from the fuel inlet distribution pipe into the anode flow field. It can be seen that in areas close to the fuel inlet a higher amount of fuel is present. This subsequently leads to a higher electric potential on the cathodes in these areas. Another observation obtained by looking at the distribution of electric potential is that on the edgeds of the cathodes the electric potential is higher than in cathode areas located more central. This, again, can be explained with local availability of fuel. Since at the edges of the cell's cathodes less fuel is be consumed, a higher fuel concentration is available which subsequently leads to a higher cathode potential. Furthermore, at high current densities (e.g. $i = 449\ \frac{mA}{cm^2}$), a decrease of oxygen in the cathode flow field, especially in the area of the cathodes themselves, can be observed (see figures 58-b and 61-b). This can be explained by the transport of oxygen ions through the cell (see chapter 2).

Finally, the gas species in the anode flow field can be seen from figures 50 and 53 for 700 °C, figures 56, 59 and 62 for 750 °C as well as 65, 68, and 71 for 800 °C. Every subfigure holds two orthogonal cutting planes, as illustrated in figure 47.

Looking at the molar fraction of methane (see subplots a), results indicate that the amount of CH_4 that gets converted to H_2 and CO via steam reforming is independent of the drawn current. This finding is in accordance to the measurements displayed in chapter 3. Further, methane shows the same conversion behaviour for all three investigated temperatures. It has to be noted, however, that due to the configuration of the test rig the fuel composition entering the flow field-cell assembly also varies depending on the test rig's temperature. This fact was taken into consideration when setting up the different CFD calculations (see chapter 4). Nonetheless, using the results obtained, no final conclusion regarding the temperature dependence of the reforming behaviour in the test rig can be drawn.

At lower current densities the hydrogen producing effect of the steam reforming reaction is clearly visible (see subplot c in figures 50, 56 and 65). As the current drawn is increased, hydrogen is consumed as a fuel. Therefore, at high current densities, the molar fraction of

hydrogen decreases over the course of the flow field. Since the edges and the middle of the cell are not covered by cathodes, no fuel is consumed in these areas. This subsequently leads to an increased local concentration of hydrogen in the middle and on the outer edges of the flow field. Furthermore, the figures stating the gas species in the anode flow field show that more hydrogen is consumed as fuel over the length of the flow field in the areas where methane-rich fuel is inserted into the flow field through inlet channels (see subplots c). A likely explanation for this behaviour is that in areas with a high methane concentration steam reforming of methane takes place faster than in areas with a low methane concentration. Subsequently, the reforming reactions take more time to produce hydrogen in areas with a lower methane concentration. Therefore, not all of the hydrogen present in the fuel mixture is available for consumption through cell operation over the full length of the flow field. Further it can be seen at high current densities ($i = 449\ \frac{mA}{cm^2}$, see figures 62-c and 71-c) that in the area where the cathodes are positioned the local consumption of hydrogen is higher than in the rest of the anode flow field. The areas, where the least amounts of hydrogen are consumed, are the sections between the cathodes and the fuel channels at the edge of the flow field.

In addition, the molar fractions of carbon monoxide and carbon dioxide in the anode flowfield are stated in the figures 50, 53 - subplots b and d for cell operation at 700 °C as well as 56, 59, 62 and 65, 68, 71 - subplots b and d for cell operation at 750 °C and 800 °C. As discussed in chapter 2, the molar fractions of carbon monoxide and carbon dioxide are directly linked to the molar fractions of methane, hydrogen and water via the steam reforming reaction and the water-gas shift reaction and their respective equilibrium constants.

The impact of the methane reforming reaction on the molar fraction of CO can be clearly seen at the beginning of the flow field (see subplots b and d). In this area, the decrease of methane is accompanied with the increase of hydrogen and carbon monoxide. As shown in chapter 2, the steam reforming of methane can be considered as the dominant reaction at elevated temperatures. However, the water-gas shift reaction still displays influence on the overall gas composition in the anode flow field. A main indicator for this is the increase of CO_2 in the flow field. It can be noticed that the increases of CO_2 and CO concentrations take place in different areas of the flowfield. While CO is produced mainly at the fuel inlet position, the molar fraction of CO_2 shows a steady increase along the the fuel path in the anode flow field. A possible explanation for this observation is that the water-gas shift reaction requires CO in order to take place. This CO is mainly produced by the methane steam reforming reaction. As already mentioned before, the boundary conditions used take into account the steam reforming inside the test rig before the gas flows into the anode flow field. Subsequently, a small amount of CO is already present in the fuel mixture (see chapter 3). It is, however, safe to assume that the water-gas shift reaction occurs further downstream in the anode flow field, where the steam reforming of methane is nearly complete and higher amounts of CO are available. Again, the uneven fuel distribution at the flow field

inlet affects the concentrations of both CO and CO_2. Further, the possible consumption of CO as fuel has to be taken into consideration.

The water inserted into the testbed (see subplots e) by a steam generator (see chapter 3) is consumed for the most part in the methane steam reforming reaction. However, at higher current densities, it can be noticed that in the area of the cathode row close to the fuel outlet the mole fraction of water increases (see subplot e in figures 62 and 71). It can be assumed that this water increase in the anode flow field is coupled with the oxygen decrease in the cathode flow field and therefore is subsequently driven by the cell operation. The increase of water is located in the area where the cathodes are positioned. Likewise, the sections between the cathodes and at the edge of the flowfield show limited increase in the concentrations H_2O.

A finding clearly visible when looking at the fuel species in the anode flow field is the major influence of geometry on the distribution of species. Methane-rich fuel is inserted into the flow field through just six pipes. At the positions of these pipes high amounts of unreformed methane are present, whereas between the pipes the concentration of methane is low. The impact of this inhomogeniously distributed fuel composition at the inlet of the flow field can be seen in an uneven fuel distribution further downstream. This might show potential for optimisation, since the inhomogenous fuel distribution at the inlet of the flow field not only affects the distribution of electric potentials in the cathodes by the local availability of fuel. It also affects the electric potentials near the fuel inlet via a cooling effect.

Optimising the geometry of the fuel flow field could therefore not only lead to a higher fuel utilisation, but also to a higher cell lifetime by decreasing temperature gradients through steam reforming.

6 Conclusions and Outlook

This thesis had the objective to simulate an segmented single SOFC test bed operating on methaneous fuel. The simulation was set up using data from a test bed. Further, the obtained simulation results were validated using this data. Concluding it can be said that the simulation results show good accordance with measurements. For a further discussion of the obtained results, the focus will be laid on three main aspects of this thesis: The thermal results, the results in regard to the investigated chemical composition of the fuel along the cell and the electrical fit of the obtained IV-curves.

The accuracy of the simulated thermal results to respective measurements can be regarded as good. The deviations between simulation and measurement are below 10 K in all considered cases. Depending on the operating point, said differences are even lower up to a mean deviation below 1 K. Despite this good agreement between simulation and measurement the results still have to be investigated further. The main drawback regarding the obtained results is the overall small temperature difference. Heating elements, which can simulate stack-like temperature distributions as shown by Fabian Rasinger [51] and Daniel Schaffer [53], were not used in the experiments this thesis was based on. Without those, the temperature drop caused by steam reforming reactions is less than 20 K directly at the anode and 7 K in the measuring plane. This small temperature range still offers room for improvement, just as the K-type thermocouples do which have a limited accuracy.

Simulations of the chemical kinetics using the parameters found for the Arrhenius equation showed good accordance with measurements. On the downside, these parameters are 4 to 5 times smaller than typical parameters found in literature (for examples, see [2], [54], [55], [43] and [64]). There are several possible explanations for this fact. The first one is that the region of the testbed, where steam reforming of the fuel would take place, had to be assumed. Some papers state the opinion that fuel reforming takes place only at the surface of the anode [11]. It has to be questioned, however, if this assumption can be applied directly to the given testing setup. One possible approach for explaining the mentioned deviation is that the given test setup differs from setups considered in literature. For example, in the given configuration, nickel meshes are used to establish contact between anode interconnect and the YSZ anode, therefore providing an additional catalyst. Further, alloys used for pipes as well as for the interconnect and anode flow field provide some amount of cataytic material through their compounds. This subsequently leads to another issue with the CFD

simulation. AVL FIRE® only allows the definition of a single selection of cells in which reforming takes place. In this single selection only one set of parameters is used to define the chemical kinetics of the water-gas shift and steam reforming reaction. Thereby it is not possible to define multiple reaction rates, taking into consideration factors like the reduction of activation energy or the potentially larger reaction surface of a certain catalytic volume (e.g. for nickel mesh and anode). Since for the given test setup not all values needed to simulate chemical kinetics are known, experimental investigations on reaction rates may be necessary. Naturally, the accuracy of the fuel species measured along the anode flow field also has to be questioned. However, a seperate test run investigating the fuel species at cell inlet was conducted. Since the thereby obtained results showed good accordance to the provided measurements, a systematic measuring errors seems unlikely.

Chemical kinetics in the investigated setup have a major influence on the simulated temperature distributions. Therefore, further improvement of the accuracy of reforming reactions could subsequently lead to an improvement in temperature results. To improve future measurements using hydrocarbon fuels, a complete overhaul of the testbed has to be considered. As stated in this thesis, reforming reactions take place in the pipes inside the oven test bench. In order to obtain meaningful results, a more controlled testing environment is desireable. One approach would be to use ceramic piping. This would combine the non-catalytic nature of ceramic materials with the ability to pre-heat gases before sending them into the fuel cell setup. Another approach to solve the problem would be the use of cooled pipes. This, however, has the downside of potentially inserting a cooled gas into the test setup. Depending on the desired test results, using cooled pipes therefore may be not purposeful.

The fitting of the IV-curves displays several drawbacks. As already stated by Daniel Schaffer [53], an asymmetrical spread between measured IV-curves can not be reproduced using a symmetrical CFD model. Further, in order to find an efficient procedure for fitting simulated IV-curves to measurements, fitting was concentrated on the linear ohmic region of the curve. In addition, the IV-curves were fitted using the mean values of the measured as well as the simulated electric potential on the cathodes. This represents a simplification, since the single cathode voltages are not reproduced to full accuracy using this method. However, results indicate that the impact of the drawn current is rather small at single cell level ($\Delta T < 1.5\,\mathrm{K}$ between $i = 0\ \frac{mA}{cm^2}$ and $i = 449\ \frac{mA}{cm^2}$). The necessity to fit simulations to measured IV-curves also represents a major obstacle. Although steps towards a semi-automatic fitting procedure already have been made, this procedure is not yet applicable for all measured curves. Therefore, this topic shows room for improvement.

This thesis represents a step towards a full and validated thermal, chemical and electrical simulation of solid oxide fuel cells. The next step would be to gather results from the testbed operating on methane and using the heaters to imitate stack-like conditions. Thereby the heating effect through fuel cell operation and the overlaying cooling effect caused by the

endothermic nature of the steam reforming reactions could be investigated. For further analysis of the temperature distribution on application scale, subsequent tests and simulations of fuel cell stacks will be neccessary.

References

[1] ABB. Advance Optima Kontinuierliche Gasanalysatoren; AO2000 Serie; Software-Version 5.1; Kurzanleitung für Installation, Inbetriebnahme und Bedienung, 2012.

[2] E. Achenbach and E. Riensche. Methane/steam reforming kinetics for solid oxide fuel cells. *Journal of Power Sources*, 52(2):283–288, 1994.

[3] K. Ahmed, P. Seshadri, and Y. Ramprakash et. al. Proceedings of the fifth international symposium on SOLID OXIDE FUEL CELLS (SOFC-V). pages 228–234, 1997.

[4] K. Ahmed et. al. Internal steam reforming of partially pre-reformes natural gas in SOFC stacks. In *Proc. Of. the 5th In. Symp. On Solid Oxide Fuel Cells*, page 228, Penington, NL, 1997.

[5] Vanesa Alzate-Restrepo and Josephine M. Hill. Effect of anodic polarization on carbon deposition on Ni/YSZ anodes exposed to methane. *Applied Catalysis A: General*, 342(1-2):49–55, 2008.

[6] Harlan U. Anderson and Frank Tietz. Interconnects. In K. Singhal, S.C. Kendall, editor, *High Temperature Solid Oxide Fuel Cells: Fundamentals, Design and Application*, pages 173–195. Elsevier, 2003.

[7] AVL AST. AVL AST Internal Documentation.

[8] AVL GmbH. Internal Documentation.

[9] AVL GmbH. Correspondence with Development Engineer, 2016.

[10] AVL GmbH. Fire v2014.2 - Electrification / Hybridization, 2016.

[11] P. Chinda, S. Chanchaona, P. Brault, and W. Wechsatol. A planar anode-supported Solid Oxide Fuel Cell model with internal reforming of natural gas. *EPJ Applied Physics*, 54(2), 2011.

[12] E. L. Cussler. *Diffusion, mass transfer in fluid systems*. Cambridge University Press, New York, 1 edition, 1984.

[13] Andrew Dicks. Hydrogen generation from natural gas for the fuel cell systems of tomorrow. *Journal of Power Sources*, 61(1-2):113–124, 1996.

[14] DOE. *Fuel Cell Handbook*. Department of Energy, 7th edition, 2004.

[15] Clément Dufour. Experimental validation of a segmented SOFC cell test equipment to simulate stack like conditions, 2016.

[16] Mohamed Elsharif. Experimental evaluation of a SOFC cell testing equipment towards determined temperature distributions, 2016.

[17] Craig Fisher. Solide Oxide Fuel Cells. `http://people.bath.ac.uk/cf233/sofc.php`. Accessed: 2017-01-03.

[18] Alexandre Gitz. Extension of a CFD Model for SOFC Fuel Cells and implementation of methane reforming, 2016.

[19] Deutsche Edelstahlwerke GmbH. Material Data-Sheet: X15CrNiSi25-21 - 1.4841, 2016.

[20] C. H. Hamman, A. Hamnett, and W. Vielstich. *Electrochemistry*. J. Wiley & Sons, New York, 1998.

[21] Martin Hauth. Einführung in die Brennstoffzellentechnik, 2016.

[22] H. Hisinuma et. al. Current status of planar SOFC development at Tokyo Gas. In *4th Int. symp. On Solid Oxide Fuel Fells*, page 153, Yokohame, Japan, 1995.

[23] Teruhisa Horita, Natsuko Sakai, Tatsuya Kawada, and Yokokawa Harumi. Oxidation and Steam Reforming of CH 4 on Ni and Fe Anodes under Low Humidity Conditions in Solid Oxide Fuel Cells. *Journal of The Electrochemical Society*, 134(4):1161–1168, 1996.

[24] Tatsumi Ishihara, Nigel M Sammes, and Osamu Yamamoto. Electrolytes. In K. Singhal, S.C. Kendall, editor, *High Temperature Solid Oxide Fuel Cells: Fundamentals, Design and Application*, pages 83–117. Elsevier, 2003.

[25] Ellen Ivers-Tiffe and Anil V Virkar. Electrode Polarisations. In K. Singhal, S.C. Kendall, editor, *High Temperature Solid Oxide Fuel Cells: Fundamentals, Design and Application*, pages 229–260. Elsevier, 2003.

[26] William B. Jensen. Faradays laws or Faradays law? *Journal of Chemical Education*, 89(9):1208–1209, 2012.

[27] Sadik Kakaç, Anchasa Pramuanjaroenkij, and Xiang Yang. A review of numerical modeling of solid oxide fuel cells. 32:761–786, 2007.

[28] Robert J Kee, Huayang Zhu, and David G Goodwin. Solid-oxide fuel cells with hydrocarbon fuels. *Proceedings of the Combustion Institute*, 30(2):2379–2404, 2005.

[29] Kevin Kendall, Nguyen Q Minh, and Subhash C Singhal. Cell and Stack Designs. In K. Singhal, S.C. Kendall, editor, *High Temperature Solid Oxide Fuel Cells: Fundamentals, Design and Application*, pages 197–228. Elsevier, 2003.

[30] Mohammad A Khaleel and J Robert Selman. Cell, Stack and System Modelling. In K. Singhal, S.C. Kendall, editor, *High Temperature Solid Oxide Fuel Cells: Fundamentals, Design and Application*, pages 292–331. Elsevier, 2003.

[31] Manfred Klell and Raimund Almbauer. *Höhere Thermodynamik*. TU Graz, 2014.

[32] Joon-ho Koh, Young-sung Yoo, Jin-woo Park, and Hee Chun Lim. Carbon deposition and cell performance of Ni-YSZ anode support SOFC with methane fuel. 149:157–166, 2002.

[33] A. Lee, R. Zabransky, and W. Huber. Internal reforming development for Solid Oxide Fuel Cells. *Ind. Eng. Chem. Res.*, 29:766, 1994.

[34] R Leinfelder. Reaktionskinetische Untersuchungen zur Methan-Dampf-Reformierung und Shift-Reaktion an Anoden Oxidkeramischer Brennstoffzellen. *Erlangen-Nurnberg, Germany*, 2004.

[35] Susanne Lux, Daniela Painer, and Matthäus Siebenhofer. Skriptum Reaktionstechnik I, 2013.

[36] Qianli Ma, Jianjun Ma, Sa Zhou, Ruiqiang Yan, Jianfeng Gao, and Guangyao Meng. A high-performance ammonia-fueled SOFC based on a YSZ thin-film electrolyte. *Journal of Power Sources*, 164(1):86–89, 2007.

[37] J. Malzbender and Y. Zhao. Flexural strength and viscosity of glass ceramic sealants for solid oxide fuel cell stacks. *Fuel Cells*, 12(1):47–53, 2011.

[38] Augustin Mcevoy. Anodes. In K. Singhal, S.C. Kendall, editor, *High Temperature Solid Oxide Fuel Cells: Fundamentals, Design and Application*, pages 149–171. Elsevier, 2003.

[39] J. Metzger. *Untersuchung der Stoffumsätze an mit Methan betriebenen Festelektrolyt-Brennstoffzellen*. PhD thesis, Erlangen, 1998.

[40] Nguyen Q Minh. Ceramic Fuel Cells. *Journal of the American Ceramic Society*, 76(3):563–588, 1993.

[41] Nguyen Q Minh and Takehiko Takahashi. *Science and Technology of Ceramic Fuel Cells*. Elsevier Science, 1995.

[42] Erwin Müller-Erlwein. *Chemische Reaktionstechnik*. Springer Spektrum, 3rd edition, 2015.

[43] P. Münster and H. J. Grabke. Kinetics of the steam reforming of methane with iron, nickel, and iron-nickel alloys as catalysts. *Journal of Catalysis*, 72(2):279–287, 1981.

[44] Pedro Nehter. A high fuel utilizing solid oxide fuel cell cycle with regard to the formation of nickel oxide and power density. *Journal of Power Sources*, 164(1):252–259, 2007.

[45] Omega. "Thermoelemente - Einführung zum Thema Temperaturmessung". `http://www.omega.de/prodinfo/thermoelemente.html`. Accessed: 2017-01-30.

[46] R. Mark Ormerod. Fuels and Fuel Processing. In K. Singhal, S.C. Kendall, editor, *High Temperature Solid Oxide Fuel Cells: Fundamentals, Design and Application*, pages 333–361. Elsevier, 2003.

[47] GUSTAVO ADOLFO ORTIGOZA VILLALBA. *DESIGN & DEVELOPMENT OF PLANAR SOLID OXIDE FUEL CELL STACK*. PhD thesis, POLITECNICO DI TORINO, 2013.

[48] Seungdoo Park, Radu Craciun, John M. Vohs, and Raymond J. Gorte. Direct Oxidation of Hydrocarbons in a Solid Oxide Fuel Cell: I. Methane Oxidation. *Journal of The Electrochemical Society*, 146(10):3603–3605, 1999.

[49] J Parsons and S. Randall. Experimental Determination of Kinetic Rate Data for SOFC Anodes. In *SOFC Mocromodelling IEA-SOFC-Task Rep.*, pages 43–46, Berne, 1992.

[50] Murat Peksen. Numerical thermomechanical modelling of solid oxide fuel cells. *Progress in Energy and Combustion Science*, 48:1–20, 2015.

[51] Fabian Rasinger. Design eines Messapparates für SOFC-Einzelzellen und Feststellung der Temperaturverteilung mittels CFD-Simulationen, 2014.

[52] Jens R Rostrup-Nielsen and L. J. Christiansen. Internal steam reforming in fuel cells and alkali poisoning. *Applied Catalysis A: General*, 126(2):381–390, 1995.

[53] Daniel Schaffer. CFD-Simulation einer segmentierten SOFC-Einzelzelle, 2016.

[54] C. Schluckner, V. Subotic, V. Lawlor, and C. Hochenauer. Three-dimensional numerical and experimental investigation of an industrial-sized SOFC fueled by diesel reformat - Part I: Creation of a base model for further carbon deposition modeling. *International Journal of Hydrogen Energy*, 39(33):19102–19118, 2014.

[55] C. Schluckner, V. Subotic, V. Lawlor, and C. Hochenauer. Three-dimensional numerical and experimental investigation of an industrial-sized SOFC fueled by diesel reformat - Part II: Detailed reforming chemistry and carbon deposition analysis. *International Journal of Hydrogen Energy*, 40(34):10943–10959, 2015.

[56] S.C. Singhal and K. Kendall. Introduction to SOFCs. In K. Singhal, S.C. Kendall, editor, *High-temperature Solid Oxide Fuel Cells: Fundamentals, Design and Applications*, pages 1–22. Elsevier, 2003.

[57] Vanja Subotić, Christoph Schluckner, and Christoph Hochenauer. An experimental and numerical study of performance of large planar ESC-SOFCs and experimental investigation of carbon depositions. *Journal of the Energy Institute*, 89(1):121–137, 2016.

[58] Vanja Subotić, Christoph Schluckner, Jörg Mathe, Jürgen Rechberger, Hartmuth Schroettner, and Christoph Hochenauer. Anode regeneration following carbon depositions in an industrial-sized anode supported solid oxide fuel cell operating on synthetic diesel reformate. *Journal of Power Sources*, 295(x):55–66, 2015.

[59] Cell Technology. European PROSOFC project aims to boost SOFC stack reliability. *Fuel Cells Bulletin*, 2013(9):10–11, 2013.

[60] K Wang, D Hissel, M. C. Péra, N Steiner, D Marra, M Sorrentino, C Pianese, M Monteverde, P Cardone, and J Saarinen. A Review on solid oxide fuel cell models, 2011.

[61] Gerd Wedler. *Lehrbuch der Physikalischen Chemie*. 5th edition, 2004.

[62] Wolfgang Winkler. *Brennstoffzellenanlagen*. Springer-Verlag Berlin Heidelberg, 1 edition, 2002.

[63] Wolfgang Winkler. Thermodynamics. In K. Singhal, S.C. Kendall, editor, *High Temperature Solid Oxide Fuel Cells: Fundamentals, Design and Application*, pages 53–82. Elsevier, 2003.

[64] J G Xu and G F Froment. Methane Steam Reforming, Methanation and Water-Gas Shift .1. Intrinsic Kinetics. *Aiche Journal*, 35(1):88–96, 1989.

[65] Harumi Yokokawa and Teruhisa Horita. Cathodes. In K. Singhal, S.C. Kendall, editor, *High Temperature Solid Oxide Fuel Cells: Fundamentals, Design and Application*, pages 119–147. Elsevier, 2003.

A Appendix

A.1 Used Fire Settings

Boundary Conditions for Gases

Table 17: Nonelectric boundary conditions used in the model.

Boundary Condition:	**Description:**
INLET_AIR	Surface representing the Fuel Gas entering the System
OUTLET_AIR	Surface representing the Fuel Gas leaving the System
INLET_FUEL	Surface representing the Cathode Air entering the System
OUTLET_FUEL	Surface representing the Cathode Air leaving the System

Table 18: Boundary definition for the fuel-inlet-surface

Boundary Definition		**Specification Types**		**Used Parameters**		
Sel. f. BC:	INLET_FUEL	Inlet/Outlet:	Mass Flow	$\dot{m}$:	159.987	$[\frac{g}{h}]$
Name of BC:	INLET_FUEL	BC species	Mole Fract.	table		
Type of BC:	Inlet/Outlet					
Activate Flow Dir.:	NO					

Table 19: Boundary definition for Phase 1 of the fuel inlet surface

Settings for Phase 1				
Fixed Temperature	YES	Temp.:	700	[°C]
Fixed Scalar	YES	Scalar	0	-
Fixed Vol.-Fract.	YES	Vol.-Fract.	1	-
Fixed Turbulence	YES	Turb. ref. velocity	0	$[\frac{m}{s}]$
		% of mean velocity	0	-
		% of hydr. diameter	0	-
		Turb. kin. energy	0.001	$[\frac{m^2}{s^2}]$
		Turb. length scale	0	[m]
		Turb. diss. rate	1	$[\frac{m^2}{s^3}]$

Table 20: Boundary definition for the fuel outlet surface

Boundary Definition		**Specification Types**		**Used Parameters**		
Sel. f. BC:	OUTLET_FUEL	Inlet/Outlet:	Static Pressure	p:	101325	[Pa]
Name of BC:	OUTLET_FUEL	BC species	Mole Fract.	table		
Type of BC:	Inlet/Outlet					
Activate Flow Dir.:	NO					

Electric Boundary Conditions

Table 21: Electric boundary conditions used in the model

Boundary Condition:	**Description:**
Cat_Elec_Out	Interface between the cathodes of the fuel cell and the contacting gold mesh. Used to set the current drawn out ouf the fuel cell.
Ano_Elec_Out	Bottom surface (excluding the heaters 1-4) of the model. Used to set the reference potential.

Table 22: Boundary definition for the Cathode Interconnect

Boundary Definition		**Specification Types**		**Used Parameters**		
Sel. f. BC:	Cat_Elec_Out	Movement:	Velocity	u:	0	$[\frac{m}{s}]$
Name of BC:	Cat_Elec_Out			v:	0	$[\frac{m}{s}]$
				w:	0	$[\frac{m}{s}]$
		Thermal:	Conv./Radiat.	α:	1056	$[\frac{W}{m^2 \cdot K}]$
		Convection:	YES	T_{env}:	700	[°C]
		Radiation:	NO	WTR:	0	$[\frac{m^2 \cdot K}{W}]$
		Electric:	Current	(see A.3)		
				CR:	0	$[\frac{V \cdot m^2}{A}]$
		Roughness:	No			
		Slipwall:	No			

Table 23: Boundary definition for the Anode Interconnect

Boundary Definition		**Specification Types**		**Used Parameters**		
Sel. f. BC:	Ano_Elec_Out	Movement:	Velocity	u:	0	$[\frac{m}{s}]$
Name of BC:	Ano_Elec_Out			v:	0	$[\frac{m}{s}]$
				w:	0	$[\frac{m}{s}]$
		Thermal:	Conv./Radiat.	α:	68.571	$[\frac{W}{m^2 \cdot K}]$
		Convection:	YES	T_{env}:	700	[°C]
		Radiation:	NO	WTR:	0	$[\frac{m^2 \cdot K}{W}]$
		Electric:	Current	0		
				CR:	0	$[\frac{V \cdot m^2}{A}]$
		Roughness:	No			
		Slipwall:	No			

Non-Electric Boundary Conditions

Following boundary conditions were used to set the conditions on the surface of the model:

Table 24: Non-electric boundary conditions used in the model

Boundary Condition:	**Description:**
TGIVEN_CROFER	Exterior surface of all Crofer parts
TGIVEN_CERAMIC	Exterior surface of all ceramic parts
TGIVEN_top	Visible surface on the top of the Ceramic-Stamps
TGIVEN_WEIGHT_VSTAMP	Vertical surface of the metal stamp
TGIVEN_WEIGHT_VFrame	Vertical surface of the metal frame
TGIVEN_STAMPS_H	Horizontal surface of the metal stamps
TGIVEN_Frame_H	Horizontal surface of the metal frame
Heater_1 to Heater_4	Four circular surface selections at the bottom of the model

Table 25: Boundary conditions for non-electric solid surfaces at the example of the exterior surface of the crofer-parts

Boundary Definition		**Specification Types**		**Used Parameters**		
Sel. f. BC:	TGIVEN_CROFER	Movement:	Velocity	u:	0	$[\frac{m}{s}]$
				v:	0	$[\frac{m}{s}]$
				w:	0	$[\frac{m}{s}]$
Name of BC:	TGIVEN_CROFER	Thermal:	Temperature	Temp.:	700	[°C]
Type of BC:	Wall	Electric:	Field	Field:	0	$[\frac{V}{m}]$
				CR:	0	$[\frac{V \cdot m^2}{A}]$
		Roughness:	No			
		Slipwall:	No			

Initial Conditions

Solver Control

Table 26: Solver control - Active Equations

Active Equations	
Momentum and Continuity	YES
Volume fraction	YES
Turbulence	Laminar
Energy	YES
	Total Enthalpy
Viscous heating	YES
Pressure Work	YES
Scalar	NO
Two stage pressure correction	NO
Compressibility	Weakly Compressible
Wall Treatment	Hybrid Wall treatment
Heat Transfer Wall Model	Standard Wall Function

Table 28: Linear solver settings

Linear Solver Type		Min iteration	Max iteration	Tolerance
Momentum	GSTB	0	50	0.1
Continuity	AMG	0	5000	0.005
Turbulence	GSTB	0	50	0.1
Energy	GSTB	0	50	0.1
Scalar	GSTB	0	50	0.1
Volume Fraction	GSTB	0	50	0.1
Electric Potential	AMG	0	50	0.1

Table 27: Differencing Scheme

		Blending factor (ignored if upwind)
Momentum	MINIMOD Relaxed	0.5
Continuity	Central Differencing	1
Turbulence	Upwind	0
Energy	Upwind	0
Scalar	Upwind	0
Volume-Fraction	Upwind	0

Table 29: Convergence Criteria

Iteration Limits		
Max. nr. Iterations	10000	
Min. nr. iterations	3	
Normalized Residuals	YES	
Criterion	Used?	Set Value
Pressure	YES	1e-006
Momentum	YES	1e-006
Turb. kin. energy	NO	0.0001
Turb. diss. rate	NO	0.0001
Energy	YES	1e-006
Scalar	NO	5e-008
Volume fraction	NO	0.0001
Electric potential	YES	1e-006

Module Porosities

Table 30: Overview of the set porosities in the model

Definition:	**Description:**
Material_cathode	Definition of the cathode as porous material.
Material_anode	Definition of the anode as porous material.
Material_nickel	Definition of the nickel-net as porous material.
Material_gold	Definition of the gold-net as porous material.
contact_ano_nickel	Modelling the boundary between anode and nickel mesh as porosity to implement a contact resistance.
contact_ano_gold	Modelling the boundary between cathode and gold mesh as porosity to implement a contact resistance.

Table 31: Porosity settings at the example of the cathode material

Porosity Definition		**Used parameters**		**Unit**
Selection:	Material_cathode	Volume Fraction	0.3	-
Name:	Material_cathode	Hydraulic diameter	0.001	m
Mesh requirements fulfilled	YES	Rel. turb. lenght scale	0.01	
Porosity type	Undirected Porosity		1	
	Turbulence fixed	YES	1	
	Pressure-drop model	Forchheimer		
		Zeta_x	0	$\frac{1}{m}$
		Zeta_y	0	$\frac{1}{m}$
		Zety_z	0	$\frac{1}{m}$
		Alpha_x	1e+013	$\frac{1}{m^2}$
		Alpha_y	1e+013	$\frac{1}{m^2}$
		Alpha_z	1e+013	$\frac{1}{m^2}$
		Relative Permeability-model	Muskat/Meres	
			Saturation exp.	6
	Heat exchanger	OFF		
	Turtosity model	Constant		
		Turtosity	5	-
	Knudsen diffusion	OFF		

Table 32: Contact porosity at the example of the surface between anode and nickel

Porosity Definition		**Used parameters**		**Unit**
Selection:	contact_ano_nickel	Volume Fraction	1	-
Name:	contact_ano_nickel	Hydraulic diameter	0.001	m
		Porosity thickness	0.001	m
		0	m^2K/W	
		Electric contact resistance	1e-006	$\frac{V \cdot m^2}{A}$
	Turbulence fixed	NO		
	Pressure drop model	Forhchheimer		
		Superficial velocity	YES	
		Zeta value	100	$\frac{1}{m}$
		Alpha value	0	$\frac{1}{m^2}$
		Relative Permeability-model	Muskat/Meres	
			Saturation exponent	3
	Heat exchanger	OFF		
	Turtosity Model	Constant		
		Turtosity	1	
	Knudsen diffusion	OFF		

Module Fuel-Cell

Table 33: Fuel cell gobal settings

Global Settings		
Cell Type	SOFC	
Definition of Regions		
Electrolyte	Material_electrolyte	
	Positive (Cathode)	Negative (Anode)
Channel	air	fuel
Channel Inlet	INLET_AIR	INLET_FUEL
Channel Outlet	OUTLET_AIR	OUTLET_FUEL
Electrode	Material_cathode_and_gold	Material_anode_and_nickel
Electric inlet/outlet	Cat_Elec_Out	Ano_Elec_Out
Interconnect	Material_interconnect_cat	Material_interconnect_ano

Table 34: Settings for the chemical reactions of the fuel cell

Equation	Parameter	Value	Unit
Watergas-shift reaction	ON		
	Pre-exponential factor a	1.18123	$\frac{m^3}{mol \cdot s \cdot K^b}$
	Temperature exponent b	2	-
	Activation energy	103191	103191
	Equilibrium coefficient	Formula	
Reforming reaction	ON		
	Equation setting n	1	-
	Equation setting m	4	-
	Equation setting p	0	-
	Pre-exponential factor a	48971.8	
	Temperature exponent b	0	
	Activation energy	31776.93	
	Equilibrium coefficient	Formula	

Table 35: Fuel-Cell: Exemplary electrochemistry settings

	Positive (Cathode)	Negative (Anode)
Cathodic transfer coefficient	0.4	0.5
Anodic transfer coefficient	0.5	0.4
Exchange current density	12000	60000
Oxigen exponent	0.25	-
Hydrogen exponent	-	1
Water exponent	-	1
Reference temperature	800	800
Activation energy	120000	120000

A.2 Material Data

Table 36: Material parameters for porosity ϵ [53]

Material	**Value or Formula for ϵ**
Anode:	$\epsilon_{Ni-YSZ} = 0.4$
Cathode:	$\epsilon_{LSM} = 0.3$
Gold-Nets:	$\epsilon_{GN} = 0.75$
Nickel-Nets:	$\epsilon_{NN} = 0.626$

Table 37: Material parameters for turtosity τ [53]

Material	**Value or Formula for τ**
Anode:	$\tau_{Ni-YSZ} = 5$
Cathode:	$\tau_{LSM} = 5$
Gold-Nets:	$\tau_{GN} = 2.5$
Nickel-Nets:	$\tau_{NN} = 2.5$

Table 38: Material parameters for thermal conductivity λ [53]

Material	**Value or Formula for** $\lambda\,[W/(m\cdot K)]$
Anode:	$\lambda_{Ni-YSZ} = 2$
Electrolyte:	$\lambda_{YSZ} = 2.27430 - 1.79104\cdot 10^{-4}\cdot T$
Cathode:	$\lambda_{LSM} = 2$
Gold:	$\lambda_{GN} = 310$
Nickel:	$\lambda_{Ni} = 85$
Crofer:	$\lambda_{Crofer} = 23\cdot(1 - 2.53623\cdot 10^{-4}\cdot(T-673.15) + 9.05797\cdot 10^{-7}\cdot(T-673.15)^2)$
Ceramic:	$\lambda_{Ceramic} = 31.9\cdot(1-0.00229)\cdot(T-293.15) + 1.66666\cdot(T-293.15)^2$
Glass-Solder:	$\lambda_{GL} = 1$

Table 39: Material parameters for the specific heat capacity c [53]

Material	**Value or Formula for** $c\,[J/(kg\cdot K)]$
Anode:	$c_{Ni-YSZ} = 470$
Electrolyte:	$c_{YSZ} = 471$
Cathode:	$c_{LSM} = 470$
Gold:	$c_{GN} = 130$
Nickel:	$c_{Ni} = 444$
Crofer:	$c_{Crofer} = 610\cdot(1 + 3.96175\cdot 10^{-4}(T-673.15) - 4.78142\cdot 10^{-7}\cdot(T-673.15)^2$
Ceramic:	$c_{Ceramic} = 780$
Glass-Solder:	$c_{GL} = 800$

Table 40: Material parameters for electrical conductivity σ [53]

Material	**Value or Formula for** $\sigma\,[\Omega^{-}1 \cdot m^{-}1]$
Anode:	$\sigma_{Ni-YSZ}(T) = \frac{9.5 \cdot 10^7}{T} \cdot exp\left(-\frac{1150}{T}\right)$
Elektrolyt:	$\sigma_{YSZ}(T) = \frac{100}{0.3685 + 0.002838 \cdot exp(\frac{10300}{T})}$
Cathodes:	$\sigma_{LSM}(T) = \frac{4.72 \cdot 10^7}{T} \cdot exp(-\frac{1220}{T})$
Gold:	$\sigma_{Au}(T) = \frac{10^8}{7.96 \cdot \left(1 + 1.38461 \cdot 10^{-3} \cdot (T - 865) + 6.78743 \cdot (T - 865)^2\right)}$
Nickel:	$\sigma_{Ni}(T) = \frac{1}{7 \cdot 10^{-8} \cdot (1 + 6 \cdot 10^{-3} \cdot (T - 293.15))}$
Crofer:	$\sigma_{Crofer}(T) = \frac{10^7}{10.5 \cdot \left(1 + 3.96825 \cdot 10^{-4} \cdot (T - 873.15) + 3.97 \cdot 10^{-7} \cdot (T - 873.15)^2\right)}$

Table 41: Material parameters for porosity ϵ [53]

Material	**Value or Formula for** ϵ
Anode:	$\epsilon_{Ni-YSZ} = 0.4$
Cathode:	$\epsilon_{LSM} = 0.3$
Gold-Nets:	$\epsilon_{GN} = 0.75$
Nickel-Nets:	$\epsilon_{NN} = 0.626$

Table 42: Material parameters for thermal conductivity λ [53]

Material	**Value or Formula for** $\lambda\,[W/(m\cdot K)]$
Anode:	$\lambda_{Ni-YSZ} = 2$
Electrolyte:	$\lambda_{YSZ} = 2.27430 - 1.79104\cdot 10^{-4}\cdot T$
Cathode:	$\lambda_{LSM} = 2$
Gold:	$\lambda_{GN} = 310$
Nickel:	$\lambda_{Ni} = 85$
Crofer:	$\lambda_{Crofer} = 23\cdot(1 - 2.53623\cdot 10^{-4}\cdot(T - 673.15) + 9.05797\cdot 10^{-7}\cdot(T - 673.15)^2)$
Ceramic:	$\lambda_{Ceramic} = 31.9\cdot(1 - 0.00229)\cdot(T - 293.15) + 1.66666\cdot(T - 293.15)^2$
Glass-Solder:	$\lambda_{GL} = 1$

Table 43: Material parameters for the specific heat capacity c [53]

Material	**Value or Formula for** $c\,[J/(kg\cdot K)]$
Anode:	$c_{Ni-YSZ} = 470$
Electrolyte:	$c_{YSZ} = 471$
Cathode:	$c_{LSM} = 470$
Gold:	$c_{GN} = 130$
Nickel:	$c_{Ni} = 444$
Crofer:	$c_{Crofer} = 610\cdot(1 + 3.96175\cdot 10^{-4}(T - 673.15) - 4.78142\cdot 10^{-7}\cdot(T - 673.15)^2$
Ceramic:	$c_{Ceramic} = 780$
Glass-Solder:	$c_{GL} = 800$

Table 44: Material parameters for electrical conductivity σ [53]

Material	**Value or Formula for** $\sigma\,[\Omega^{-}1 \cdot m^{-}1]$
Anode:	$\sigma_{Ni-YSZ}(T) = \frac{9.5 \cdot 10^7}{T} \cdot exp\left(-\frac{1150}{T}\right)$
Elektrolyt:	$\sigma_{YSZ}(T) = \frac{100}{0.3685 + 0.002838 \cdot exp(\frac{10300}{T})}$
Cathodes:	$\sigma_{LSM}(T) = \frac{4.72 \cdot 10^7}{T} \cdot exp(-\frac{1220}{T})$
Gold:	$\sigma_{Au}(T) = \frac{10^8}{7.96 \cdot \left(1 + 1.38461 \cdot 10^{-3} \cdot (T - 865) + 6.78743 \cdot (T - 865)^2\right)}$
Nickel:	$\sigma_{Ni}(T) = \frac{1}{7 \cdot 10^{-8} \cdot (1 + 6 \cdot 10^{-3} \cdot (T - 293.15))}$
Crofer:	$\sigma_{Crofer}(T) = \frac{10^7}{10.5 \cdot \left(1 + 3.96825 \cdot 10^{-4} \cdot (T - 873.15) + 3.97 \cdot 10^{-7} \cdot (T - 873.15)^2\right)}$

A.3 Geometry CFD-Model

Table 45: Positions in the CFD Model used for postprocessing

Element	Coordinate
Flow field Air	y=-0.00067m
Flow field Fuel	y=-0.0033m
Single Fuel Channel	x=0.0252
Anode Electric Contact	y=-0.0218
Cathode Electric Contact	y=0.05843
Gold-Wires (horizontal)	y=-0.00142
Goldnetze	y=-0.00165
Nickelnetze	y=-0.0023775
Anode	y=-0.001985
Electrolyte	y=-0.0018075
Cathodes	y=-0.001765
Thermocouples	y=-0.0068
Bottom Edge	y=-0.0218m

A.4 Programmed Formulas

Formula: Current

Global Formula Variables (accessible both from Initialization and Body)

```
int matDim;

char mat[1];

void set_mat(char selName[], char matIndex)

{

        int sel[3],idir,ib,ic;

        if(SelInit(selName, sel) && SelType(sel) == 2){

                if(IAMPRO < 2) print "setting formula mat index in selection", selName, "to", (int)
        matIndex;

                while(SelNext(sel)){

                        ic=SelIndex(sel);

                        idir=SelIndex2(sel);

              ib=INDEX_OF_SEL_BND_FACE(ic+1,idir+1)-1;

              mat[ib] = matIndex;

                }

        }else{

                print "ERROR: selection", selName, "does not exist or is not a cell selection!";

        }

}
```

Formula Initialization

```
if(ITER == 0){

        matDim = NBFAC;

        resize(mat, matDim+1);

        mat = 0;

        set_mat("Cat1_Elec_Out", 1);

        set_mat("Cat2_Elec_Out", 2);
```

```
        set_mat("Cat3_Elec_Out", 3);
        set_mat("Cat4_Elec_Out", 4);
}
```

Formula Body

```
double ncat=4.0;
double i1=0.0;
double i2=0.0;
double i3=0.0;
double i4=0.0;
int iterset=100;
if(mat[index] == 1){
    if(ITER>iterset) {
        return -i1*ncat;
}else return -i1/iterset*ncat*ITER;
} else if(mat[index] == 2){
    if(ITER>iterset) {
        return -i2*ncat;
}else return -i2/iterset*ncat*ITER;
} else if(mat[index] == 3){
    if(ITER>iterset) {
        return -i3*ncat;
}else return -i3/iterset*ncat*ITER;
} else if(mat[index] == 4){
    if(ITER>iterset) {
        return -i4*ncat;
}else return -i4/iterset*ncat*ITER;
}
```

A.5 Fuel-Compositions CFD

	t=700°C, i=0mA/cm2		t=700°C, i=168.35mA/cm2	
Ch.	CFD (wet)	CFD (Dry)	CFD (wet)	CFD (Dry)
	H2 (calc, wet)	H2 (calc, dry)	H2 (calc, wet)	H2 (calc, dry)
1	5.486	6.938	5.120	6.484
2	19.179	22.284	18.374	21.573
3	23.126	26.271	21.841	25.214
4	24.651	27.739	22.553	26.002
5	25.087	28.080	22.487	25.974
	CO (calc, wet)	CO (calc, dry)	CO (calc, wet)	CO (calc, dry)
1	0.731	0.924	0.501	0.635
2	4.791	5.567	4.727	5.550
3	5.829	6.622	5.890	6.799
4	6.114	6.880	6.009	6.928
5	6.245	6.990	5.991	6.920
	CH4 (calc, wet)	CH4 (calc, dry)	CH4 (calc, wet)	CH4 (calc, dry)
1	7.462	9.437	7.713	9.767
2	2.385	2.772	2.573	3.021
3	0.885	1.005	0.889	1.027
4	0.363	0.409	0.280	0.323
5	0.116	0.130	0.109	0.126
	CO2 (calc, wet)	CO2 (calc, dry)	CO2 (calc, wet)	CO2 (calc, dry)
1	0.865	1.094	0.857	1.085
2	1.033	1.200	1.036	1.217
3	1.199	1.362	1.295	1.495
4	1.363	1.534	1.490	1.718
5	1.690	1.891	1.728	1.996
	H2O (calc, wet)		H2O (calc, wet)	
1	20.927		21.032	
2	13.934		14.828	
3	11.971		13.378	
4	11.133		13.265	
5	10.658		13.423	

	t=750°C, i=0mA/cm2		t=750°C, i=168.35mA/cm2		t=750°C, i=448.93mA/cm2	
Ch.	CFD (wet)	CFD (Dry)	CFD (wet)	CFD (Dry)	CFD (wet)	CFD (Dry)
	H2 (calc, wet)	H2 (calc, dry)	H2 (calc, wet)	H2 (calc, dry)	H2 (calc, wet)	H2 (calc, dry)
1	10.139	12.491	8.762	10.819	9.211	11.375
2	21.390	24.592	20.031	23.223	18.856	22.117
3	24.179	27.218	22.883	26.170	20.774	24.382
4	25.574	28.565	23.463	26.844	19.975	23.809
5	25.897	28.832	23.278	26.709	18.801	22.747
	CO (calc, wet)	CO (calc, dry)	CO (calc, wet)	CO (calc, dry)	CO (calc, wet)	CO (calc, dry)
1	1.137	1.401	0.743	0.917	0.828	1.023
2	4.616	5.307	4.485	5.200	4.445	5.213
3	5.536	6.232	5.450	6.232	5.271	6.186
4	5.780	6.456	5.611	6.419	5.330	6.352
5	5.841	6.503	5.556	6.375	5.122	6.197
	CH4 (calc, wet)	CH4 (calc, dry)	CH4 (calc, wet)	CH4 (calc, dry)	CH4 (calc, wet)	CH4 (calc, dry)
1	6.731	8.293	6.727	8.306	6.727	8.308
2	2.063	2.372	2.171	2.516	2.140	2.510
3	0.649	0.730	0.721	0.825	0.696	0.817
4	0.235	0.262	0.255	0.292	0.232	0.276
5	0.075	0.084	0.061	0.071	0.046	0.056
	CO2 (calc, wet)	CO2 (calc, dry)	CO2 (calc, wet)	CO2 (calc, dry)	CO2 (calc, wet)	CO2 (calc, dry)
1	1.327	1.635	1.327	1.639	1.329	1.641
2	1.510	1.736	1.554	1.802	1.611	1.890
3	1.660	1.869	1.780	2.036	1.941	2.278
4	1.797	2.007	1.986	2.272	2.327	2.774
5	1.961	2.183	2.229	2.557	2.692	3.257
	H2O (calc, wet)		H2O (calc, wet)		H2O (calc, wet)	
1	18.836		19.012		19.024	
2	13.021		13.745		14.746	
3	11.165		12.562		14.798	
4	10.471		12.595		16.103	
5	10.177		12.848		17.348	

	t=800°C, i=0mA/cm2		t=800°C, i=168.35mA/cm2		t=800°C, i=448.93mA/cm2	
	CFD (wet)	CFD (Dry)	CFD (wet)	CFD (Dry)	CFD (wet)	CFD (Dry)
Ch.	H2 (calc, wet)	H2 (calc, dry)	H2 (calc, wet)	H2 (calc, dry)	H2 (calc, wet)	H2 (calc, dry)
1	10.367	12.677	9.838	12.107	10.081	12.398
2	21.830	25.019	21.001	24.244	19.952	23.327
3	25.075	28.182	23.737	27.088	21.574	25.250
4	26.141	29.171	24.084	27.509	20.613	24.521
5	26.314	29.276	23.794	27.275	19.432	23.422
	CO (calc, wet)	CO (calc, dry)	CO (calc, wet)	CO (calc, dry)	CO (calc, wet)	CO (calc, dry)
1	1.384	1.692	1.007	1.239	1.002	1.232
2	4.713	5.401	4.582	5.290	4.538	5.306
3	5.555	6.244	5.396	6.158	5.212	6.100
4	5.749	6.415	5.528	6.314	5.170	6.151
5	5.806	6.459	5.462	6.261	4.905	5.912
	CH4 (calc, wet)	CH4 (calc, dry)	CH4 (calc, wet)	CH4 (calc, dry)	CH4 (calc, wet)	CH4 (calc, dry)
1	6.345	7.759	6.478	7.972	6.447	7.929
2	1.797	2.059	1.844	2.128	1.833	2.143
3	0.587	0.660	0.593	0.677	0.569	0.667
4	0.187	0.208	0.179	0.205	0.182	0.216
5	0.049	0.054	0.043	0.049	0.027	0.032
	CO2 (calc, wet)	CO2 (calc, dry)	CO2 (calc, wet)	CO2 (calc, dry)	CO2 (calc, wet)	CO2 (calc, dry)
1	1.237	1.513	1.233	1.518	1.244	1.530
2	1.508	1.728	1.558	1.799	1.653	1.933
3	1.674	1.881	1.800	2.054	2.034	2.381
4	1.790	1.997	2.029	2.317	2.364	2.812
5	1.936	2.154	2.208	2.531	2.830	3.411
	H2O (calc, wet)		H2O (calc, wet)		H2O (calc, wet)	
1	18.223		18.738		18.690	
2	12.744		13.376		14.466	
3	11.026		12.368		14.558	
4	10.389		12.452		15.938	
5	10.120		12.761		17.032	

A.6 Measured Fuel Compositions

		CH4_800_Degr: Mittelwerte über Messdauer				
		Channel 1	Channel 2	Channel 3	Channel 4	Channel 5
0A	O2_0A	2.651201235	2.691537429	2.711268928	2.724234669	2.724877549
	H2_0A	5.729860494	19.2032662	25.6440353	29.85150632	32.14286823
	CO_0A	0.289995062	2.61680776	4.159787847	5.337601896	6.021241235
	CH4_0A	10.13650741	4.955029508	2.543018259	1.132305969	0.518821132
	CO2_0A	1.093603704	2.389315354	2.711295642	2.734774995	2.648920355
	N2_0A	x	x	x	x	x
	H2O_0A	x	x	x	x	x
1A	O2_1A	2.65144485	2.687869149	2.708037205	2.719961745	2.72069202
	H2_1A	6.295094352	19.10239199	25.10104182	29.07118668	31.28303487
	CO_1A	0.364062458	2.597303581	4.040133064	5.143554426	5.847747451
	CH4_1A	9.889387375	4.853475737	2.502339576	1.135893079	0.468902426
	CO2_1A	1.172177741	2.470258396	2.869537373	2.963523791	2.918244244
	N2_1A	x	x	x	x	x
	H2O_1A	x	x	x	x	x
2A	O2_2A	2.651237313	2.68867548	2.707068932	2.718310843	2.718846043
	H2_2A	6.317969652	18.93959481	24.76590708	28.48516813	30.57906253
	CO_2A	0.374762687	2.567266356	3.954619829	4.986669988	5.665939606
	CH4_2A	9.7958199	4.823916754	2.481299032	1.131341572	0.460414353
	CO2_2A	1.199464179	2.554609222	3.042090469	3.195944791	3.142584802
	N2_2A	x	x	x	x	x
	H2O_2A	x	x	x	x	x
3A	O2_3A	2.652973626	2.68905098	2.705858975	2.716918909	2.717963445
	H2_3A	6.432589011	18.6930049	24.26424961	27.86309043	30.11320697
	CO_3A	0.385391209	2.525802941	3.843260826	4.838092783	5.537927927
	CH4_3A	9.729401099	4.804176471	2.477188332	1.113579822	0.454370989
	CO2_3A	1.207816484	2.625013725	3.190416901	3.411035678	3.354214583
	N2_3A	x	x	x	x	x
	H2O_3A	x	x	x	x	x
4A	O2_4A	2.652756972	2.688783013	5.182765758	2.715418317	2.716441679
	H2_4A	6.178905976	18.18397891	23.46700062	26.93037327	29.353166
	CO_4A	0.373359761	2.437611422	3.675669753	4.624579703	5.353349863
	CH4_4A	9.613162948	4.771482635	2.46965679	1.118272277	0.451620945
	CO2_4A	1.199854183	2.658210374	3.30417716	3.600209406	3.547306212
	N2_4A	x	x	x	x	x
	H2O_4A	x	x	x	x	x

		CH4_750_Degr: Mittelwerte über Messdauer				
		Channel 1	Channel 2	Channel 3	Channel 4	Channel 5
0A	O2_0A	2.639875248	2.677057346	2.696208416	2.708410117	2.717748398
	H2_0A	10.06762475	22.36011835	27.95409059	31.09297827	32.55426235
	CO_0A	0.91019802	3.800852536	5.427334158	6.448048528	6.975363429
	CH4_0A	8.482637624	3.650584831	1.603218812	0.603912724	0.193006564
	CO2_0A	1.650638614	2.358913073	2.446626733	2.365624956	2.265571067
	N2_0A	x	x	x	x	x
	H2O_0A	x	x	x	x	x
1A	O2_1A	2.639756436	2.675359155	2.692729895	2.702211698	2.702781387
	H2_1A	10.13506139	22.1649831	27.59103977	30.63718204	32.04577485
	CO_1A	0.913116832	3.733423631	5.32403412	6.31495159	6.849923117
	CH4_1A	8.534839604	3.701361972	1.633712814	0.613538644	0.192577122
	CO2_1A	1.657086139	2.430916901	2.606277962	2.591146037	2.476649046
	N2_1A	x	x	x	x	x
	H2O_1A	x	x	x	x	x
2A	O2_2A	2.64002439	2.67524089	2.691824932	2.69973345	2.700729626
	H2_2A	10.2136561	22.02188556	27.18519704	30.0752879	31.49307013
	CO_2A	0.921890244	3.712497202	5.216694949	6.166397689	6.69816463
	CH4_2A	8.560426829	3.723061286	1.659247461	0.62485772	0.193265397
	CO2_2A	1.660809756	2.495776064	2.758320588	2.807991034	2.729592275
	N2_2A	x	x	x	x	x
	H2O_2A	x	x	x	x	x
3A	O2_3A	2.64045082	2.67457992	2.690172821	2.698877399	2.698174614
	H2_3A	9.956596721	21.44593315	26.3346068	29.16895341	30.1398547
	CO_3A	0.894913115	3.599482099	5.037639701	5.977697443	6.378063437
	CH4_3A	8.495645902	3.723859731	1.673092696	0.628560673	0.194128921
	CO2_3A	1.655455738	2.542763108	2.892726578	3.014744921	3.157032301
	N2_3A	x	x	x	x	x
	H2O_3A	x	x	x	x	x
5A	O2_5A	2.640448485	2.676640432	2.690850263	2.698272345	2.69756559
	H2_5A	10.20871667	21.18504583	25.59149962	28.03889751	29.2830198
	CO_5A	0.923024242	3.52575863	4.847844732	5.687873481	6.166525821
	CH4_5A	8.5663	3.796010265	1.719616813	0.64920862	0.195753487
	CO2_5A	1.679237879	2.700445738	3.231612131	3.477485867	3.505811263
	N2_5A	x	x	x	x	x
	H2O_5A	x	x	x	x	x
7A	O2_7A	2.644809877	2.676674734	2.689474257	2.695307746	2.695650998
	H2_7A	10.15180247	15.90173502	24.63591238	26.56351387	28.02314211
	CO_7A	0.92695679	3.436794415	4.635437129	5.359031295	5.881294901
	CH4_7A	8.533877778	3.826271158	1.749723762	0.659883877	0.199154889
	CO2_7A	1.696725926	2.837417745	3.543423267	3.944920326	3.923023127
	N2_7A	x	x	x	x	x
	H2O_7A	x	x	x	x	x
8A	O2_8A	2.640411765	2.676955191	2.688900691	2.695046616	2.694702952
	H2_8A	10.19236078	20.45953993	24.07726955	25.88644887	27.22016918
	CO_8A	0.924582353	3.379483866	4.524746522	5.226726741	5.715552809
	CH4_8A	8.556219608	3.842365348	1.76059904	0.653967822	0.242555343
	CO2_8A	1.691168627	2.901038664	3.703992208	4.168430198	4.187225278
	N2_8A	x	x	x	x	x
	H2O_8A	x	x	x	x	x

		CH4_800_Degr: Mittelwerte über Messdauer				
		Channel 1	Channel 2	Channel 3	Channel 4	Channel 5
0A	O2_0A	2.60931782	2.63849303	2.65734645	2.66690183	2.6697755
	H2_0A	11.5557832	22.131555	28.3274217	31.4718583	32.7536099
	CO_0A	1.2273604	3.86734826	5.66233611	6.7280522	7.29977705
	CH4_0A	8.06257525	3.70789055	1.46522991	0.48247977	0.10257118
	CO2_0A	1.52754356	2.38702761	2.42870377	2.10988036	2.00967718
	N2_0A	x	x	x	x	x
	H2O_0A	x	x	x	x	x
1A	O2_1A	2.61104834	2.65382995	2.65678107	2.66630728	2.6683105
	H2_1A	11.7566	21.8591921	27.786012	30.8279358	32.0276346
	CO_1A	1.2608649	3.80276854	5.5295495	6.58301867	7.14221549
	CH4_1A	7.96897285	3.72217715	1.50015877	0.50879656	0.10834942
	CO2_1A	1.54872649	2.41449338	2.4957069	2.20438893	2.22491886
	N2_1A	x	x	x	x	x
	H2O_1A	x	x	x	x	x
2A	O2_2A	2.63347562	2.65720155	2.67305146	2.67919127	2.6777485
	H2_2A	11.8488498	21.4414805	27.276891	30.0972623	31.213073
	CO_2A	1.26096517	3.64146524	5.3516092	6.36315517	6.83534589
	CH4_2A	7.71954826	3.73559995	1.49972963	0.5168773	0.11403213
	CO2_2A	1.55773184	2.44050007	2.55201439	2.45203223	2.43354419
	N2_2A	x	x	x	x	x
	H2O_2A	x	x	x	x	x
3A	O2_3A	2.63163267	2.65719109	2.67349356	2.68168812	2.67731146
	H2_3A	11.9451406	21.3277134	26.9822941	29.4777866	30.430751
	CO_3A	1.30232376	3.63805693	5.31390396	6.24150248	6.80622534
	CH4_3A	7.76690099	3.77428663	1.51158762	0.52217178	0.10061115
	CO2_3A	1.57787129	2.46313267	2.60568663	2.64076337	2.66598172
	N2_3A	x	x	x	x	x
	H2O_3A	x	x	x	x	x
5A	O2_5A	2.63248119	2.65722499	2.67233119	2.67908069	2.66492881
	H2_5A	11.8749861	21.1269755	26.3326149	28.3077005	29.1679974
	CO_5A	1.32354455	3.67161244	5.24938663	6.1049005	6.61835358
	CH4_5A	7.88925248	3.81027814	1.5295203	0.51880644	0.09868819
	CO2_5A	1.61465545	2.51098588	2.71966931	3.03314257	3.08574087
	N2_5A	x	x	x	x	x
	H2O_5A	x	x	x	x	x
7A	O2_7A	2.62689307	2.65245782	2.66629063	2.67137081	2.67417098
	H2_7A	11.8855802	20.8185329	25.5309966	26.9778802	27.7502868
	CO_7A	1.33423168	3.60361452	5.08252751	5.83121631	6.33531269
	CH4_7A	7.92057327	3.84211443	1.56372756	0.513525	0.10335447
	CO2_7A	1.62988812	2.5592416	2.85055152	3.46973089	3.56743391
	N2_7A	x	x	x	x	x
	H2O_7A	x	x	x	x	x
8A	O2_8A	2.62762673	2.65105336	2.66374059	2.66783515	2.67042505
	H2_8A	12.0514752	20.576205	25.0404153	26.0963797	26.9285343
	CO_8A	1.37055446	3.57861681	4.99801238	5.66116188	6.172805
	CH4_8A	7.88726832	3.8607881	1.56681584	0.54309307	0.10888902
	CO2_8A	1.67649307	2.58578175	2.90896287	3.69232327	3.81166669
	N2_8A	x	x	x	x	x
	H2O_8A	x	x	x	x	x
9A	O2_9A	2.62407723	2.6465475	2.66145519	2.66210855	2.66478239
	H2_9A	11.7153356	20.1716574	24.7675129	25.3125581	26.077948
	CO_9A	1.33256436	3.5111214	4.94766882	5.52679783	6.0069383
	CH4_9A	7.77855248	3.85782557	1.57933108	0.54943085	0.1399322
	CO2_9A	1.66988119	2.59875245	2.90759182	3.89605496	3.65541669
	N2_9A	x	x	x	x	x
	H2O_9A	x	x	x	x	x

A.7 Calculated Dry-based Wet Fuel Compositions at OCV

		CH4_700_Degr: Errechnete Zusammensetzung (Atombilanz) (mol% feucht, O2 zu 0 korrigiert)				
		Channel 1	Channel 2	Channel 3	Channel 4	Channel 5
OCV	O2_0A	0	0	0	0	0
	H2_0A	4.515699178	16.30970459	22.60123999	26.93706858	29.35422883
	CO_0A	0.228544912	2.222505333	3.666207847	4.816485532	5.498852553
	CH4_0A	7.988574629	4.208402189	2.241276199	1.021757602	0.473809435
	CO2_0A	0.861868339	2.029291641	2.389586614	2.467775689	2.419106276
	N2_0A	65.21524528	60.16202616	57.23618037	54.99379474	53.57823887
	H2O_0A	21.19006767	15.06807009	11.86550897	9.763117857	8.675764044

		CH4_750_Degr: Errechnete Zusammensetzung (Atombilanz) (mol% feucht, O2 zu 0 korrigiert)				
		Channel 1	Channel 2	Channel 3	Channel 4	Channel 5
OCV	O2_0A	0	0	0	0	0
	H2_0A	8.13327748	19.35080186	24.98519564	28.28403837	29.84449544
	CO_0A	0.735316744	3.289318203	4.850918162	5.865531772	6.394744866
	CH4_0A	6.852822513	3.159274142	1.432947194	0.549355243	0.176940994
	CO2_0A	1.333492477	2.041440871	2.186780048	2.151914378	2.076988404
	N2_0A	63.73154916	58.70075453	55.92354892	54.11515943	53.18298354
	H2O_0A	19.21354162	13.4584104	10.62061003	9.034000807	8.323846761

		CH4_800_Degr: Errechnete Zusammensetzung (Atombilanz) (mol% feucht, O2 zu 0 korrigiert)				
		Channel 1	Channel 2	Channel 3	Channel 4	Channel 5
0A	O2_0A	0	0	0	0	0
	H2_0A	9.374804567	19.16884625	25.40053942	28.59448064	29.99304107
	CO_0A	0.995714758	3.34963378	5.077284943	6.112926556	6.684530769
	CH4_0A	6.540886598	3.211522366	1.313837548	0.43836809	0.093926185
	CO2_0A	1.239242912	2.067480813	2.177762121	1.916980323	1.840295782
	N2_0A	62.97586964	58.81570899	55.69824754	53.79454413	52.95991753
	H2O_0A	18.87348152	13.3868078	10.33232843	9.142700255	8.428288667

A.8 Measured and simulated IV-Curves

	700 °C:					
A/Cell	Current-Density	C1 (meas)	C2 (meas)	C3 (meas)	C4 (meas)	Mean Voltage (meas)
1	56.117	0.965	0.960	0.925	0.930	0.945
2	112.233	0.911	0.893	0.846	0.847	0.874
3	168.350	0.859	0.833	0.777	0.772	0.810
4	224.467	0.811	0.776	0.715	0.703	0.751
5	280.584	0.763	0.721	0.659	0.643	0.697
	Current-Density	C1 (calc)	C2 (calc)	C3 (calc)	C4 (calc)	Mean Voltage (calc)
1	56.117	0.949	0.949	0.936	0.936	0.943
5	280.584	0.711	0.711	0.675	0.676	0.693

	750 °C:					
A/Cell	Current-Density	C1 (meas)	C2 (meas)	C3 (meas)	C4 (meas)	Mean Voltage (meas)
1	56.117	0.970	0.964	0.965	0.958	0.964
2	112.233	0.925	0.920	0.925	0.916	0.922
3	168.350	0.884	0.879	0.885	0.876	0.881
4	224.467	0.844	0.840	0.848	0.840	0.843
5	280.584	0.806	0.803	0.812	0.804	0.806
6	336.700	0.770	0.769	0.776	0.773	0.772
7	392.817	0.736	0.736	0.742	0.743	0.739
8	448.934	0.701	0.704	0.710	0.714	0.707
	Current-Density	C1 (calc)	C2 (calc)	C3 (calc)	C4 (calc)	Mean Voltage (calc)
3	168.350	0.887	0.887	0.878	0.878	0.883
8	448.934	0.712	0.712	0.706	0.706	0.709

	800 °C:					
A/Cell	Current-Density	C1 (meas)	C2 (meas)	C3 (meas)	C4 (meas)	Mean Voltage (meas)
1	56.117	0.970	0.970	0.971	0.970	0.970
2	112.233	0.932	0.941	0.942	0.944	0.940
3	165.350	0.899	0.916	0.917	0.922	0.914
4	224.467	0.860	0.888	0.885	0.895	0.882
5	280.584	0.828	0.863	0.861	0.873	0.856
6	336.700	0.798	0.837	0.837	0.853	0.831
7	392.817	0.767	0.812	0.813	0.831	0.806
8	448.934	0.737	0.789	0.790	0.811	0.782
9	505.051	0.708	0.764	0.768	0.792	0.758
	Current-Density	C1 (calc)	C2 (calc)	C3 (calc)	C4 (calc)	Mean Voltage (calc)
3	168.350	0.909	0.908	0.907	0.907	0.908
8	448.934	0.772	0.772	0.782	0.782	0.777

A.9 Measured and simulated Temperatures

Measured Temperatures (uncorrected) [°C]

	CH4_700D_0A	CH4_700D_3A	CH4_750D_0A	CH4_750D_3A	CH4_750D_8A	CH4_800D_3A	CH4_800D_8A
T_v1	697.26	695.48	750.20	749.32	751.53	798.06	800.53
T_v2	696.20	694.75	749.63	748.63	750.56	797.40	799.37
T_v3	696.45	694.96	749.97	749.00	751.03	797.88	799.86
T_v4	698.58	696.88	751.77	750.97	752.74	800.06	801.56
T_v5	696.79	695.17	749.66	748.89	751.74	797.73	800.91
T_v6	698.36	696.62	751.59	750.71	751.90	799.89	801.23
T_v7	694.03	692.62	746.88	745.84	747.43	794.30	796.47
T_v8	690.95	690.61	745.13	744.24	748.35	792.90	796.37
T_v9	696.39	695.06	749.87	748.89	750.61	798.07	799.79
T_v10	689.93	689.69	743.92	743.03	747.33	791.47	795.09
T_v11	691.16	690.65	745.29	744.30	747.85	793.05	796.07
T_v12	693.26	691.98	746.02	745.04	746.55	793.51	795.64
T_v13	690.34	689.98	744.33	743.40	747.11	792.00	795.32
T_v14	695.67	694.54	749.08	748.17	750.12	797.32	799.13
T_v15	694.14	692.99	746.79	746.13	749.00	794.85	797.15
T_v16	695.56	694.35	748.54	747.96	751.20	797.04	798.68
T_v17	694.61	694.12	747.75	747.36	754.62	795.85	799.97
T_v18	694.38	693.37	747.61	746.57	748.17	795.70	797.83
T_h11	695.02	694.15	748.28	747.07	748.71	795.38	797.70
T_h12	694.23	693.73	747.85	746.63	749.07	794.83	797.89
T_h13	694.37	693.99	748.21	747.08	749.93	796.02	799.38
T_h14	693.77	693.78	748.00	746.61	748.90	795.85	797.94
T_h21	696.17	695.70	750.26	749.19	752.28	798.30	800.55
T_h22	696.62	696.62	751.42	750.90	757.48	799.95	803.52
T_h23	698.33	697.40	752.15	750.89	752.67	800.26	801.89
T_h24	698.66	698.12	753.13	751.84	754.66	801.82	805.42
T_h31	693.40	692.53	746.38	745.21	746.93	793.72	796.08
T_h32	694.12	693.44	747.47	746.25	748.56	794.62	797.49
T_h33	691.32	690.78	744.61	743.65	746.34	791.75	794.90
T_h34	690.38	690.47	744.02	743.17	747.03	791.24	795.01
T_h41	692.05	691.64	745.78	744.93	748.04	793.81	796.93
T_h42	693.07	693.07	747.54	746.64	750.66	795.70	799.17
T_h43	693.77	693.15	747.43	746.58	749.04	795.68	798.15
T_h44	695.00	694.68	749.38	748.40	751.58	797.77	800.60

Measured Temperatures (corrected) [°C]

	CH4_700D_0A	CH4_700D_3A	CH4_750D_0A	CH4_750D_3A	CH4_750D_8A	CH4_800D_3A	CH4_800D_8A
T_v1	696.25	694.46	748.95	748.06	750.27	796.81	799.27
T_v2	695.51	694.06	748.91	747.91	749.84	796.69	798.65
T_v3	696.00	694.50	749.43	748.46	750.49	797.35	799.32
T_v4	697.53	695.83	750.52	749.72	751.49	798.73	800.23
T_v5	696.25	694.63	748.92	748.15	751.00	797.10	800.27
T_v6	697.68	695.94	750.65	749.77	750.96	798.84	800.17
T_v7	694.79	693.37	747.66	746.62	748.21	795.04	797.21
T_v8	691.99	691.66	746.60	745.70	749.81	794.37	797.84
T_v9	696.84	695.51	750.39	749.42	751.14	798.48	800.19
T_v10	691.36	691.12	745.87	744.98	749.28	793.54	797.16
T_v11	693.16	692.66	747.72	746.73	750.29	795.57	798.59
T_v12	695.32	694.04	748.16	747.18	748.69	795.70	797.83
T_v13	692.50	692.14	746.97	746.04	749.76	794.77	798.09
T_v14	696.80	695.67	750.36	749.45	751.40	798.56	800.37
T_v15	696.59	695.43	749.18	748.52	751.39	797.26	799.56
T_v16	697.75	696.54	750.75	750.17	753.41	799.19	800.83
T_v17	696.18	695.70	749.02	748.63	755.89	797.33	801.44
T_v18	696.57	695.55	749.51	748.48	750.08	797.74	799.87
T_h11	693.51	692.63	746.28	745.07	746.72	793.60	795.92
T_h12	691.46	690.97	744.54	743.32	745.76	791.44	794.51
T_h13	692.56	692.18	746.01	744.88	747.74	794.00	797.36
T_h14	691.08	691.09	744.86	743.48	745.77	792.59	794.67
T_h21	694.63	694.15	748.42	747.35	750.44	796.63	798.87
T_h22	693.27	693.27	747.57	747.06	753.64	795.87	799.44
T_h23	696.39	695.46	749.66	748.41	750.18	797.85	799.48
T_h24	695.29	694.75	749.14	747.84	750.66	797.52	801.12
T_h31	694.04	693.17	746.60	745.44	747.15	794.03	796.39
T_h32	692.43	691.75	745.20	743.98	746.29	792.16	795.03
T_h33	693.54	693.00	747.53	746.57	749.26	794.85	798.01
T_h34	690.81	690.90	745.35	744.51	748.37	792.56	796.32
T_h41	694.10	693.70	748.65	747.80	750.91	796.77	799.89
T_h42	692.51	692.51	747.68	746.78	750.80	795.69	799.17
T_h43	695.46	694.84	749.78	748.93	751.38	797.99	800.47
T_h44	694.22	693.90	749.10	748.12	751.29	797.19	800.01

Temperature data CFD-Simulations [°C]

	CH4_700D_0A	CH4_700D_3A	CH4_750D_0A	CH4_750D_3A	CH4_750D_8A	CH4_800D_0A	CH4_800D_3A	CH4_800D_8A
T_v1	698.06	698.41	748.58	748.60	748.70	798.68	798.72	798.78
T_v2	698.91	699.10	749.12	749.11	749.43	799.29	799.33	799.53
T_v3	699.29	699.42	749.40	749.44	749.73	799.57	799.67	799.82
T_v4	699.69	699.71	749.75	749.80	749.92	799.85	799.88	799.96
T_v5	697.75	697.92	748.00	748.15	748.24	798.49	798.50	798.47
T_v6	699.73	699.76	749.77	749.81	749.93	799.87	799.90	799.98
T_v7	695.15	695.79	746.00	746.07	746.23	796.70	796.75	796.87
T_v8	697.94	698.28	747.51	747.87	748.93	798.20	798.41	799.09
T_v9	699.78	699.80	749.66	749.75	750.00	799.81	799.88	800.04
T_v10	697.13	697.50	746.89	747.24	748.22	797.57	797.76	798.45
T_v11	698.51	698.83	748.11	748.55	749.54	798.70	798.95	799.71
T_v12	695.75	695.85	745.99	746.06	746.23	796.69	796.73	796.86
T_v13	697.87	698.22	747.52	747.87	748.92	798.13	798.41	799.10
T_v14	699.77	699.80	749.66	749.75	750.00	799.82	799.88	800.05
T_v15	697.99	698.00	748.12	748.15	748.24	798.38	798.40	798.47
T_v16	699.74	699.76	749.78	749.81	749.94	799.87	799.90	799.97
T_v17	699.10	699.17	749.10	749.11	749.37	799.26	799.33	799.58
T_v18	699.38	699.46	749.40	749.43	749.72	799.61	799.65	799.83
T_h11	694.46	694.72	744.79	745.09	745.65	795.24	795.35	795.88
T_h12	693.42	693.75	743.63	743.90	744.74	794.36	794.59	795.16
T_h13	697.15	697.35	747.11	747.39	748.12	797.37	797.64	798.27
T_h14	696.66	696.92	746.33	746.77	747.69	796.82	797.11	797.92
T_h21	699.09	699.35	748.97	749.27	750.01	799.16	799.42	800.06
T_h22	699.00	699.34	748.67	749.07	750.01	799.02	799.33	800.06
T_h23	699.60	699.80	749.47	749.70	750.33	799.61	799.82	800.34
T_h24	699.61	699.82	749.35	749.63	750.42	799.51	799.78	800.40
T_h31	694.91	695.13	744.92	744.97	745.57	795.11	795.23	795.91
T_h32	693.61	693.94	743.80	743.86	744.72	794.22	794.43	795.17
T_h33	697.34	697.56	747.15	747.30	748.12	797.38	797.67	798.29
T_h34	696.66	696.94	746.35	746.75	747.67	796.83	797.11	797.93
T_h41	699.14	699.41	748.96	749.26	750.02	799.17	799.42	800.06
T_h42	698.95	699.32	748.68	749.01	750.01	798.99	799.30	800.08
T_h43	699.60	699.80	749.47	749.70	750.34	799.60	799.82	800.34
T_h44	699.59	699.82	749.36	749.64	750.42	799.52	799.79	800.42